Spring 5-6-2022

# Mixing Processes in Tidally Pulsed River Plumes: Mechanisms, Significance, and Variability

Preston Spicer
preston.spicer@maine.edu

# MIXING PROCESSES IN TIDALLY PULSED RIVER PLUMES: MECHANISMS, SIGNIFICANCE, AND VARIABILITY

By

Preston Spicer

B.S. University of Maine, 2017

M.S. University of Maine, 2019

A DISSERTATION

Submitted in Partial Fulfillment of the

Requirements for the Degree of

Doctor of Philosophy

(in Civil & Environmental Engineering)

The Graduate School

The University of Maine

May 2022

Advisory Committee:

Kimberly Huguenard, Associate Professor of Civil & Environmental Engineering, Co-advisor

Kelly L. Cole, Assistant Research Professor of Civil & Environmental Engineering, Co-advisor

Lauren Ross, Assistant Professor of Civil & Environmental Engineering

Michael M. Whitney, Associate Professor of Marine Sciences, University of Connecticut

Daniel G. MacDonald, Professor and Chair of Civil & Environmental Engineering, University of Massachusetts Dartmouth

# MIXING PROCESSES IN TIDALLY PULSED RIVER PLUMES: MECHANISMS, SIGNIFICANCE, AND VARIABILITY

By Preston Spicer

Dissertation Advisors: Dr. Kimberly Huguenard and Dr. Kelly L. Cole

An Abstract of the Dissertation Presented
in Partial Fulfillment of the Requirements for the
Degree of Doctor of Philosophy
(in Civil & Environmental Engineering)
May 2022

River plumes form at the river-ocean interface when fresh, buoyant river water merges with salty, dense ocean water and can significantly modify coastal water properties and circulation. It is important to understand how plumes physically mix into the ocean to inform predictive modeling of river-borne tracers to coastal seas. In tidally energetic regions such as New England, river plumes can form and evolve with each new tide and are referred to as "tidally pulsed". In this dissertation, we explore the numerous mechanisms which can contribute to mixing tidally pulsed plumes (i.e., frontal, stratified shear [interfacial], and bottom-generated tidal mixing) their spatiotemporal variability, controlling processes, and the relative importance of each to plume dilution by utilizing numerical modeling and field observation techniques.

The contributions of frontal, interfacial, and bottom-generated tidal mixing are first investigated using an idealized numerical model broadly inspired by the Connecticut River plume. A mixing budget is applied, and river discharge and tidal amplitude are varied between experiments to isolate the influence of each forcing on the budget. Results indicate bottom-generated tidal mixing can dominate the mixing budget for large tide, small discharge events, when the product of the nondimensional Estuarine Richardson number and inverse Rossby number ($Ri_E R_O^{-1}$) exceeds 1. When the nondimensional parameter is below 1, interfacial mixing dominates. Frontal mixing was found to never exceed 10% of total mixing in the budget. This is the first study to identify the potential for bottom-generated tidal mixing to dominate mixing in surface-advected river plumes.

Wind controls on stratified shear mixing in tidal plumes is investigated using a realistic model of the Merrimack River plume system. A salinity variance approach is applied, allowing for the quantification of stratifying and de-stratifying processes (straining, mixing, advection) throughout the tidal plume. Winds countering the right-turning tendency of the plume are found to be most effective at increasing plume mixing. During the wind events, ambient shelf stratification is advected offshore, which creates a saltier shelf condition beneath the plume and increases the vertical salinity gradient. Simultaneously, plume layer velocities are enhanced, increasing shear and straining. The larger salinity gradient between plume and ambient coupled with increased shear leads to enhanced stratified shear mixing in the near and mid-field plume. The wind mechanism was found to be effective at modulating mixing at short, tidal time scales.

The evolution of stratified shear mixing throughout the interior Merrimack River plume is characterized using observational data. Three source-to-front transects were conducted over a ~6-hour tidal pulse during low wind conditions. Data collection on each transect included continuous sampling of current magnitude and direction supplemented by profiles of turbulent kinetic energy dissipation rates and conductivity, temperature, and depth (CTD). Analysis shows stratified shear mixing transforms spatially and temporally over a tide and is characterized by three distinct regimes: plume layer mixing, nearfield interfacial mixing, and tidal interfacial mixing. Plume layer mixing is confined within the plume and decreases offshore of the nearfield as the tide progresses. Nearfield interfacial mixing facilities exchange between the plume and underlying ambient shelf throughout the tidal pulse. Tidal interfacial mixing mixes plume with ambient waters offshore of the nearfield at the end of ebb tide when shelf currents reverse direction beneath the plume. These observations provide some of the most robust spatiotemporal plume mixing estimates to date.

This dissertation highlights the highly variable nature of mixing in tidally pulsed river plumes and the often-important influence of the ambient shelf condition on mixing. Winds and tides impact the collective plume-shelf system to varying degrees which subsequently modulates mixing in a spatiotemporally varying manner. Analyses of static locations or times likely omit essential processes contributing to mixing. This research provides important context for future coastal model development.

## ACKNOWLEDGEMENTS

This work was funded by the National Science Foundation.

I would not be graduating with a PhD in Civil Engineering if Kim Huguenard had not taken a chance on me in 2017. She took me on to the Sensing Storm Surge project and Bagaduce River sampling, even though I had no real experience in anything coastal at the time. The work hooked me, and I found a great advisor, colleague, mentor, and friend in Kim. Thank you for inviting me to be a part of the river plume project, from which this dissertation was built. Thank you for putting up with my countless office "pop-ins" which turned into hour-long conversations on coastal hydrodynamics and/or skiing. Thank you for your humor, which showed me that academia does not need to be so darn serious all the time. Kim, thank you for investing in me, and leading me into the coolest career path ever.

Although I had no intention of becoming a "modeler", Kelly Cole guided me into that life in a wonderful way. I know I am a better researcher because of what you have taught me, which I am unequivocally thankful for. Thanks, Kelly, for troubleshooting ROMS, Python, and MATLAB code with me until our eyes were nearly bleeding. I am truly in debt to you for showing me the beauty of vectorizing code to maximize efficiency (which I am ALL about). Thank you for fielding my many questions over text, which typically turned into pages-long conversations on whatever topic I was stumped on. And thank you for your calm and thoughtful guidance to all questions and problems…whether it be about school or life.

I am indebted to my friend, M.S. co-advisor, and committee member, Lauren Ross, for inspiring adventure, leadership, and confidence in my work. Thank you, Lauren, for initiating my field work trips to France and the Netherlands and entrusting me to cart some pretty darn expensive equipment across an ocean to do so! You have given me the itch to travel and work with global colleagues. I have also been fortunate to experience your remarkably positive outlook toward teaching, research, and life. Thank you for bringing that infectious positivity into every conversation. Thank you for always advocating for me, and pushing me towards opportunity, even when the paths to get there were not always simple.

I am quite lucky to have had external committee members who took a sincere and active interest in my PhD work from start to finish. I thank Dan MacDonald for always challenging me to not forget the details! Our conversations on the nitty-gritty theory within this dissertation were always fruitful and led to a better final product. Thank you also to Mike Whitney for the thoughtful discussions and editing of this work.

Thank you to my fellow plume project graduate students at UMass Dartmouth: Agata Piffer Braga and Nikiforos Delatolas. It was a pleasure to work with you both, both in our virtual meetings and in the field. I appreciate your kindness, support, and technical prowess in the field. I am also grateful for support from fellow graduate students at UMaine: Zhilong Liu, Longhuan Zhu, Taylor Bailey, and Sohiab Alahmed. Our office chit chat, group discussions, and coursework trials and tribulations all contributed greatly to my UMaine experience.

The field work presented in this dissertation would not have been possible without a significant group of people. Thanks to Sam Rickerich and Matt Fischer for making the long drive to the Merrimack with me on multiple occasions. Thank you, Dan Doumani, Tim Healey, and Pete Atherton for captaining and crewing the vessels which were crucial to the success of this project. The modeling component relied heavily on the expertise of Steve Cousins in the Advanced Computing Group at UMaine. Thank you, Steve, for your critical support on the technical aspects of supercomputing and ROMS.

I have always considered myself to be lucky in life. I think I am most lucky to have the family that I do. Thank you to my parents: Scott and Phyllis, and siblings: Hannah, Dan, and Dustin, for endless support and encouragement as I traveled a road quite unfamiliar to our family. Thank you to my grandpa, Mickey, for always giving me confidence in my choices, no matter what. I'm happy and proud of where I come from and where I am today, and I owe that to my family.

Lastly, thank you Carly, my number one cheerleader and confidant. You're unwavering support has been more important to me than you may ever know. I can't wait for our next adventure.

## TABLE OF CONTENTS

## LIST OF TABLES

## LIST OF FIGURES

# CHAPTER 1

# INTRODUCTION

## 1.1. Motivation

More than one-third of precipitation runoff from land travels to the ocean via a river (Trenberth et al., 2007). At the river-ocean interface, fresh river water often flows seaward on top of the saltier ocean water, driven by discharge momentum and differences in buoyancy (Garvine, 1984). Referred to as a river plume, these distinct regions are transitional zones in the coastal ocean where water properties and dynamics are significantly influenced by freshwater (Horner-Devine et al., 2015). River plumes are responsible for the transportation and mixing of land-sourced pollutants, sediments, and organic matter into the ocean and can have a significant influence on coastal health and utility. It is therefore prudent to better understand the implications of river plume processes on the coastal ocean to inform coastal modeling and management decisions.

Important coastal biogeochemical processes can be modulated by river plumes. During the 2010 Deepwater Horizon oil spill, the spatially large Mississippi River plume acted as a conduit for oil transport in the Gulf of Mexico, exhibiting fronts which arrested oil slicks in some regions while guiding oil onshore in others (Kourafalou & Androulidakis, 2013), creating scenarios both aiding and impeding oil mitigation responses. Plumes like the Mississippi have also been found to drive seasonal hypoxia in shelf seas by introducing large scale vertical stratification that suppresses surface water from mixing with the bottom (Hetland & DiMarco, 2008). Sediment transport out of river plumes can harm nutrient and organic matter cycling on the coast, thereby interrupting the nearshore ecosystem (Milligan et al., 2007). In 2011 after Tropical Storm Irene, the Connecticut River plume (Fig. 1) delivered record sediment loads to Long Island Sound (Yellen et al., 2016) which likely had a significant impact on the ecology of the region. Even small river and creek plumes can carry elevated fecal matter into the ocean, leading to beach closures and harmful algal blooms, both of which are frequent occurrences in southern California (Devine, 2014). Collectively if the plethora of biogeochemical processes modulated by river plumes is to

be understood and managed, the underlying physics which dictate transport and mixing needs to be clarified.


Figure 1: Landsat 5 satellite image of the Connecticut River plume following Tropical Storm Irene on September 2, 2011. The Connecticut River, Thames River, and Long Island Sound are labeled. From Simmon (2011).

Physical river plume characteristics are largely determined by the dynamics of the estuarine discharge. Surface advected plumes will form when there is a relatively large buoyancy anomaly between river and ocean water, a relatively narrow river mouth, and low or moderate river discharge. Bottom attached plumes occur when there is small buoyancy anomaly between river and shelf and/or large river discharge (Yankovsky & Chapman, 1997). Surface plumes feature a relatively thin plume layer which can behave independently of bottom-boundary layer processes, while bottom-attached plumes are essentially controlled by the bottom-boundary layer. In this work, we focus on surface plumes, as they often feature more tidal variability to dynamics than their bottom-attached counterparts. Surface advected plumes are

noted by a freshwater layer which detaches from the bottom near the estuary mouth (Fig. 2), shoals, spreads laterally, and advects offshore (Horner-Devine et al., 2015). At the leading offshore edge is the plume front, which marks the boundary between plume and ambient waters (Fig. 2). The front typically exhibits a bore-like structure and is characterized by strong convergence, downwelling, and horizontal density gradients (Kilcher & Nash, 2010; Marmorino & Trump, 2000). Dynamics at the front and within the plume interior both modulate mixing of plume water to the shelf. Mixing transfers momentum, buoyancy, and suspended materials across isopycnals and is important in controlling plume water fate (Horner-Devine et al., 2015).

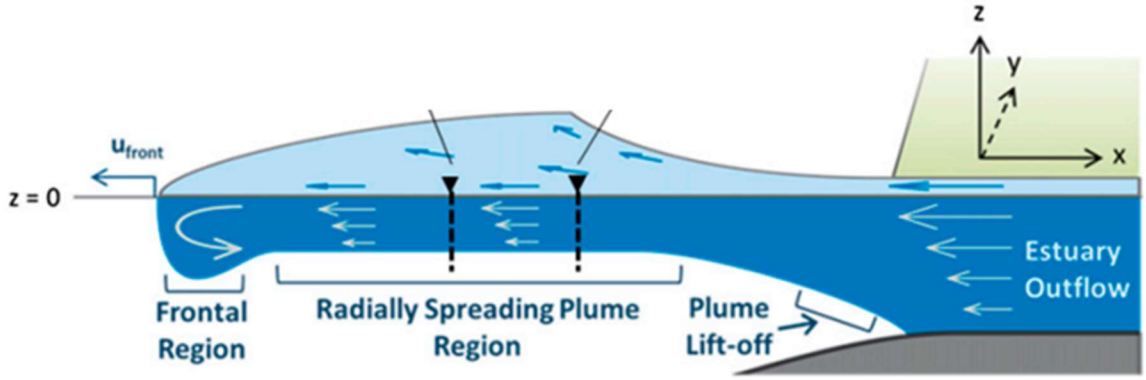


Figure 2: Conceptual schematic of a typical surface advected plume. Arrows denote current direction and scale with magnitude. From Jurisa et al. (2016).

River plume mixing has been studied extensively over the past few decades. Research has focused on mixing at the front (e.g., O'Donnell et al., 2008; Orton & Jay, 2005), stratified-shear mixing in the interior plume (e.g., Kilcher et al., 2012; MacDonald et al., 2007; MacDonald & Geyer, 2004), as well as mixing from wind (e.g., Fong & Geyer, 2001; Houghton et al., 2009; Lentz, 2004), waves (Gerbi et al., 2013), and the bottom boundary layer (e.g., de Boer et al., 2008; De Boer et al., 2006; Fisher et al., 2002). To date, our knowledge of plume mixing generally focuses on a specific location or mechanism, omits analysis of temporal variation of mixing, and lacks meaningful intercomparisons and scaling between plumes of different forcing scales.

Tidal river plumes discharge pulses of freshwater to the shelf on each ebb tide (also known as tidally pulsed) and thereby form a plume with significant intratidal variability in dynamics (e.g., Nash et al., 2009). Although multiple observational studies have improved our understanding of tidal plume energetics and mixing (e.g., Kilcher et al., 2012; MacDonald et al., 2007; MacDonald & Geyer, 2004; McCabe et al., 2008; Orton & Jay, 2005; Pritchard & Huntley, 2006), we still lack a mechanistic understanding of spatial and temporal variability in mixing of tidally pulsed plumes, as well as the relative importance of various mechanisms in diluting a tidal plume.

### 1.2. Scientific Questions and Outline

The major goal of this work is to evaluate the relative importance and spatiotemporal variability of tidal plume mixing mechanisms in systems subject to a variety of environmental forcing conditions. This dissertation utilizes idealized modeling inspired by the Connecticut River plume (Connecticut, USA), realistic modeling of the Merrimack River plume (Massachusetts, USA), and observational data in the Merrimack plume to investigate mixing mechanisms in tidal plumes under a variety of environmental forcing, with special attention paid to spatiotemporal evolution. Although frontal mixing is analyzed and discussed to some extent, this work generally concentrates on mixing within the interior plume, as companion work will focus on frontal processes. We aim to answer the following questions:

1. How do tidal currents on the shelf modulate tidally pulsed plume mixing mechanisms?
2. Do realistic winds modulate tidal plume mixing in the near- and mid-field?
3. How does interior plume mixing evolve over a tidal pulse?

Chapter 2 addresses question 1 using numerical output from an idealized model broadly configured to represent the Connecticut River plume. A parameter space of tidal plumes is created with river discharge and tidal amplitude varying between simulations. Results indicate bottom-generated stresses can dominate plume mixing under certain low discharge, large tide conditions. Stratified-shear

mixing is dominant when tides are small, and discharge is large. This chapter is reproduced with minor changes from:

P. Spicer, K.L. Cole, K. Huguenard, D.G. MacDonald, and M.M. Whitney, *The Effect of Bottom-Generated Tidal Mixing on Tidally Pulsed River Plumes*, Journal of Physical Oceanography (2021), https://doi.org/10.1175/JPO-D-20-0228.1.

Chapter 3 addresses question 2 using a realistic numerical model of the Merrimack River plume. Realistic winds, tides, and river discharge from May 2019 are used to analyze the effect of winds on mixing in the Merrimack plume over that month. Results show winds aimed north (countering the downcoast rotation of the plume) advect the plume and stratification offshore and enhance straining and mixing in the near- and mid-field plume. This chapter has been submitted to the *Journal of Geophysical Research* as:

P. Spicer, K.L. Cole, K. Huguenard, D.G. MacDonald, and M.M. Whitney, *Wind Effects on Near and Midfield Mixing in Tidally Pulsed River Plumes*, Journal of Geophysical Research: Oceans (submitted).

Chapter 4 addresses question 3 utilizing observational data (conductivity, temperature, depth [CTD] profiling, microstructure turbulence profiling, and transects of 3D currents) in the Merrimack River plume over a tidal pulse. Robust spatial resolution of turbulence from source to front over three transects allows for mixing to be estimated and characterized. Further, we distinguish between shear mixing in the plume layer and interfacial mixing between the plume and ambient shelf water. This chapter is being prepared for submission to *Geophysical Research Letters*:

P. Spicer, K. Huguenard, K.L. Cole, D.G. MacDonald, M.M. Whitney, *Evolving Interior Mixing Regimes in a Tidal River Plume*, Geophysical Research Letters (in prep).

Lastly, chapter 5 summarizes the dissertation. The implications of this work are discussed, as well as future research paths and needs. The remainder of chapter 1 will first provide more in-depth background on mixing and stratification quantification methods, tidally pulsed river plume physics, and the study areas.

## 1.3. Mixing and Stratification: Quantification Methods and Budgets

### 1.3.1. Mixing in River Plumes

Mixing in river plumes is prone to occur when the gradient Richardson number, *Ri*, is less than a critical value of 0.25 (Geyer et al., 2008; Miles, 1961), although it may also occur when $Ri > 0.25$ (e.g., Giddings et al., 2011). In formulation, $Ri = N^2/S^2$, where $N^2 = -\frac{g}{\rho_o}\frac{\partial \rho}{\partial z}$ is the buoyancy frequency ($g$ is the gravitational acceleration, $\rho_o$ is a reference density, and $\rho$ is the density at each vertical coordinate, $z$), and $S^2 = (\partial u/\partial z)^2 + (\partial v/dz)^2$ is the squared vertical shear in horizontal currents ($u$ and $v$ being the east-west and north-south currents, respectively). Physically, buoyancy will be mixed across isopycnals when velocity shear becomes large enough to overcome stratification, generally when $Ri = 0.25$ (e.g., Geyer et al., 2010; Gregg, 2004). Horizontal fluxes in salinity and buoyancy are considered minor relative to vertical, so mixing is classically quantified as the turbulent vertical buoyancy flux (Horner-Devine et al., 2015), $B = -\frac{g}{\rho_o} K_\rho \frac{\partial \rho}{\partial z}$, where $K_\rho$ is the eddy diffusion coefficient. In highly sheared and stratified environments such as river plumes, $B$ can be parameterized with the turbulent kinetic energy (TKE) dissipation rate, $\varepsilon$, which can be estimated observationally and evaluated numerically (Horner-Devine et al., 2015). Former work has shown $B$ scales with the TKE dissipation rate: $B = \Gamma\varepsilon$, by applying a maximal mixing efficiency, $\Gamma$, of 0.2 (Ivey & Imberger, 1991; Jurisa et al., 2016; Nash & Moum, 2005). If turbulence can be measured or estimated via overturns (Orton & Jay, 2005) or microstructure techniques (Moum et al., 1995), mixing can be estimated using the above parameterization. The vertical turbulent buoyancy flux can also be estimated numerically using $K_\rho$ output from turbulence closure

schemes (e.g., Cole & Hetland, 2016). Recent numerical work has also introduced a new definition of mixing utilizing $K_\rho$, which is explained further in the next section.

### 1.3.2. Stratification and Mixing Budgets

In order to determine the relative importance of the various plume mixing mechanisms to each other and total mixing, it is useful to compute budgets which quantify both stratification and mixing. In this work, we utilize variations of two approaches: one based on the potential energy anomaly and another utilizing the salinity variance method. Each method carries advantages and disadvantages over the other and are more readily applied depending on the data available (e.g., numerical model output vs. observational data). The formulation, applicability, advantages, and limitations of each method are presented below.

#### 1.3.2.1. Potential Energy Anomaly

Stratification can be quantified via the potential energy, $\varphi$, and physically represents the mechanical energy required to vertically homogenize the water column:

$$\varphi = \frac{1}{\eta+H}\int_{-H}^{\eta} gz(\bar{\rho}-\rho)dz \qquad (1)$$

where $\eta$ is the free surface elevation, $H$ is the water depth, and $\bar{\rho}$ is the depth averaged density (Burchard & Hofmeister, 2008; J. H. Simpson & Bowers, 1981). Energy budgets based on Equation 1 have been formulated and applied to river plumes (e.g., de Boer et al., 2008; MacCready et al., 2009; Pritchard & Huntley, 2006) with the most notable and simple version presented by Pritchard & Huntley (2006). In their budget, Pritchard & Huntley (2006) parameterize the instantaneous power, or work (in Watts), required to mix a plume of depth $d$ over total depth $h$, as:

$$P = \frac{h-d}{2}\Delta\rho g Q_b \qquad (2)$$

where $\Delta\rho$ is the difference in density between plume and ambient waters and $Q_b$ is the estuarine discharge. The authors then evaluate the mixing power input to the plume by multiple mixing mechanisms, namely frontal processes, surface stresses (wind), and bottom stresses (tidal). Frontal mixing is evaluated as a volume integral of *B* in the frontal region of the plume:

$$P_f = \frac{1}{\rho_o}\int_0^{r_f}\int_{-d}^{0} B\, dzdr \qquad (3)$$

with $r_f$ being the frontal width and *r* the horizontal coordinates within the front. Wind mixing is parametrized as:

$$P_w = \delta\rho_a W_{10} U_w^3 \qquad (4)$$

with $\delta$ being the wind stirring efficiency factor (a constant of 0.001), $\rho_a$ is the density of air, $W_{10}$ is the wind drag coefficient, and $U_w$ the mean wind speed. Similarly formulated, tidal mixing is taken as:

$$P_t = \gamma\rho_o C_D U_t^3 \qquad (5)$$

where $\gamma$ is the tidal stirring efficiency factor (0.037), $C_D$ is the bottom drag coefficient (0.0025), and $U_t$ is the vertically averaged tidal current speed. Equations 2 through 5 can be evaluated for different times during a tidal plume pulse, with the relative importance of each mechanism determined as the ratio of mixing power ($P_f$, $P_w$, or $P_t$) to total mixing power ($P$). The method presented by Pritchard & Huntley (2006) is simple and can be easily evaluated with oceanographic measurements but carries shortcomings. For one, Equations 4 and 5 are indirect parameterizations of wind and tidal mixing, which require assumptions on stirring efficiency and drag. Further, interfacial mixing due to stratified-shear instabilities is omitted from analysis, even though the mechanism has been considered quite important in other tidal plumes (i.e., Kilcher et al., 2012; MacDonald et al., 2007). Lastly, the budget does not close (i.e., there can be residual mixing power which is unaccounted for) due to the simplistic parameterizations presented. Although the potential energy equation can be derived in such a way which allows for the quantification

of stratifying and destratifying processes in a closed budget, it becomes quite complicated (10 terms) and only applicable to numerical output (de Boer et al., 2008).

#### 1.3.2.2. Salinity Variance

Recently, another metric quantifying stratification in estuaries and coastal seas was developed. The salinity variance equation was first introduced as a means of linking stratification, straining, and mixing (Burchard & Rennau, 2008). The method, and similar versions, have been widely used in studying estuarine exchange, mixing, and transport (e.g., Burchard et al., 2019; Lorenz et al., 2021; MacCready et al., 2018; Wang & Geyer, 2018; Warner et al., 2020). The method is particularly amiable to numerical model output, as all terms can be quantified relatively simply. As a basis, stratification is quantified at each vertical coordinate in the water column as the vertical salinity variance:

$$(S_v')^2 = (S - \bar{S})^2 \qquad (6)$$

where $S$ is the salinity at each $z$ coordinate, and $\bar{S}$ is the depth average of those salinities. Net stratification in the water column is then taken as the depth integral or average of $(S_v')^2$. Using the Reynold's averaged salt conservation advection – diffusion equation, Li et al. (2018) analytically derive a dynamic equation for the vertical variance as:

$$\frac{\partial (S_v')^2}{\partial t} + \nabla \cdot [\boldsymbol{u}(S_v')^2 - \boldsymbol{K}\nabla(S_v')^2] - 2S_v'\overline{\boldsymbol{u_v'} \cdot \nabla S_v'} = -2\boldsymbol{u_v'}S_v' \cdot \nabla\bar{S} - 2(\boldsymbol{K}\nabla S_v') \cdot S_v' \qquad (7)$$

In Equation 7, $\boldsymbol{u}$ is the 3D velocity vector, $\boldsymbol{K}$ is the 3D eddy diffusivity tensor, $\boldsymbol{u_v'} = \boldsymbol{u} - \overline{\boldsymbol{u}}$ is the 3D velocity deviation, and $S_v' = S - \bar{S}$ is the vertical salinity deviation. Vertically integrating Equation 7 and ignoring horizontal diffusive fluxes and mixing gives:

$$\frac{\partial \int (S_v')^2 dz}{\partial t} + \nabla_h \cdot \int \boldsymbol{u_h}\,(S_v')^2 dz = \int -2\boldsymbol{u_v'}S_v' \cdot \nabla\bar{S}\, dz - \int 2K_z \left(\frac{\partial S}{\partial z}\right)^2 dz \qquad (8)$$

with $\nabla_h$ being the horizontal gradient operator, $\boldsymbol{u_h}$ the horizontal velocity vector, and $K_z$ is the vertical eddy diffusivity. The terms in Equation 8 represent (from left to right), the time rate of change of vertical variance, advection, straining, and dissipation (mixing). Equation 8 is favorable over the potential energy formulations because it directly quantifies stratification development (through straining) and transport (advection) with mixing in a simple equation. Equation 8 is also a closed budget, and any residual (after summation of terms) is considered numerical mixing (e.g., Li et al., 2018; Warner et al., 2020). The salinity variance approach is at a disadvantage to the Pritchard & Huntley (2006) method as the contribution to mixing from specific mechanisms cannot be quantified, although mixing regions can be.

### 1.4. Tidal Plume Dynamics

River plumes can form under a variety of tidal forcing conditions. Some plumes (like the Mississippi) experience negligible tidal forcing at the estuarine outflow and are forced mainly by discharge and wind. Others (like the Columbia River plume) are forced by significant tidal currents in-estuary which control some (or all) plume dynamics at a tidal time scale (Horner-Devine et al., 2015). These tidal, or tidally pulsed, river plumes are the focus of this work. Tidal river plumes feature both interior and frontal processes which are strongly modulated by tides as the plumes typically exit an estuary on ebb tide and are separated from the coast or pushed back into the estuary during flood tide. Tidal currents and their direction influence plume spreading rates which modulates interfacial mixing from stratified-shear instabilities (Luketina & Imberger, 1987; MacDonald et al., 2007; McCabe et al., 2008). The front also propagates at different speeds and direction according to the tide, and so frontal mixing is expected to be connected to tides as well (e.g., Rijnsburger et al., 2018). Significant alongshore tidal currents can "sweep" a plume back and forth on the shelf (e.g., Rijnsburger et al., 2018, 2021; Whitney et al., 2021) whereas a tidally pulsed discharge over deeper, slower shelf tides creates a prototypical, radially expanding plume on each ebb (e.g., Cole et al., 2020; Huguenard et al., 2016; Kilcher et al., 2012). Thus, the front and the plume which it is attached to undergo intratidal transition both spatial and temporal in nature. The dynamical regions which define each plume vary as well and

influence mixing. River plumes are generally divided into three main regions: the nearfield, midfield, and far field (Fig. 3). Although the far-field is not considered to be part of a tidal river plume (objectively subtidal in nature), it is still included in this description for completeness.

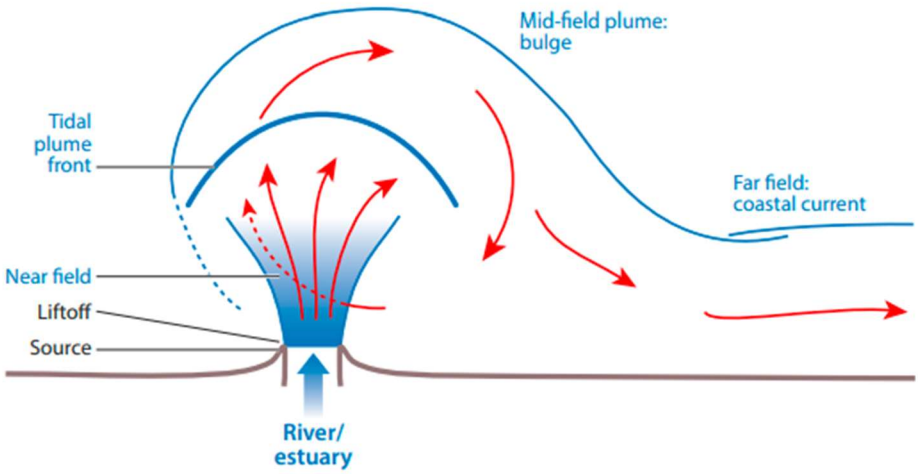


Figure 3: Conceptual schematic of a prototypical tidal plume and dynamical regions. From Horner-Devine et al. (2015).

### 1.4.1. Near-field Plume

The near-field plume (see Fig. 3) is characterized as a jet-like region originating at the plume source where the surface plume detaches from the bottom (Horner-Devine et al., 2015; Jones et al., 2007). Flow in the near-field exhibits rapid shoaling (becomes thinner), spreading, and acceleration which is caused by enhanced barotropic and baroclinic pressure gradients near the mouth. Froude numbers ($Fr = u\sqrt{gh}$, where $u$ is the plume layer velocity and $h$ is the plume layer thickness) in the near-field are supercritical (Fr > 1) indicating turbulent conditions (Hetland, 2005). Consequently, interfacial stresses between ambient and plume waters are typically maximized in the near-field (Kilcher et al., 2012; McCabe et al., 2008). The near-field plume is most sensitive to tidal discharge (e.g., Horner-Devine et al., 2009; Kilcher et al., 2012) and will exist if the river mouth is wider than the Rossby radius of deformation ($R_d = \sqrt{gh}/f$, where $f$ is the Coriolis frequency) (Horner-Devine et al., 2015). The barotropic pressure gradient, baroclinic pressure gradient, interfacial stresses, and acceleration dominate the momentum

balance in the near-field plume, and so influence from wind, Earth's rotation, and ambient shelf conditions is thought to be negligible (McCabe et al., 2009).

Observations of turbulence and mixing in the near-field are typically larger than other plume regions due to intense flow acceleration and shear. Shear mixing TKE dissipation rates have been shown to be as large as $10^{-3}$ $m^2$ $s^{-3}$ (e.g., MacDonald et al., 2007; MacDonald & Geyer, 2004; McCabe et al., 2008). The largest turbulence and mixing is found immediately seaward of the river mouth where acceleration is largest. Seaward of that, the plume slows as saltier water is entrained within the plume, subsequently decreasing mixing (Hetland, 2010). Strong shear at the near-field plume base creates favorable conditions for Kelvin-Helmholtz (KH) instabilities to form which drive the significant turbulence and mixing between the plume and ambient shelf (Smyth et al., 2001; Smyth & Moum, 2000; Thorpe, 1969, 1971).

### 1.4.2. Mid-field Plume

The mid-field plume is the dynamical region where the near-field "jet" begins transitioning to a far-field plume coastal current (Fig. 3). Discharge momentum stops driving plume advection, allowing Earth's rotation and/or alongshore shelf currents to arrest spreading and turn the plume downcoast in the direction of Kelvin wave propagation (Fong & Geyer, 2002; Garvine, 1987; McCabe et al., 2009). The plume then evolves into a geostrophic or wind-driven coastal current, traveling parallel to shore (Horner-Devine et al., 2015). Momentum in the mid-field is dominated by Coriolis, centripetal acceleration, and the cross-stream internal pressure gradient (e.g., Horner-Devine, 2009; Yankovsky & Chapman, 1997). The mid-field plume can form anew on each tidal pulse in small to medium discharge plumes [i.e., the Merrimack River plume (Cole, 2014)] or develop more slowly as a rotational "bulge" accumulating water from multiple tidal pulses in larger systems [i.e., the Columbia River plume (Horner-Devine, 2009)]. Shear-driven mixing can sustain in the mid-field plume but is much less energetic as spreading is arrested (e.g., Cole & Hetland, 2016; Hetland, 2010). Wind, wave, and tidal-driven mechanisms can therefore become more influential on net mixing in the mid- and far-field plume and is explained further in the next section.

### 1.4.3. Far-field Plume

The mid-field region transitions a river plume into a far-field coastal current (Fig. 3), which is disconnected completely from discharge momentum and is driven by the Coriolis force, wind stress and/or bottom stress, and buoyancy-driven flow (Horner-Devine et al., 2015). The far-field current exists and develops at subtidal time scales in all systems. Dynamics of the current are largely controlled by shelf slope (Avicola & Huq, 2002), bottom attachment (Yankovsky & Chapman, 1997), and/or wind (e.g., Fong & Geyer, 2001; Jurisa & Chant, 2013; Lentz, 2004).

Mixing in the mid- and far-field plume can be driven directly by wind stresses mixing plume waters from the surface to depth (Houghton et al., 2009). Direct wind mixing often results in TKE dissipation rates much smaller than those driven by interfacial stresses in the nearfield ($\varepsilon \sim 10^{-6}$ $m^2s^{-3}$), but act over a much larger region. Winds typically mix the mid- and far-field more indirectly by enhancing shear. Constant wind stresses enhance Ekman transport which subsequently increases shear and mixing in the surface plume layer (Fong & Geyer, 2001; Hetland, 2005; Lentz, 2004). Shear and the corresponding effect on far-field mixing is modulated by wind direction: i.e., upwelling versus downwelling favorable. Wind can further contribute to plume mixing by creating waves which break on the immediate plume surface and generate turbulence that dissipates into the plume layer (i.e., Thomson, 2012; Thomson et al., 2014). Although TKE dissipation rates associated with waves can be exceptional ($\varepsilon \sim 10^{-2}$ $m^2s^{-3}$), numerical modeling and observational work have shown wave-generated turbulence to be insignificant in mixing plumes (Gerbi et al., 2013; Kastner et al., 2018), likely because the plume base is deeper than wave-induced turbulence can reach. Wave-generated mixing is likely of more importance in smaller, thinner plumes or at the plume front (Thomson et al., 2014).

Mixing from tidal processes can occur in the mid- and far-field plume (and perhaps the near-field, but this has yet to be studied). Observations have shown tidal ellipses which rotate in opposing directions in the bottom boundary layer relative to the surface plume initiate a type of straining which increases and decreases stratification at a tidal time scale (de Boer et al., 2006, 2008; Visser et al., 1994). It is likely tidal bottom stresses generated in the boundary layer can also drive mixing (N. R. Fisher et al., 2002),

although a direct quantification of this tidal mixing is yet to be evaluated. Pritchard & Huntley (2006) hypothesized tidally driven bottom stresses to be influential, but indirectly parameterized the mechanism. Tides can also alter frontal propagation speed and direction (Rijnsburger et al., 2018, 2021), which likely modifies frontal mixing.

#### 1.4.4. The Plume Front

The front is perhaps the most notable feature of many river plumes and is often visible from the surface due to strong convergence and downwelling which can trap sediment and debris, create a foam line, and/or exhibit a marked surface roughness (Ackleson & O'Donnell, 2011; Rascle et al., 2020). The river plume front is modified by many of the processes which govern the dynamical plume regions outlined above: wind, waves, tides, rotation, discharge, etc. (Horner-Devine et al., 2015). The front has also been shown to evolve as an independent feature: i.e., it can sustain and propagate even if the plume behind it is disconnected from the river source (Cole et al., 2020). The role of the front in dictating plume dynamics, and mixing in particular, is an open topic which we consider in this dissertation.

During the initial stages of an ebb plume discharge, the front physically resembles a bore-like structure which propagates offshore relatively quickly, driven by discharge momentum (Marmorino & Trump, 2000). The frontal head is at the immediate plume boundary with ambient waters, exhibits significant convergence, and dives relatively deep into the water column compared to the plume behind it (e.g., Kilcher & Nash, 2010). A turbulent wake typically follows behind the frontal head, and intense turbulence and mixing can occur there which is comparable to that of the nearfield [$\varepsilon \sim 10^{-3}$ $m^2 s^{-3}$, (Horner-Devine et al., 2013; O'Donnell et al., 2008; Orton & Jay, 2005)]. The region over which strong mixing occurs is relatively narrow, with estimates ranging from 15 m to 60 m behind the frontal head (Itsweire et al., 1993; O'Donnell et al., 2008). As the tidal pulse progresses, the front may transition to a more geostrophic state with less intense vertical mixing, more comparable to a shelf-break front in cross-shore thermal wind balance (Yankovsky & Chapman, 1997). If the front slows to speeds less than the ambient wave speed, energy can also be transported out of the front via internal waves and bores (e.g., Huguenard et al., 2016; Nash & Moum, 2005; Stashchuk & Vlasenko, 2009). The evolution of frontal

mixing and relative importance to other mixing mechanisms throughout a tidal plume's evolution is still quite uncertain. Estimates of the percent contribution of the front to total mixing range from 100% (Pritchard & Huntley, 2006), to 60% (Huguenard et al., 2016), to 20% (Orton & Jay, 2005), and possibly less (Cole, 2014; Cole et al., 2020).

## 1.5. Study Areas

Observational and numerical work in this dissertation focuses on two, dynamically different, tidally pulsed river plume systems in New England. The Merrimack River plume discharges into the Gulf of Maine near Newburyport, Massachusetts (Fig. 4), and features a more typical, radially expanding plume which advects over a relatively calm ambient shelf. The Connecticut River plume discharges to Long Island Sound (LIS) near Old Saybrook, Connecticut (Fig. 4), where it experiences significant modulation from energetic alongshore tidal currents. The differing dynamics of each plume create an opportunity to evaluate and compare mixing mechanisms in tidal plumes exposed to a variety of environmental forcing and ambient shelf conditions.

### 1.5.1. Merrimack River Plume

The Merrimack River watershed covers a large portion of New Hampshire and Northeastern Massachusetts. River flows vary from 100 $m^3 s^{-1}$ in the summer months to maxima near 600 $m^3 s^{-1}$ in April and May. The predominantly semidiurnal tides in the vicinity of the river mouth are macrotidal, with ranges varying between 1.5 m and 3 m (Hetland & MacDonald, 2008). The river enters the Gulf of Maine through a narrow (300 m) channel bounded by jetties on the north and south sides. The narrow entry and strong tidal forcing make the Merrimack River estuary a strongly forced, salt wedge estuary, with reversing flows through the mouth which are tide dependent (Geyer et al., 2008). Salt intrusion in the system can extend nearly 10 km inland under low river flows. During low discharge periods ($< 300 m^2 s^{-1}$), freshwater is mixed significantly with oceanic inflow in the estuary, and a more "mixed" salinity class water exits the estuary on ebb tides (Ralston, Geyer, & Lerczak, 2010; Ralston, Geyer, Lerczak, et al.,

2010). For higher discharges (> 300 $m^2$ $s^{-1}$), the salt wedge is forced seaward and nearly completely fresh water exits the estuary near surface, forming a plume (Hetland & MacDonald, 2008; Ralston, Geyer, Lerczak, et al., 2010). During sufficiently large discharges (> 400 $m^2$ $s^{-1}$), a 5 m deep sandbar, ~500 m offshore from the jetties, acts as a lift-off point for the plume where it detaches from the bottom and begins spreading.

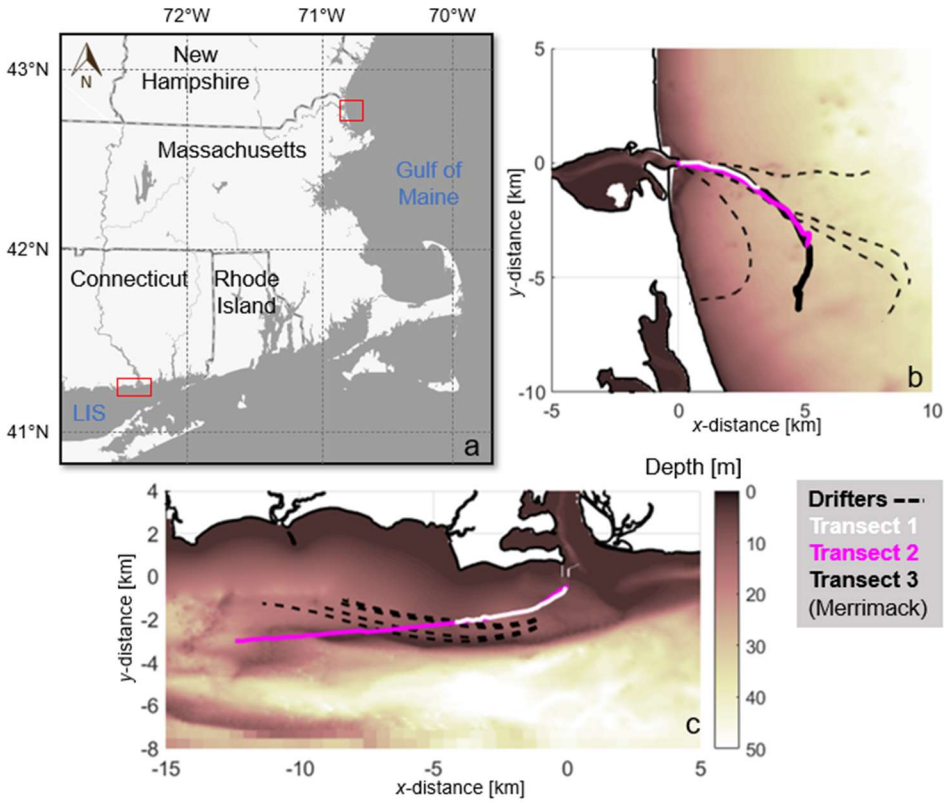


Figure 4: (a) Locations of the Merrimack and Connecticut River outflows relative to New England, the Gulf of Maine, and Long Island Sound (LIS). (b) Zoom in on the Merrimack River plume, showing drifter tracks (dashed black) and sampling transects (solid white, magenta, and black) from a field campaign on April 20, 2021. (c) Zoom in on the Connecticut River plume, showing drifter tracks (dashed black) and sampling transects (solid white and magenta) from a field campaign on October 13, 2021.

The near-field region of the Merrimack River plume has been studied extensively in the past decade, particularly in regard to spreading and mixing (e.g., Chen et al., 2009; Hetland & MacDonald,

2008; MacDonald et al., 2007, 2013; MacDonald & Chen, 2012). In general, stratified-shear instability dominates mixing processes in the plume (e.g., MacDonald et al., 2007), albeit other mechanisms and regions have not been studied thoroughly. Radial expansion occurs throughout the near-field, with a transition to geostrophic mid-field conditions within 6 to 12 hours, depending on discharge (Kakoulaki, 2015). Unlike some larger tidal plumes, transport in the near-field and mid-field of the Merrimack has been found to be sensitive to wind, and it is hypothesized that mixing is equally sensitive (Kakoulaki et al., 2014). River discharge is perhaps the most important forcing mechanism for the Merrimack plume, as it dictates plume development, where mixing occurs, and the amount of ambient stratification on the shelf from former plumes, which collectively modulate subsequent plume formation and dynamics (Cole, 2014).

### 1.5.2. Connecticut River Plume

The Connecticut River is the longest river system in New England, with a mean annual discharge of ~500 $m^3 s^{-1}$ and spring freshet flows which can exceed 1000 $m^3 s^{-1}$ in April and May (Yellen et al., 2017). Tidal ranges at the mouth of the river vary from 1 to 1.5 m and are mainly semidiurnal. The estuary itself is relatively shallow (10 – 12 m deep channel, 4 – 6 m shoals), and features multiple constrictions which restricts flow to 300 – 400 m widths. Salt intrusion extends anywhere from 5 to 15 km inland, depending on flow conditions (Ralston et al., 2017). Dynamically, the Connecticut River estuary is similar to the Merrimack estuary, featuring a salt front which propagates inland on floods and intense mixing on ebbs (Ralston, Geyer, Lerczak, et al., 2010). The river outflow to Long Island Sound is approximately 1400 m wide, from which a ~2 m deep plume protrudes under most discharge conditions.

Dynamics in the Connecticut River plume are strongly forced by the significant ambient tidal currents (> 1 m/s) in LIS, which are predominantly rectilinear and shore-parallel in the vicinity of the plume (Bennett et al., 2010). During the initial ebb discharge, the plume is forced to the east with ebb currents exiting LIS, while flood currents reverse in direction and swing the plume to the west (Garvine, 1974, 1977; Garvine & Monk, 1974). Mixing in the Connecticut River plume has not been studied

extensively, although it has been inferred from tracer variance budgets (e.g., Whitney et al., 2021). Generally, LIS is stratified due to plume water from former tidal pulses which recirculates within the estuary. Plume water may exits LIS within several days, or travel on longer routes (on the order of months) throughout the estuary (Deignan-Schmidt & Whitney, 2018; Jia & Whitney, 2019).

# CHAPTER 2

# THE EFFECT OF BOTTOM – GENERATED TIDAL MIXING ON TIDALLY PULSED RIVER PLUMES

## 2.1. Introduction

River plumes are created by the discharge of buoyant river water into the coastal ocean and create distinct hydrodynamic regions in the nearshore environment where water properties and dynamics are significantly influenced by freshwater. More than one-third of precipitation runoff from land travels by river to the ocean, where it is often mixed into the ocean via a river plume (Trenberth et al., 2007). River plumes are therefore responsible for the transportation and mixing of land-sourced pollutants, sediments, and organic matter into the ocean and so influence how these materials effect ecologically sensitive coastal zones. How tracers such as these are mixed into the ocean is related to physical mixing dynamics within a plume. Multiple mechanisms influence plume mixing, but their relative importance within different plumes and to each other has yet to be clarified.

Plume mixing is primarily controlled by stratified-shear instabilities, frontal processes, and wind forcing which create turbulent fluxes of buoyancy and momentum between the fresh, riverine discharge and salty, ambient ocean [e.g. (Ivey et al., 2008; Sherman et al., 1978; Stacey et al., 2012)]. The vertical turbulent buoyancy flux, $B$, is often estimated to quantify mixing. Point measurements from field data provide coarse estimates of $B$ (MacDonald and Geyer 2004; MacDonald et al. 2007; Orton and Jay 2005; O'Donnell et al. 2008; Horner-Devine et al. 2013), but likely do not capture the heterogeneity in mixing across an entire plume. Those observations therefore begin a framework for estimating the fraction of dilution from fresh water to ocean salinity which each mixing process is responsible for.

To create a more comprehensive framework that quantifies net plume mixing and compares the relative importance of mixing processes in oceanic systems, recent studies have modeled mixing in terms of energy budgets (MacCready et al., 2009; Winters et al., 1995; Wunsch & Ferrari, 2004). In a notable, simplified budget, Pritchard and Huntley (2006) use a potential energy model to argue that three main

mechanisms are responsible for plume mixing: wind stress, tides, and frontal processes [later expanded upon by Horner-Devine et al. (2015)]. The relative importance of those three mechanisms can be estimated if $\varepsilon$, the turbulent kinetic energy dissipation rate, is known within the plume. A few observational studies have applied the budget with limited measurements (Huguenard et al., 2016; Pritchard & Huntley, 2006). The simplified budget lacks an inclusion of interfacial mixing, created by shear instabilities on the strongly stratified interface between ocean and plume. The budget also lacks a robust tidal mixing term, created by bottom generated shear instabilities from tidal currents, which is broadly parameterized on current magnitudes and an assumed stirring efficiency (both included with frontal mixing conceptually in Fig. 5). Interfacial mixing has been studied extensively and is shown to be important in radially-spreading plume systems (Cole & Hetland, 2016; Hetland, 2005; MacDonald et al., 2007; MacDonald & Geyer, 2004). Although tide-plume dynamics have been studied frequently, tidal mixing itself has largely been ignored but hypothesized to contribute in strongly tidal, shallow systems (N. R. Fisher et al., 2002; Horner-Devine et al., 2015).

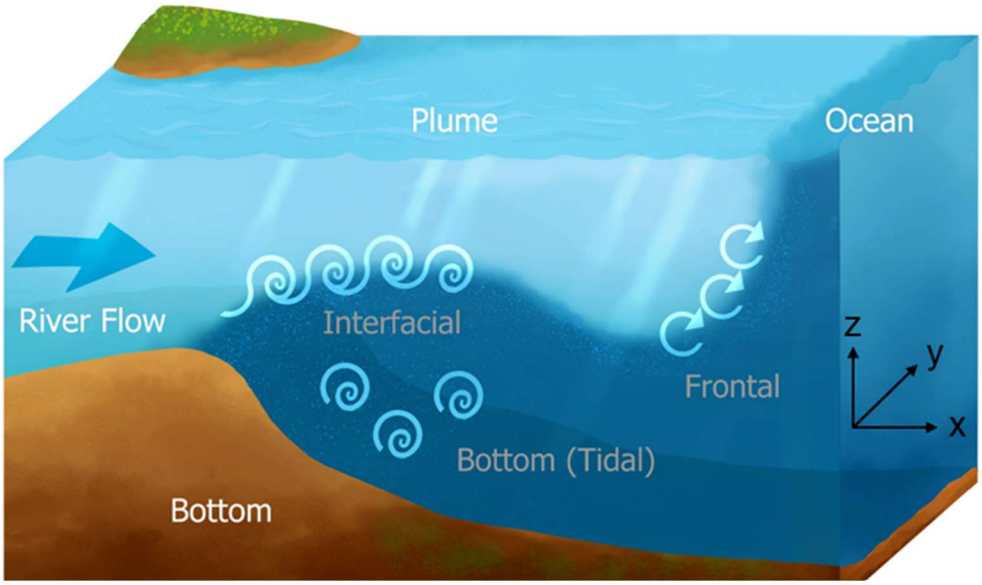


Figure 5: Conceptual model of a river plume shows the major mixing mechanisms excluding wind. Input buoyancy from river discharge is mixed into shelf waters by bottom boundary (tidal), frontal, and interfacial mixing mechanisms. Darker blue indicates saltier ocean water and light blue represents fresher plume water.

Surface advected plumes are influenced by tidal motions which can modify plume structure and mixing, particularly in meso/macrotidal systems (tidal ranges > 2 m). Observations show plume fronts travel according to tidal direction and speed (O'Donnell et al., 2008; Rijnsburger et al., 2018), likely adjusting the importance of frontal and interfacial mixing with the tide. There are also indications that tidally modulated plumes can be subject to a type of tidal straining which periodically transforms plume stratification due to counter-rotating tidal ellipses in the plume and bottom boundary layers (de Boer et al. 2006; de Boer et al. 2008) and likely causes mixing at the plume base (N. R. Fisher et al., 2002). In Long Island Sound, past observations have shown tidally generated bottom stress can be substantial, generating mixing throughout the water column (Bowman & Esaias, 1981; O'Donnell et al., 2014; Whitney et al., 2016), although its effect on mixing the strongly tidal Connecticut River plume within the Sound has not been quantified. Elsewhere, studies have connected tidally generated bottom stress to mixing and particle resuspension in plumes during low discharge, large tide events (Nash et al., 2009; Spahn et al., 2009). Bottom generated tidal mixing and its relative importance to other mechanisms has yet to be quantified in surface plumes.

The simplified mixing energy budget of Pritchard and Huntley (2006) has not been evaluated for an entire plume throughout a tidal cycle, for plumes of different forcing conditions, or with inclusion of non-parameterized interfacial and tidal mixing. The goal of this investigation is to evaluate the importance of interfacial, frontal, and tidal mixing on the net mixing budget of a river plume using an idealized numerical model and energy budget for an entire tidal cycle under varying conditions. The objectives of this work are to (1) quantify how the vertical mixing of plume water into shelf waters varies with tidal current magnitude and river discharge, and (2) diagnose the relative importance of each mixing mechanism to total mixing via the simplified energy budget within that parameter space. Similar to estuaries, plume forcing is closely connected to freshwater discharge and tides and so we identify variation in the mixing energy budget from those forcings. The remainder of this chapter begins with a background on the numerical model configuration (section 2.2) and data analysis (section 2.3). A detailed

account of the numerical simulation results is presented in section 2.4, outlining the importance of interfacial and tidal mixing on the net energy budget. Section 2.5 analyzes the conditions when tidal or interfacial mixing dominate the budget while section 2.6 discusses the relative importance of frontal mixing and the broader implications of this work. The main conclusions are presented in section 2.7.

### 2.2. Model

The simulations demonstrated here utilize the Regional Ocean Modeling System (ROMS) which is a free-surface, hydrostatic, primitive equation ocean model (Haidvogel et al., 2008). ROMS uses stretched, terrain following coordinates in the vertical direction and orthogonal coordinates in the horizontal direction. The domain is idealized so results may be extendable to other systems and features a

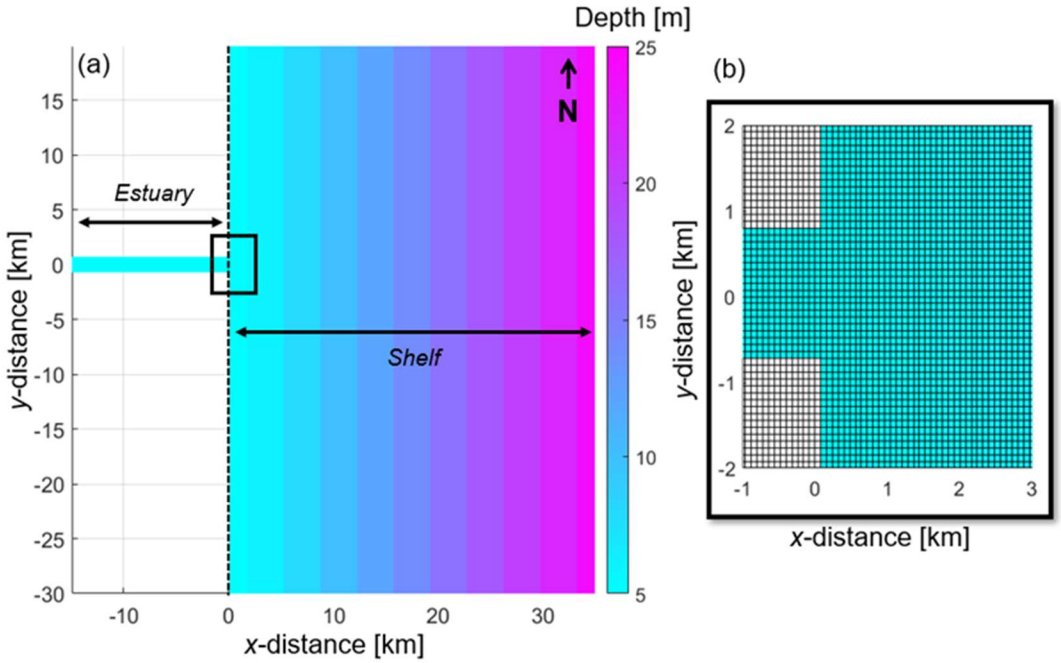


Figure 6: (a) Plan view of bathymetry over the entire model domain, with white area representing land and the dashed line separating estuary and coast from shelf. The horizonal axis is the *x*-distance in km with 0 being in the middle of the estuary, and the vertical axis is the *y*-distance in km, with 0 being the estuary / shelf boundary. (b) Zoom-in of the mouth of the estuary, showing grid resolution and depth at the outflow.

long (15 km) and narrow (1500 m), shallow, constant-depth (5 m) estuary attached to a linearly sloping shelf with a straight coastline (Fig. 6). The shelf depth increases to a maximum of 25 m at the eastern boundary. The oceanic section of the domain is 50 km long and 35 km wide, with square grid cells 80 m x 80 m throughout. The model has 30 vertical layers, with increased resolution at the surface and bottom resulting in ~7 layers within the top 2 m of the water column over the entire domain.

The idealized model configuration broadly represents the Connecticut River plume in Long Island Sound, which has been studied extensively and is noted for significant tidal modulation(Garvine, 1974, 1977; Garvine & Monk, 1974; Jia & Whitney, 2019; O'Donnell, 1997). Long Island Sound features significant along-shore tidal currents due to geometry which makes the Connecticut River plume an ideal system to study the effect of tides on a plume mixing budget. Although dimensions are based on the Connecticut River plume, tidally pulsed plumes with a narrow source (a mouth width smaller than the local deformation radius) will generally spread and mix similarly so results may be extrapolated to other systems.

River discharge is introduced on the western boundary of the 15 km estuary as fresh water (0 psu). Tides are forced by sea level as a sine wave near the $M_2$ period (12 h). The Coriolis parameter, $f$, was calculated for a latitude of 41°N, representative of the Connecticut River plume location. No winds are prescribed in any simulation to simulate simple environmental conditions and eliminate wind mixing from the analysis. A 5 cm $s^{-1}$ constant downcoast current is forced at the up coast oceanic boundary, which is typical of other idealized river plume models and much slower than the tidal currents forced in these experiments (Cole & Hetland, 2016; Hetland, 2005).

Flather and Chapman conditions were applied at the open boundaries for the velocity and free surface, respectively, allowing fluid flow out of the domain (Chapman, 1985; Flather, 1975). Three dimensional velocity components and tracers followed a radiation open boundary condition (Marchesiello et al., 2001). Vertical mixing was described by the k-ε turbulence closure scheme (Umlauf & Burchard,

2003) with Canuto A stability function formulation (Canuto et al., 2001). Horizontal and vertical tracer advections were calculated using the multidimensional positive definite advection transport algorithm [MPDATA, (Smolarkiewicz & Grabowski, 1990)]. Another advection scheme (U3H) was also applied to test the influence of numerical mixing on the analysis presented below. Ultimately, the choice of advection scheme created negligible differences (Appendix C). The bottom boundary layer (BBL) model is applied for bottom stresses, with the nondimensional quadratic friction coefficient set to 0.003 which is typical of estuaries and coastal seas (Valle-Levinson, 2010).

The model is initialized with a flat sea surface and a vertically uniform along-channel salinity gradient in the estuary from 0 psu at the up-river boundary to 32 psu in the oceanic domain. Each simulation was run for four full semi-diurnal tidal cycles before analysis began on the fifth to allow for the estuarine circulation and plume to develop such that consecutive tidal pulses of fresh water onto the shelf exhibited similar horizontal and vertical spatial scales. Passive dye tracers (initial concentration = 1 kg $m^{-3}$) are released from the estuary mouth over the full width and depth at mid-flood tide ($\eta$ =0 m and increasing) on the fifth tidal cycle to track the plume. A parameter space was chosen which encompasses microtidal to mesotidal plumes and relatively low to high discharges with the intent of creating plumes generally strongly tidally modulated. Tidal elevation amplitudes ($\eta_{tide}$) of 0, 0.75, and 1.5 m are each run with discharge rates ($Q$) of 100, 500, and 1000 $m^3$ $s^{-1}$. $\eta_{tide}$ = 0.5 m is also run with Q = 500 and 1000 $m^3$ $s^{-1}$ while Q = 200 $m^3$ $s^{-1}$ is run with tidal amplitudes of 0.75, 1.0, and 1.5 m resulting in 14 experiments total (outlined in Table 1) which gave a realistic and reasonable range of values for the estuary inflow parameters described in the next paragraph. Figure 7 outlines the variation in horizontal plume extent under two different tidal amplitudes with a moderate discharge. For all runs, tidal elevations and velocities are in phase, not unlike a progressive Kelvin wave tide, and so maximum tidal current magnitudes occur during the minimum and maximum tidal elevations (Fig. 7a, e, c, g).

Table 1: Tidally averaged inflow parameters for all experiments. Columns (from left to right) show river discharge, $Q$, tidal elevation amplitude, $\eta_{tide}$, Froude number, $Fr$, Burger number, $S$, baroclinic deformation radius, $R_d$, the Rossby number, $R_o$, estuary Richardson number, $Ri_E$, and $Ri_E R_o^{-1}$.

| $Q$ [m$^3$/s] | $\eta_{tide}$ [m] | $Fr$ | $S$ | $R_d$ [km] | $R_o$ | $Ri_E$ | $Ri_E R_o^{-1}$ |
|---|---|---|---|---|---|---|---|
| 100 | 1.5 | 0.67 | 4.4 | 6.6 | 2.8 | 0.4 | 0.1 |
| 100 | 0.75 | 0.56 | 5.5 | 8.2 | 3.1 | 0.7 | 0.2 |
| 100 | 0 | 0.38 | 5.1 | 7.7 | 2.0 | 390 | 195 |
| 200 | 1.5 | 0.76 | 4.9 | 7.3 | 3.7 | 0.3 | 0.1 |
| 200 | 1.0 | 0.67 | 5.9 | 8.8 | 4.0 | 0.7 | 0.2 |
| 200 | 0.75 | 0.54 | 5.8 | 8.8 | 3.2 | 1.3 | 0.4 |
| 500 | 1.5 | 0.76 | 5.7 | 8.6 | 4.4 | 0.7 | 0.2 |
| 500 | 0.75 | 0.54 | 6.5 | 9.8 | 3.6 | 2.9 | 0.8 |
| 500 | 0.5 | 0.53 | 6.5 | 9.7 | 1.0 | 6.6 | 6.6 |
| 500 | 0 | 0.50 | 6.2 | 9.3 | 3.1 | 497 | 160 |
| 1000 | 1.5 | 0.77 | 6.3 | 9.4 | 4.8 | 1.2 | 0.3 |
| 1000 | 0.75 | 0.55 | 7.0 | 10.4 | 3.9 | 4.7 | 1.2 |
| 1000 | 0.5 | 0.54 | 6.9 | 10.4 | 1.2 | 10.2 | 8.5 |
| 1000 | 0 | 0.59 | 6.7 | 10.1 | 4.0 | 253 | 63 |

Tidally averaged estuary inflow parameters for each experiment are described in Table 1. $R_d = \sqrt{g'h}/f$ is the baroclinic Rossby radius, which describes the length scale at which rotational effects become important over buoyancy, with $g' = g\,\Delta\rho/\rho_0$ being the reduced gravity at the estuary mouth, $h$ is the depth at the mouth, $g$ is the acceleration due to gravity, $\Delta\rho$ is the density anomaly of the inflow relative to ambient, and $\rho_0$ is the ambient density. $R_0 = U/fW$ is the mouth Rossby number with $U$ being the mean velocity of inflow and $W$ is the mouth width. $S = R_d/W$ is the Burger number and $Fr = R_0/S$ is the Froude number. Both $R_0$ and $S$ are greater than unity for all runs, indicating that rotation does not dominate flow at the inflow and $Fr < 1$ for all cases indicating that buoyancy influences plume evolution and the plume is surface advected (Yankovsky & Chapman, 1997).

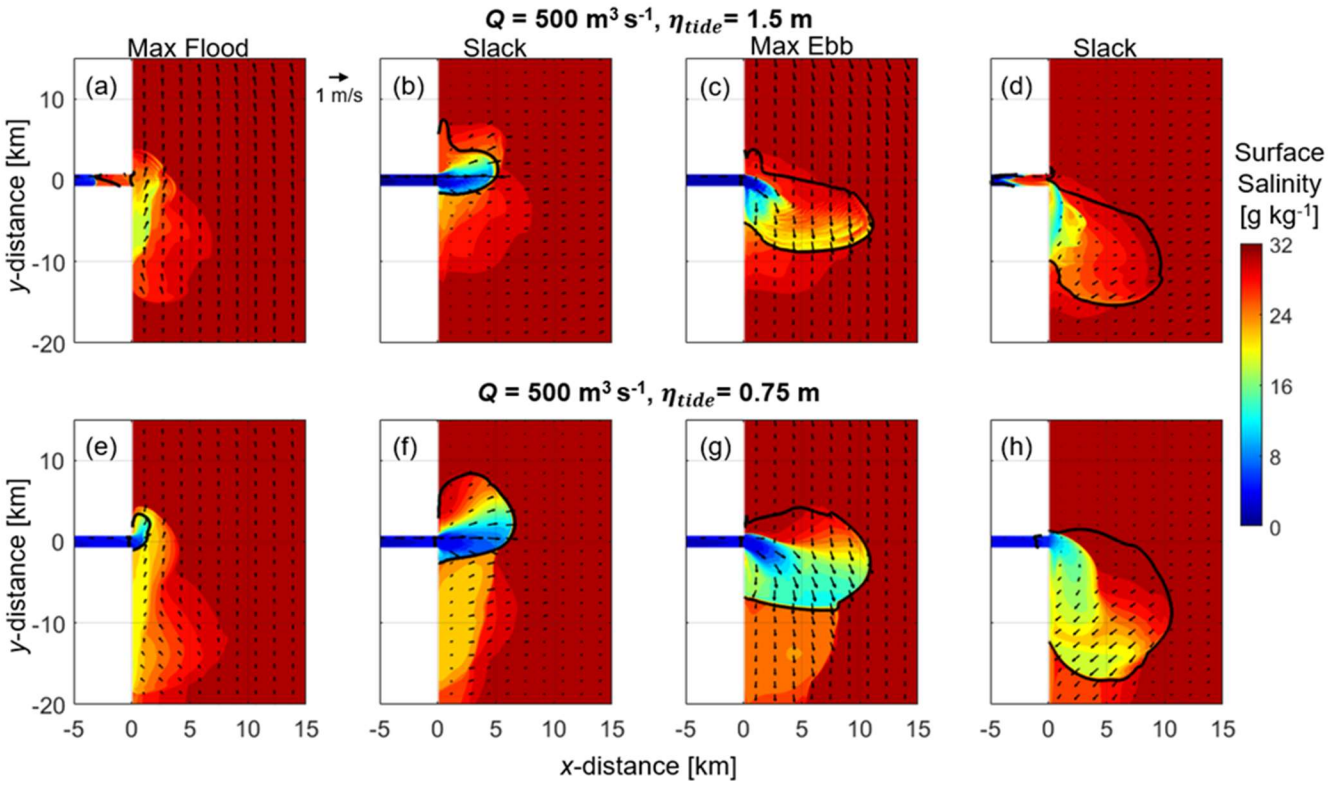


Figure 7: Surface salinity distribution over the fifth tidal cycle for two moderate discharge ($Q$ = 500 m$^3$ s$^{-1}$) runs. Top panels (a – d) show progression from maximum flood tidal currents to the slack tide after ebb for $\eta_{tide}$= 1.5 m and bottom panels (e – h) for $\eta_{tide}$= 0.75 m. The x and y axes are $x$ and $y$ distances, respectively. The thick black line bounds the plume being analyzed according to dye released at the mouth. Surface current magnitude and direction are denoted by black arrows.

### 2.3. Methods

The mixing budget approach utilized in Pritchard and Huntley (2006) is based on a potential energy budget, with the mechanical energy required to completely mix the water column being formulated according to Equation 1. Equation 1 quantifies stratification in the water column (Burchard & Hofmeister, 2008; Horner-Devine et al., 2015) and is used in this work to define the total energy required to completely mix a river plume with ambient waters. We note that $\phi$ can be misleading at times in highly stratified systems, as the location of a two-layer interface relative to the mid-depth can slightly change $\phi$

(MacDonald & Horner-Devine, 2008). Regardless, Equation 1 was deemed appropriate as a simple metric to compare the relative magnitude of stratification between plumes.

Similar to Horner-Devine et al. (2015), we express each mixing energy via the vertical turbulent buoyancy flux, $B$ (units of W/kg) which allows for a determination of mixing power (units of W) after consideration of the density of seawater and depth and area $B$ acts over. The dye release beginning on the fifth tidal cycle was used as the start point for the budget analysis on all experiments and ended when in-estuary dye was cut off from the shelf. The dye distinguishes ambient stratification from the tidal plume. $B$ was calculated at all grid points in that plume allowing for a complete view of plume mixing in space and time. The vertical turbulent buoyancy flux can be calculated as:

$$B = -\frac{g}{\rho_0} K_\rho \frac{\partial \rho}{\partial z}, \qquad (9)$$

where $K_\rho$ is the vertical eddy diffusivity and $\rho$ is the density at vertical coordinate $z$. Equation 9 was determined using the ROMS output of eddy diffusivity and density, which allowed for the simplified mixing energy budget (Pritchard & Huntley, 2006) to be resolved.

The total mixing power, $M$, within the dye-tracked plume was calculated at each time step using a volume integral of $B$ throughout the plume, which we explicitly state here as:

$$M = \rho_0 \sum_{i=0}^{n} A_i \int_{d_{p_i}}^{\eta} B_i \, dz, \qquad (10)$$

where $n$ is the number of horizontal grid points in the plume, $A_i$ is the horizontal area of each cell (80 m x 80 m) in the plume at each grid point $i$, $d_{p_i}$ is the plume depth at each point and is considered the depth where dye concentration falls below $10^{-2}$ kg m$^{-3}$, and $B_i$ is the buoyancy flux at each grid point. The dye threshold chosen produced the most realistic plume boundaries both vertically and horizontally based on in-estuary dye releases as it matched the outer edge of the plume surface salinity field and fell near the largest vertical gradients in dye within the water column. Spatial limits to integration in Equation 10 are

based on Equation 1: i.e. $\phi$ must be greater than 0 at a given dye-tracked plume coordinate and $d_{p_i}$ not equal to the bottom depth (indicating a new, surface-advected plume exists) else $\int_{d_{p_i}}^{\eta} B_i$ is set to zero.

The frontal mixing power, $M_{FR}$, was calculated by summing grid volume integrals of $B$ along a narrow band on the perimeter of the plume considered the frontal region:

$$M_{FR} = \rho_0 \sum_{i=0}^{j} A_i \int_{d_{f_i}}^{\eta} B_i \, dz, \qquad (11)$$

where $j$ is the number of horizontal ρ-grid points in the frontal zone and $d_{f_i}$ is the frontal depth at each point (determined with dye like Equation 10). The total area over which the front is active ($\sum_{i=0}^{j} A_i$) is estimated in different ways in this work. Former research has simply estimated a "frontal distance" over which frontal mixing occurs based on conceptual dimensions, satellite imagery, and frontal propagation speeds (Huguenard et al., 2016; O'Donnell et al., 2008; Pritchard & Huntley, 2006). In this work, $j$ was liberally estimated based on the horizontal gradient of surface dye, with any grid point containing a gradient larger than $10^{-3}$ kg m$^{-4}$ considered as the frontal zone. Gradients of that magnitude only occurred at the plume-ambient boundary and resulted in large frontal distances ranging from the grid length (80 m) to multiple hundreds of meters (up to 300 m). Former estimates of frontal length scales produced values of similar magnitude (Huguenard et al., 2016). Estimates were also made based on salinity gradients and setting a constant length scale to compare results. We found the different values estimated for frontal length scale in this work had little impact on the results and is discussed further in section 2.6.3.

In this work, we present a new method to distinguish the contributions of interfacial and tidal mixing to the plume energy budget in a robust, non-parameterized manner compared to previous studies. In order to quantify the mixing energies, it was important to distinguish the two mechanisms from each other, as they interact with the plume over the same regions (Fig. 5). We followed the estuarine method of Ralston et al. (2010), in which there are conditions (Appendix A) that determine how to separate tidal and interfacial mixing which can slightly modify the structure of the following equations. We present

Equation 12 with the assumption that there is no tidal mixing (Condition 1, Appendix A) whereas Equation 14 assumes both tidal and interfacial mixing (Condition 2, Appendix A). This was considered the most logical way to present the method and is important to note here.

When isolated from other mechanisms, buoyancy flux from shear instabilities at the interface peaks within the plume layer and approaches zero at the plume base and surface, conceptually depicted in Figure 8a (Yuan & Horner-Devine, 2013). In this case, interfacial mixing power, $M_{IF}$, can be calculated by integrating $B$ over the plume layer (excluding the frontal zone), similarly to Equation 10:

$$M_{IF} = \rho_0 \sum_{i=0}^{k} A_i \int_{d_{p_i}}^{\eta} B_i \, dz, \qquad (12)$$

where $k$ is the number of horizontal ρ-grid points in the non-frontal portion of the plume. The total area of the non-frontal portion of the plume ($\sum_{i=0}^{k} A_i$) used to determine $k$ was considered the area bounded by surface dye concentrations greater than $10^{-2}$ kg m$^{-3}$ with the total frontal area subtracted.

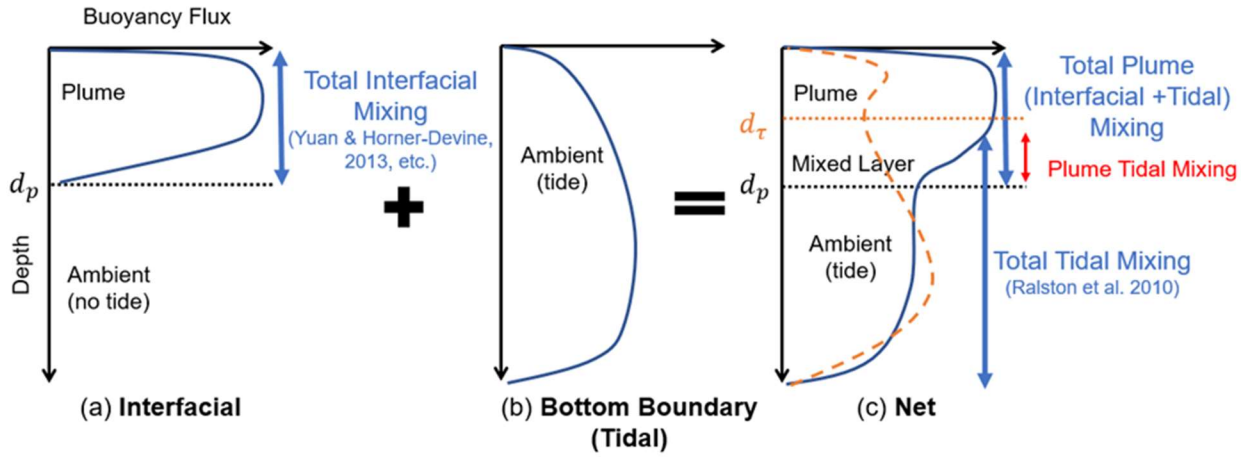


Figure 8: Conceptual diagram of vertical structure of turbulent buoyancy flux, $B$ (blue lines), for only interfacial plume mixing (a), only tidal mixing of ambient stratification (b), and the combination of interfacial and tidal mixing (c). A profile of shear stress, $\tau$ (dashed orange), is shown in (c). Vertical axis on each plot is nondimensional depth and horizontal is nondimensional $B$ and/or $\tau$. Plume depth, $d_p$, and shear stress local minimum depth, $d_\tau$, are labeled.

Equation 12 is complicated when bottom-boundary mixing from tidal currents is introduced. Tidal mixing of ambient shelf water without the existence of a plume results in a peak *B* near the bottom of the water column, decaying to zero at the surface and bottom (Fig. 8b). When plume stratification is introduced, near-surface tidal *B* is damped, though some portion of tidal buoyancy flux may still contribute to mixing the plume water. Conceptually, this creates a non-zero local minima in *B* in the mixed layer at the plume base, shown in Figure 8c (Ralston, Geyer, Lerczak, et al., 2010). Integrating *B* from the surface to the plume base is no longer quantifying strictly interfacial mixing, but rather interfacial mixing combined with a fraction of tidal mixing which influences the plume. In order to separate the two mechanisms, we apply the method of Ralston et al. (2010) to river plumes and distinguish tidal mixing from interfacial via the magnitude of the vertical component of shear stress, $\tau$:

$$\tau = K_m \sqrt{\left(\partial u/_{\partial z}\right)^2 + \left(\partial v/_{\partial z}\right)^2}, \qquad (13)$$

where $K_m$ is the vertical eddy viscosity output from the turbulence closure, and *u* and *v* are the east-west and north-south components to current velocities, respectively. Similar to *B*, local maxima in shear stress can exist near bottom and within the plume layer when both interfacial and tidal mixing are important, with $\tau$ sometimes offset from *B* (Fig. 8c). The local minimum ($d_\tau$) between the two maxima is taken as the boundary between the mixing mechanisms (Fig. 8c, with mixing above $d_\tau$ being only interfacial whereas below is tidal, as described in Ralston et al. 2010). Whenever $d_\tau$ is shallower than $d_{p_i}$, tidal mixing and interfacial mixing both can be considered influential to total plume mixing and $M_T$ is calculated as:

$$M_T = \left[\rho_0 \sum_{i=0}^{k} A_i \int_{d_{p_i}}^{\eta} B_i \, dz\right] - \left[\rho_0 \sum_{i=0}^{k} A_i \int_{d_{\tau_i}}^{\eta} B_i \, dz\right], \qquad (14)$$

where $d_{\tau_i}$ is the local minimum in shear stress at each grid point *i*. Conceptually, the left-hand term in Equation 14 is the total mixing within the plume layer (Fig. 8c) while the right-hand term is mixing from interfacial instabilities only (Fig. 8a).

When Equation 14 is applicable, Equation 12 must be modified to mimic the right-hand term in Equation 14 (condition 2, Appendix A). When $d_{\tau_i}$ is found deeper than $d_{p_i}$, Equation 14 is not applicable and $M_T$ must equal zero (condition 1, Appendix A), and when there is no $d_{\tau_i}$ there is no local minimum and all plume mixing is considered tidal (Ralston, Geyer, Lerczak, et al., 2010) (condition 3, Appendix A). A set of $B$ and $\tau$ profiles from a moderate tide and discharge are shown to exemplify each of these conditions in the data (Fig. 9). In this case, conditions 1 (Fig. 9a, b), 2 (Fig. 9c, d), and 3 (Fig. 9e, f) occur within the same plume as tidal currents increase on ebb (Fig. 10c, d). Considering tidal mixing does not

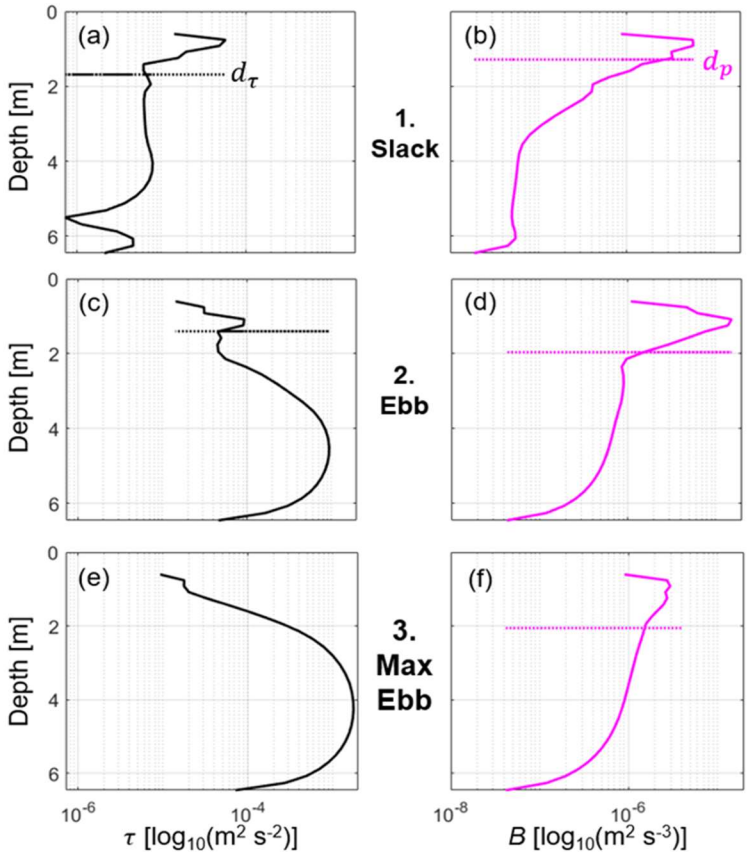


Figure 9: Profiles of shear stress, $\tau$ [(a), (c), and (d)], and vertical turbulent buoyancy flux, $B$ [(b), (d), and (f)], from the $Q$ = 500 m$^3$ s$^{-1}$, $\eta_{tide}$= 0.75 m run taken at $x$ = 3 km, $y$ = 0 km. Profiles were taken at slack tide (1), mid-ebb (2), and max ebb (3) and correspond to each mixing calculation condition outlined in Appendix A. Vertical axis on each plot is depth and horizontal is $B$ and/or $\tau$. Plume depth, $d_p$, and shear stress local minimum depth, $d_\tau$, are labeled if they are present.

distinguish between the frontal region and interior of the plume, the same conditions apply in the frontal zone (Appendix A). Tidal mixing below the plume layer was evaluated and considered negligible in its effect on Equation 14 (Appendix B), justifying the integration to $d_{p_i}$. The method outlined above was corroborated by turning bottom friction on and off in the model and quantifying tidal mixing as the difference between Equation 12 with friction and Equation 12 without friction. That test was used on most cases and produced nearly identical results (not shown) to those presented in the next section. The nature of the equations presented above is such that all mixing power terms ($M_F$, $M_{IF}$, $M_T$) always sum to the total plume mixing power, $M$. Each term is comprised of some volume integral of $B$ within the total

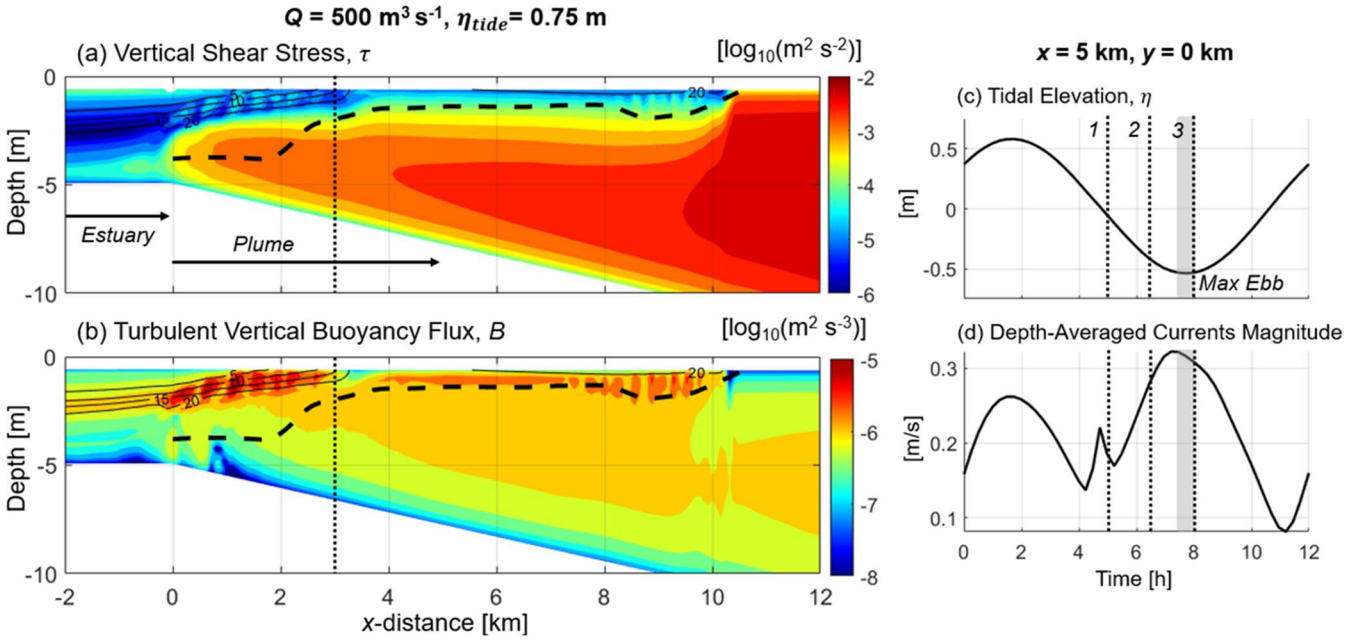


Figure 10: Contours of shear stress, $\tau$ (a), and vertical turbulent buoyancy flux, $B$ (b), during max ebb for the $Q$ = 500 m$^3$ s$^{-1}$, $\eta_{tide}$= 0.75 m run (see Fig. 7g) at $y$ = 0 km. Both color bars are on a log$_{10}$ scale. Contours of density anomaly, $\sigma_\theta$ in kg m$^{-3}$, are shown as solid black lines and labeled, while the plume depth according to the dye release is marked with a dashed black line. The vertical axes are depth, and the horizontal axes are $x$-distance. Plots of the tidal elevation, $\eta$ (c), and depth-averaged currents (d), are also shown at a mid-plume location ($x$ = 5 km, $y$ = 0 km) with max ebb [shown in (a) and (b)] shaded in grey. The dashed lines in (a) and (b) denote the location of the profiles from Fig. 9 whereas in (c) and (d) they mark the times at which profiles 1, 2, and 3 were taken.

plume volume, used to determine *M*, and so result in a closed mixing budget as their summed regions are neither greater than or less than the total plume region.

### 2.4. Results

All experiments exhibit a plume front which exits the estuary near maximum flood currents, with the highest discharge cases just prior to max flood (Fig. 7e) and the lowest discharges just after max flood (Fig. 7a). The plume rotates from north to south with the change in tidal phase after exiting the estuary (Fig. 7b, c, f, g). A salinity intrusion front enters the estuary during flood on all runs, with the intrusion extent dependent on discharge and tidal magnitude (Fig. 7d). The estuary is a salt-wedge in all experiments [$Fr > 0.07$ from Geyer and MacCready (2014)] and a plume lift-off point occurs near the mouth of the estuary where the bottom begins sloping to the shelf.

#### 2.4.1. Plume Structure

A vertical cross section of shear stress, density anomaly, and turbulent buoyancy flux is shown in Fig. 10 to conceptualize the vertical plume mixing structure during low water when ebb tidal currents are strongest. The near-field plume, where generally the strongest interfacial mixing occurs (Horner-Devine et al., 2015), is arbitrarily defined as the region from approximately $x = 0$ km to 4 km, as the most intense in-plume mixing occurs there ($\varepsilon \sim 10^{-4.5}$ m$^2$ s$^{-3}$ and $B \sim 10^{-5}$ m$^2$ s$^{-3}$ at 1 – 2 m depth, Fig. 10). Shear stress peaks in the mid-water column below the plume layer from tidally generated bottom shear ($\tau \sim 10^{-3}$ m$^2$ s$^{-2}$ at 3 – 5 m depth, Fig. 10b) and generally features another local maxima in the near-field plume layer from interfacial instabilities ($\tau \sim 10^{-4}$ m$^2$ s$^{-2}$ when $\sigma_\rho$ = 5 - 20 kg m$^{-3}$ at 0.5 - 2 m depth and $x < 4$ km, Fig. 10b). The multiple maxima in stress suggests interfacial and tidal mixing could both be influential in the near field. Seaward of the near field, no notable areas of enhanced $\tau$ exist in the plume layer, indicating tidal mixing could be more important. This is corroborated by the profile in Fig. 9e (corresponds to dashed line in Fig. 10a, b) where no $d_\tau$ exists and implies tidal mixing is likely dominant during max ebb seaward of the near field. Elevated buoyancy flux values throughout the plume generally occur near or above $d_p$ ($10^{-}$

$^{5.5}$-$10^{-5}$ m$^2$ s$^{-3}$ at 1 - 2 m depth, Fig. 10b) illustrating intense mixing is occurring in the plume, regardless if interfacial-generated shear stress exists. The variable spatial structure of shear stress and buoyancy flux in a moderate tide and discharge plume shows shear and stratification patterns differ, which therefore implies variability in mixing over the interior plume during peak tidal currents.

The variation between tides in each plume is most notable in the horizontal structure of surface salinity and total depth-integrated *B* within the plume layer (Fig. 11). For a large tide ($\eta_{tide}$= 1.5 m) surface salinity is more mixed with ambient salinity (>20 psu relative to 32 psu ambient) beyond the near-field (> 4 km in *x*-distance in Fig. 11a) during maximum ebb currents. During a moderate tide ($\eta_{tide}$=

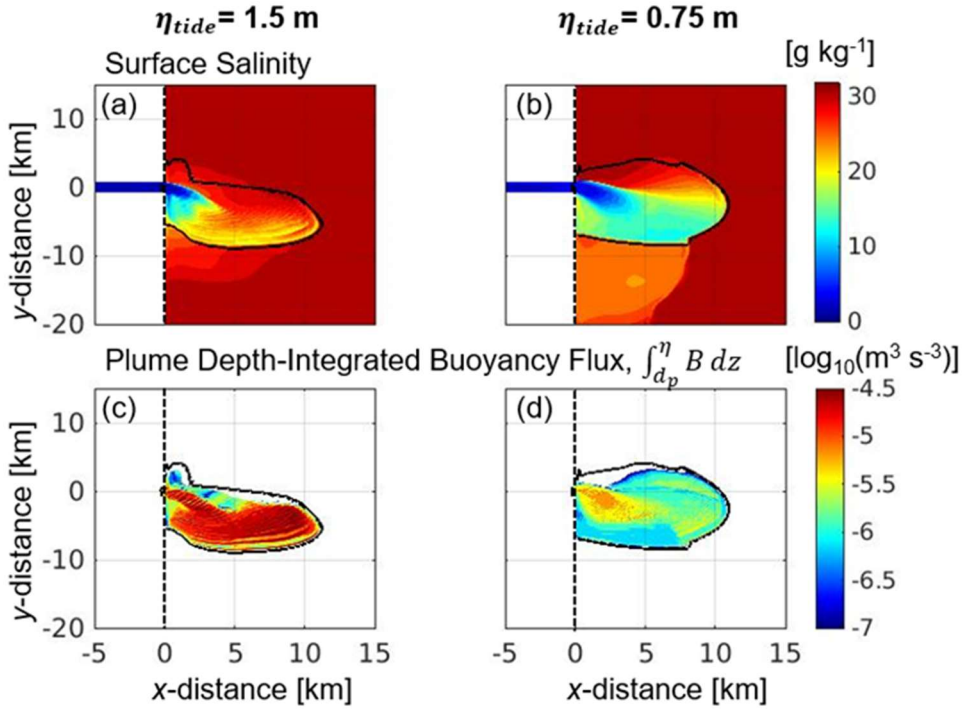


Figure 11: Contours of surface salinity (a, b) and plume depth integrated vertical turbulent buoyancy flux in m$^3$ s$^{-3}$ on a log$_{10}$ scale (c, d) for two $Q$ = 500 m$^3$ s$^{-1}$ runs at max ebb. Left panels (a, c) show the $\eta_{tide}$= 1.5 m run (Fig. 7c) and right panels (b, d) show the $\eta_{tide}$= 0.75 m run (Fig. 7d) with (d) showing the horizonal variation of Fig. 10. Plume boundaries are denoted in each panel as a solid black line. Vertical axes are *y*-distance in km and horizontal axes are *x*-distance in km. Warmer colors in (c) and (d) denote more vertical mixing.

0.75 m), fresher surface water (> 12 psu) exists beyond the near field simultaneously ($x$ > 4 km, Fig. 11b). There is also spatial variation in total mixing within the plume layer between large and moderate tides with the larger tide case showing peak $B$ throughout the plume ($\int_0^{d_p} B\,dz \sim 10^{-5.5} - 10^{-4.5}$ m$^3$ s$^{-3}$, Fig. 11c ) relative to the moderate tide case, where enhanced $B$ ($\int_0^{d_p} B\,dz \sim 10^{-5.5}$ m$^3$ s$^{-3}$, Fig. 11d) was focused in the near-field. The differences in mixing energy terms between each tide and discharge is outlined next to further elucidate the importance of each mechanism.

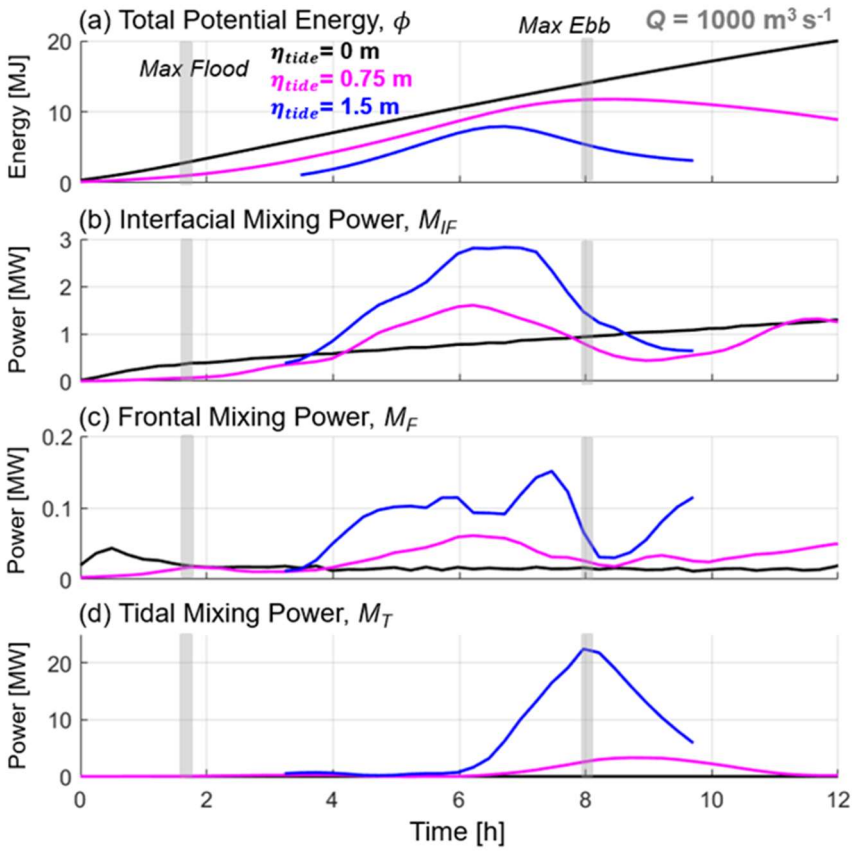


Figure 12: Time varying instantaneous energy budget terms for three $Q$ = 1000 m$^3$ s$^{-1}$ experiments. Total plume potential energy, $\phi$ (a), interfacial mixing power, $M_{IF}$ (b), frontal mixing power, $M_F$ (c), and tidal mixing power, $M_T$ (d). Horizontal axes are time in hours. Blue lines denote $\eta_{tide}$= 1.5 m runs, magenta are $\eta_{tide}$= 0.75 m runs, and black are $\eta_{tide}$= 0 m runs. Max flood and ebb tidal currents are marked with gray shading.

### 2.4.2. Intratidal Variation in Mixing Terms

During the highest river discharge cases ($Q$ = 1000 m$^3$ s$^{-1}$), the tidal maximum in total potential energy (spatial sum of $\phi$) was smallest and occurred earliest (9 MJ, hour 6.5 in Fig. 12a) for the largest tide ($\eta_{tide}$= 1.5 m) relative to the moderate ($\eta_{tide}$= 0.75 m) and no tide ($\eta_{tide}$= 0 m) experiments (11 and 20 MJ at hours 8 and 12, respectively, in Fig. 12a). Larger tides create more mixing within the water column, which limits stratification from increasing over the tidal cycle such as when no tide is present, and the plume continually expands over the shelf. As tidal amplitude increases, stratification levels out, then decreases during maximum ebb currents, indicating an enhanced influence of tides on plume mixing.

$M_{IF}$ and $M_F$ maximize during larger tides then decrease with tidal amplitude similar to $M$, with all cases peaking prior to max ebb. The large tide case is the most significant, with maxima of 3 MW and 0.15 MW near hour 7 (for $M_{IF}$ and $M_F$, respectively) followed by the moderate tide peaking at 1.8 MW and 0.06 MW near hour 6 (for $M_{IF}$ and $M_F$, respectively) (Fig. 12b, c). For all tides, maximum $M_{IF}$ and $M_F$ occur prior to max ebb, when near maximum buoyancy is input to the plume (Fig. 12a), but tidal currents have not yet peaked. The no-tide cases exhibited a small linear increase over the 12-hour duration for $M_{IF}$ and was near constant for $M_F$, both of which were small relative to the tidal plumes (Fig. 12b, c).

Tidal mixing power peaks near max ebb and increases more significantly with tidal amplitude relative to $M_{IF}$ and $M_F$. Maximum $M_T$ for the large tide clearly dominates the other terms for that tidal case (22 MW at hour 8 in Fig. 12d). Maximum $M_T$ then decreases by nearly 5x for the moderate tide and occurs slightly later (4 MW at hour 9 in Fig. 12d). Both tidal runs exhibit peak $M_T$ near max ebb when tidal currents are strongest beneath the plume. When no tide is present, $M_T$ is zero, as expected. $M_T$ exhibits the largest variability in maxima over different tides relative to other mixing terms and notably dominates all mixing terms for the largest tide.

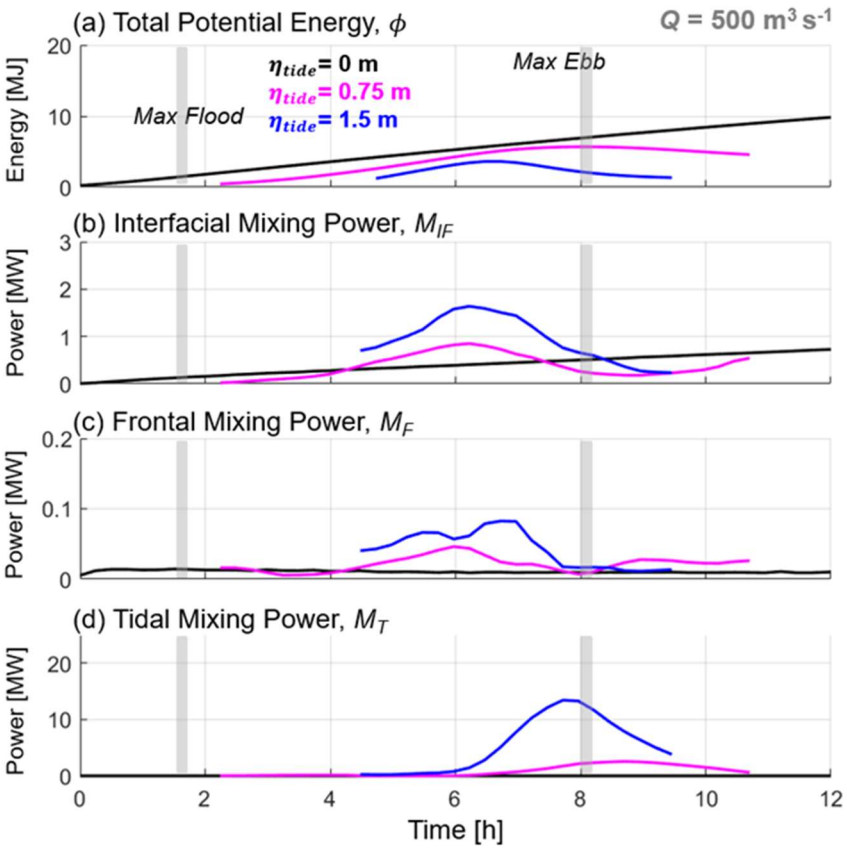


Figure 13: Same as Fig. 12 for $Q$ = 500 m$^3$ s$^{-1}$ experiments.

Under moderate discharge conditions ($Q$ = 500 m$^3$ s$^{-1}$), nearly identical patterns in each potential energy and power term are evident but are weaker in magnitude (Fig. 13). For the moderate tide, peak $M_T$ is comparable to the $Q$ = 1000 m$^3$ s$^{-1}$ counterpart (4 MW at hour 8.5 in Fig. 13d), whereas for the large tide peak $M_T$ is significantly less (13 MW at hour 8.5 in Fig. 13d) and exemplifies how a combination of increased tides and discharge are needed for maximized $M_T$. Smaller discharges ($Q$ = 200 m$^3$ s$^{-1}$ and $Q$ = 100 m$^3$ s$^{-1}$) yield similar trends to those outlined above (not shown).

### 2.4.3. Simplified Budget: Relative Importance of Terms

To synthesize all results and quantify the relative importance of each mixing mechanism through the budget, the experiments were evaluated with nondimensional numbers encompassing both tides and discharge. The Estuarine Richardson number, $Ri_E$, (Fischer, 1972), is used as a basis and is defined as:

$$Ri_E = \frac{g'Q}{Wu_{tide}^3}, \qquad (15)$$

with $Q$ being the freshwater discharge and $u_{tide}$ the tidal current magnitude in the estuary. $Ri_E$ has been linked to vertical structure and bottom-generated sediment transport in plumes (Nash et al., 2009; Spahn et al., 2009). $Ri_E$ can physically be interpreted as the ratio of freshwater transport to tidal power available for turbulent mixing in the estuary. Plumes have also been defined by the dimensional plume-to-crossflow length scale (Jones et al., 2007): $L_x = {g'Q}/{u_a^3}$, where $u_a$ is the ambient velocity. $L_x$ is the scale of influence of the input buoyancy arrested by a crossflow (i.e., how far offshore a plume spreads before a cross-plume current arrests spreading). The spreading of river plumes determines the radial expansion of the near and mid-field plume and is defined as the stretching of a water parcel as it advects through a flow field from strain acting perpendicular to the parcel. In equation form, this lateral spreading is: $\delta = {\partial v}/{\partial y}$ for local flow in the x-direction (Hetland & MacDonald, 2008). To arrest spreading implies that lateral straining is minimized, and the radial expansion of a plume is slowed or stopped. Therefore, in this application $L_x$ is the length scale of the tidal plume arrested by tidal crossflow on the shelf. Thus $Ri_E$ can also be interpreted as the ratio of the length, $L_x$, to the mouth width which traditionally scales in size with the near-field plume, assuming $u_a = u_{tide}$.

Some estuary-plume systems exhibit much different magnitudes in tidal currents once outside the estuary, and the tidal mixing implied by $Ri_E$ may not apply beyond the mouth. To make a stronger connection between tidal mixing outside the estuary and a plume length scale, we multiply $Ri_E$ by the inverse of the Rossby number and quantify $u_{tide}$ as an average of tidal currents beneath the plume on the shelf:

$$Ri_E R_0^{-1} = \frac{g'Q}{Wu_{tide}^3}\frac{W}{R_I} = \frac{g'Q}{R_I u_{tide}^3}, \qquad (16)$$

where the plume inertial radius is $R_I = {}^{U}/_{f}$ and has been found to scale with plume spreading (Kakoulaki, 2015; Kakoulaki et al., 2020). Physically, the nondimensional Equation 9 modifies our interpretation of the Estuary Richardson number to be the ratio of freshwater transport to tidal power available for turbulent mixing *under the plume*, with the plume tidal power now scaling with plume spreading. We believe this formulation is more suitable for the full extent of the tidal plume than the mouth width scaling applied in Equation 15.

$Ri_E$ and $Ri_E R_0^{-1}$ were calculated for each experiment then averaged over the 12-hour tidal period (denoted with $\langle \quad \rangle$) (Table 1). The ratio of each cumulative power term to the cumulative total power (Eq. 10) over the time the plume is attached to the estuary ($\sum M_x / \sum M$, with $x$ representing the various mechanisms) was then compared to $\langle Ri_E R_0^{-1} \rangle$ to identify the relative importance of each mixing mechanism to total plume mixing over the tidal plume's duration (Fig. 14). For all $\langle Ri_E R_0^{-1} \rangle < 1.3$, tidal mixing power is the dominant mechanism in the energy budget, ranging from 55% to 90% of the total mixing energy, with interfacial mixing accounting for 10% to 40% of the budget. Based on Equation 16, $\langle Ri_E R_0^{-1} \rangle = 1$ marks the theoretical threshold between a plume generally uninfluenced by tidal crossflow ($> 1$) and one that is arrested and significantly mixed by the tidal crossflow ($< 1$). Cases when $L_x$ is on the order of or larger that $R_I$, other mechanisms may be dominant in the mixing budget ($\langle Ri_E R_0^{-1} \rangle > 1$), which is near the 1.3 observed here. Similar to theory, these results show when $\langle Ri_E R_0^{-1} \rangle > 1.3$ mixing energy dominance shifts to interfacial mixing (ranging from 55% to 95%) and tidal mixing decreases in importance from 40% to less than 5% of total mixing. For all cases, frontal mixing contributes the least to total mixing (<10%). Collectively, Fig. 14 shows plumes with relatively enhanced tidal influence (smaller $\langle Ri_E R_0^{-1} \rangle$) experience a significant $M_T$, whereas plumes with enhanced freshwater influence (larger $\langle Ri_E R_0^{-1} \rangle$) experience a more significant $M_{IF}$. Frontal mixing has a slight increase in importance for larger $\langle Ri_E R_0^{-1} \rangle$ but to a negligible degree relative to interfacial mixing.

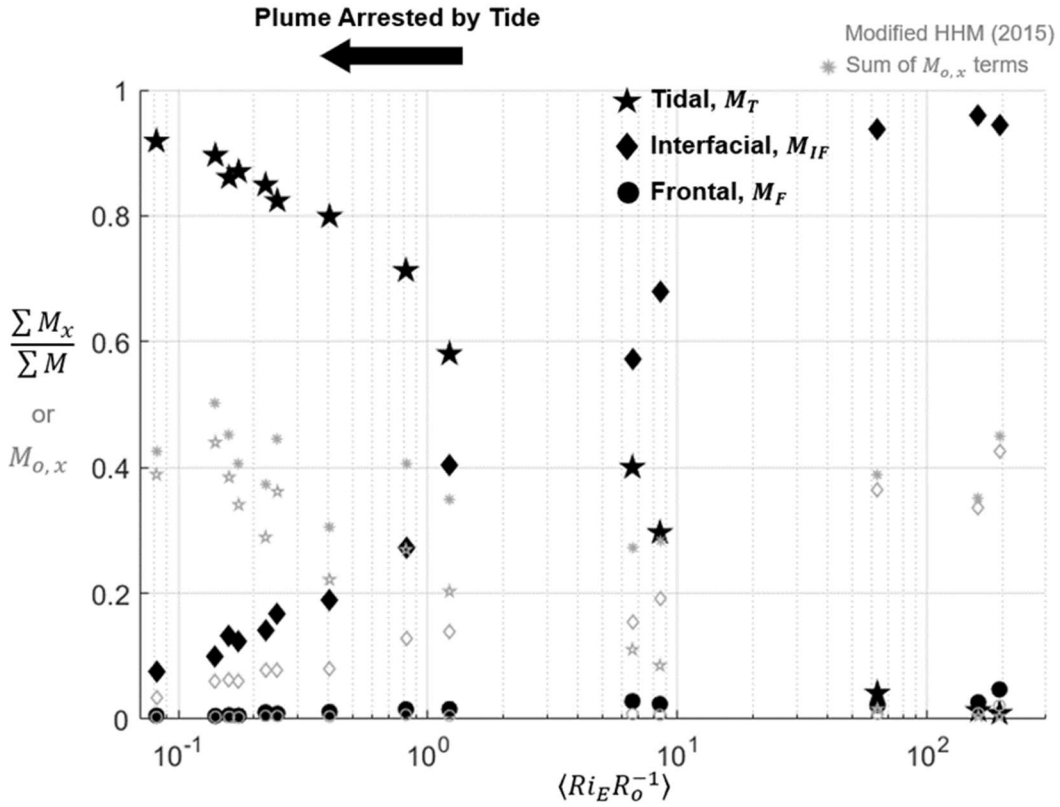


Figure 14: Ratio of each tidally summed mixing power term to summed total input power, $\sum M_x / \sum M$, with *x* changing with the following terms: tidal mixing power, $M_T$, is denoted by stars, interfacial mixing power, $M_{IF}$, by diamonds, and frontal mixing power, $M_F$, by circles. Vertical axis is the dimensionless ratio and horizontal axis is the tidally averaged dimensionless estuary Richardson number multiplied by the inverse Rossby number, $\langle Ri_E R_o^{-1} \rangle$, on a $\log_{10}$ scale. An icon in $\langle Ri_E R_o^{-1} \rangle < 1$ denotes a plume generally arrested by the tide. Icons in gray are estimates of each $M_{o,\,x}$ from the modified HHM (2015) method, with the sum of each $M_{o,\,x}$ term denoted with a gray asterisk.

**2.5. Analysis**

River plume dilution controlled by tidal mixing has not been investigated before in surface advected plumes. Although the influence of interfacial mixing is not always dominant in these experiments, the relative importance of the mechanism (10% - 40% for tidal runs) is quite close to some of the more robust estimates of interfacial near-field mixing in-situ (Kilcher et al., 2012; MacDonald et al., 2007). These results help advance our understanding of both mechanisms. To better grasp how tidal

mixing can become so large relative to the other mixing terms, we explore estuary and plume dynamics associated with the Estuarine Richardson number and plume lengths scales, then decompose the spatial variability of mixing dynamics for the experiments featuring the largest $M_T$.

### 2.5.1. Tidal vs. Interfacial Mixing: $Ri_E$ and $R_o$

Prior research has made the connection between deeper, bottom-boundary interacting plumes and tidal mixing through $Ri_E$. Nash et al. (2009) found that plume salinity, thickness, and mixing at the base all increase as $Ri_E$ decreases (i.e., tidal currents increase). Essentially, a strongly sheared estuarine outflow creates a more mixed, deeper-reaching plume that is prone to interact with the bottom-boundary layer. Consistent with Nash et al. (2009), for all discharges, increasing tidal amplitudes subsequently decreased $\langle Ri_E \rangle$ and our spreading-scaled $\langle Ri_E R_0^{-1} \rangle$, implying an enhanced mixed layer at the plume base within the estuary and over the shelf. The maximized $\sum M_T / \sum M$ which corresponded to those $\langle Ri_E \rangle$ and $\langle Ri_E R_0^{-1} \rangle$ values quantified the expansion of the mixed layer. Conversely, the discharge-dominated plumes (large $\langle Ri_E R_0^{-1} \rangle$) resulted in more interfacial mixing because of stronger stratification and shear in the plume layer which was not greatly influenced by tides (similar to Fig. 8a). Since plume spreading is a driving mechanism which allows for enhanced interfacial mixing (Hetland, 2005), we propose that plume spreading is significantly halted as $\langle Ri_E R_0^{-1} \rangle$ decreases below unity. The along-shore tides created in these simulations effectively disrupt the spreading-interfacial mixing balance for larger tidal amplitudes, as the tidal barotropic pressure gradient likely overtakes those at the river mouth and turns the plume downcoast. Spreading is further inhibited as shear from tidal processes contributes excess mixing to the plume and the alongshore tidal currents dominate plume transport relative to much smaller across shore currents (Fig. 7). This tidal influence on near-field evolution is visually evidenced by the tidally-advected, asymmetric bulge shape shown in Fig. 7 that clearly diverges in along and cross shore scales from the classically non-tidal, radially-spreading bulge from literature (Hetland, 2005). Intratidal variability shown in Figs. 12 and 13 reveal all $M_{IF}$ curves peak prior to max ebb then minimize at max ebb when spreading

is arrested. As spreading is reduced, shear at the plume interface and the associated mixing is minimized, and other mechanisms (tidal) become relatively more influential.

### 2.5.2. Tidal vs. Interfacial Mixing: Spatial Scales

Bottom-generated mixing is not typically considered an efficient mixing mechanism on pycnoclines in strongly stratified systems (Holleman et al., 2016) which calls that mechanism into question. To investigate further, vertical sections of $B$, $\tau$, shear production, $P = -\overline{u'w'}\left(\frac{\partial u}{\partial z}\right) - \overline{v'w'}\left(\frac{\partial v}{\partial z}\right)$ (where $\overline{u'w'}$ and $\overline{v'w'}$ are the Reynold's stresses in the $x$ and $y$ directions, respectively), and a plot of $\phi$ during a large tidal mixing experiment ($Q$ = 1000 m$^3$ s$^{-1}$, $\eta_{tide} = 1.5$ m) is shown at two interior plume locations to identify how interfacial and tidal mixing contributions change with increasing tidal currents (Fig. 15). The plume depth marked by dye (dashed line, Fig. 15a) can be related to the local minimum in shear stress (dotted line, Fig. 15b) to elucidate when interfacial mixing dominates relative to tidal. At a centralized plume coordinate just beyond the near field ( $x$ = 5 km, $y$ = 0 km, left panels in Fig. 15) $d_\tau$, and therefore interfacial mixing, exists only prior to max ebb when $P$ and $\tau$ are small near-bottom ($P \sim 10^{-7}$ m$^2$ s$^{-3}$ and $\tau \sim 10^{-5}$ m$^2$ s$^{-2}$, hours 5 – 6, Fig. 15b, c). Simultaneously, a relatively stratified plume layer exists in the top few meters of the water column ($\phi$ = 100 J, Fig. 15d). $d_\tau$ generally, is at the same depth as $d_p$ at that time, implying that interfacial mixing controls plume dilution during slack water with negligible tidal mixing. As the tide progresses, $P$ and $\tau$ increase near bottom ($P \sim 10^{-4}$ m$^2$ s$^{-3}$ and $\tau \sim 10^{-3}$ m$^2$ s$^{-2}$, Fig. 15b, c) and expand upward to the surface (hours 6 to 7.5). Concurrently, $d_\tau$ disappears, the plume thickness expands to near the bottom, and the stratified plume-ambient interface mixes into a more uniform, intermediate density class ($\sigma_\theta$ ~20 to 22 kg m$^{-3}$, Fig. 15c) which extends to near bottom and becomes much less stratified ($\phi$ = ~25 J, Fig. 15d). Buoyancy flux is maximized for the tidal cycle at this time (hours 6 to 7.5), and interfacial mixing does not exist, implying plume mixing transitions to a strong tidally mixed regime relative to the time of slack tidal currents. As the tide approaches max ebb, the water

column is vertically homogenized and the plume fully mixed with the ambient ($\phi$ ~ 0 J at hour 8, Fig. 15d).

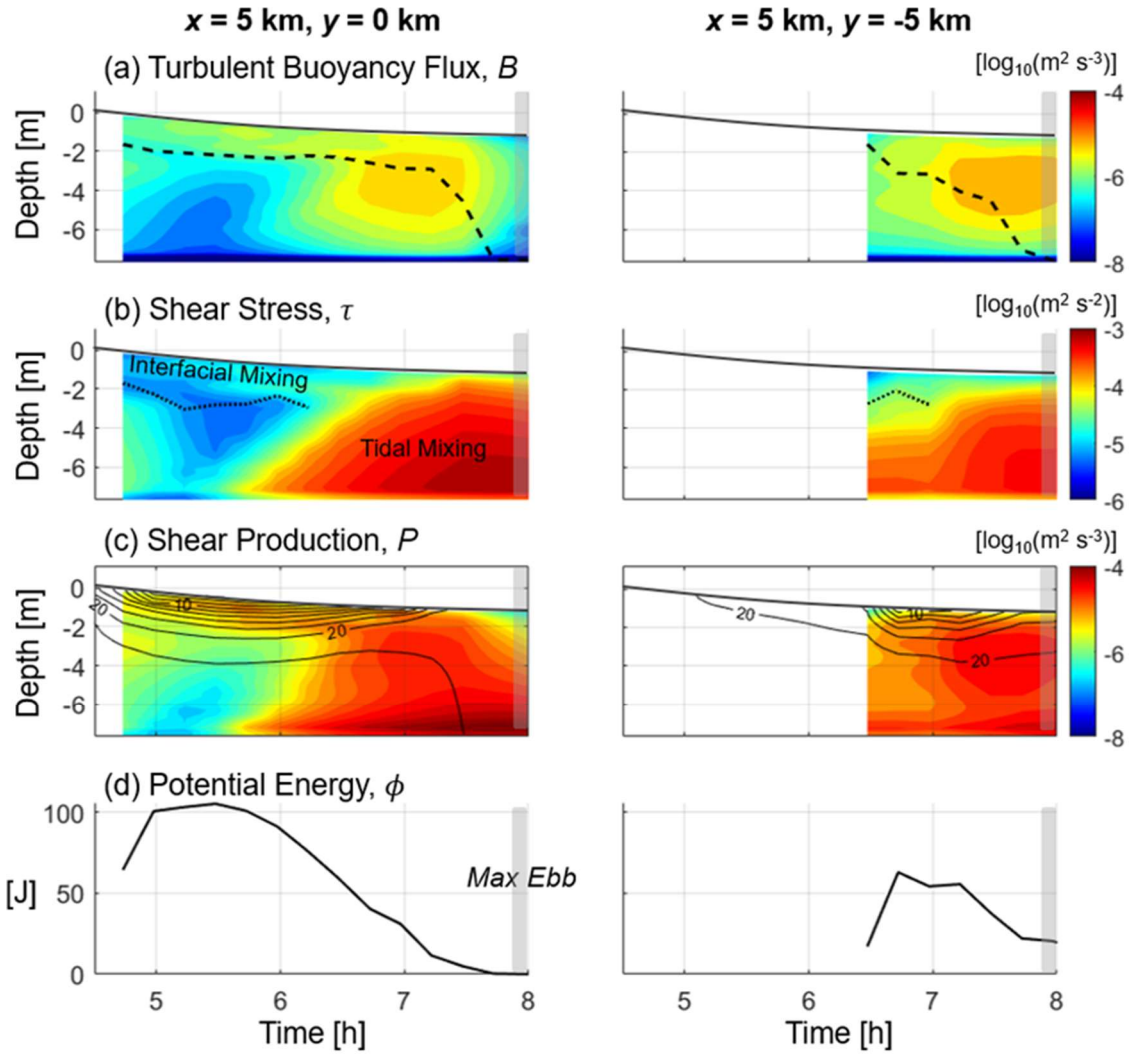


Figure 15: Filled contours of vertical turbulent buoyancy flux and plume depth (dashed line) (a), shear stress and shear stress local minimum (dotted line) (b), shear production (c), and line plot of water column potential energy (d), at $x$ = 5 km, $y$ = 0 km (left panels) and $x$ = 5 km, $y$ = -5 km (right panels) near low water when $Q$ = 1000 m$^3$ s$^{-1}$ and $\eta_{tide}$= 1.5 m. $Y$-axis is depth, in meters, and $x$-axis is time, in hours, for each subplot. All color bars are on a $\log_{10}$ scale. Max ebb is marked with a gray box and the free surface with a black line. Contours of density anomaly, $\sigma_\theta$, in 2 kg m$^{-3}$ intervals are shown as solid black lines on panel (c) with 10 and 20 kg m$^{-3}$ labeled.

At a separate, downcoast location ( $x$ = 5 km, $y$ = -5 km, right panels in Fig. 15), the same general patterns occur after a later plume arrival time (~hour 6.5 when contours begin). Tidal mixing dominates (Fig. 15b, c) and the plume thickness expands to near bottom (Fig. 15a), but the plume layer remains stratified enough to not mix away completely (minimum $\phi$ ~25 J, Fig. 15d). An asymmetry in $\phi$ is therefore created, with the up-coast edge of the plume well mixed and weaker mixing on the downcoast side. We suspect the up-coast side of the plume is more susceptible to tidal mixing because the ambient waters approaching from that direction lack stratification, as demonstrated by larger salinity values up-coast of the plume during max ebb (~32 g kg$^{-1}$) in Fig. 7. The heterogeneity in shelf stratification allows the mixed water beneath the plume to flow away and be replaced with the near-ambient waters from outside the plume and quickly decrease $\phi$. Downcoast, this effect is less defined as the mixed plume water class accumulates beneath that section of the plume, always allowing stratification to exist.

A decomposition of plume depth relative to total water depth in the horizontal extent (Fig. 16) corroborates the spatial patterns identified in Fig. 15. Contours of $d_p/(H+\eta)$ can be interpreted as the portion of the water column the plume comprises, with 1 indicating a plume mixed to the bottom. $d_p/(H+\eta)$ and $\phi$ for a relatively strong tidally mixed plume (Fig. 16a, b, c) are compared to a weaker tidal mixing experiment (Fig. 16d, e, f) during ebb. All regions of active interfacial mixing were flagged (anywhere $d_\tau$ is present, not shown), as were regions of active tidal mixing (no $d_\tau$ exists, not shown). For the significant tidal mixing scenario, a large portion of the plume footprint mixes to the bottom during maximum ebb currents at hour 8 and is biased to the upcoast side (Fig. 16a, b, c). For the moderate tide, only a small region (< 3 km) beyond the estuary mouth mixes to the bottom (Fig. 16d, e, f). Relatively large $\phi$ (> 70 J) and the existence of $d_\tau$ (not shown) near the mouth for all snapshots indicates a larger, bottom reaching mixed layer exists beneath a still relatively fresh, surface plume layer (Fig. 8c) which is mixed through interfacial and tidal mechanisms. Beyond the mouth and near-field, the regions which deepen or mix to the bottom exhibit smaller $\phi$ (0 to 20 J) and mixing is mostly tidal (no $d_\tau$) or frontal (Fig. 16c). Further, interfacial mixing dominates spatially around slack water (71% to 90% of the area,

Fig. 16a, d) but tidal mixing takes over spatial dominance only as currents increase (70% to 85% of area, Fig. 16b, c, e, f). Plumes feature a larger spatial extent of tidal mixing for a larger tidal amplitude relative to smaller amplitudes (larger % tidal mixing in Fig. 16a, b, c than Fig. 16 d, e, f). In all cases, tidal mixing never completely takes over in the near field, where discharge momentum likely allows spreading and interfacial mixing to continue, and near the leading front, where stratification maintains ($\phi$ > 80 J in all snapshots). Stratification is always greatest at the leading, downcoast plume front ($\phi$ = 80 – 100 J) and is weakest on the following, up-coast front ($\phi$ = 0 – 20 J), reinforcing the patterns identified in Fig. 15.

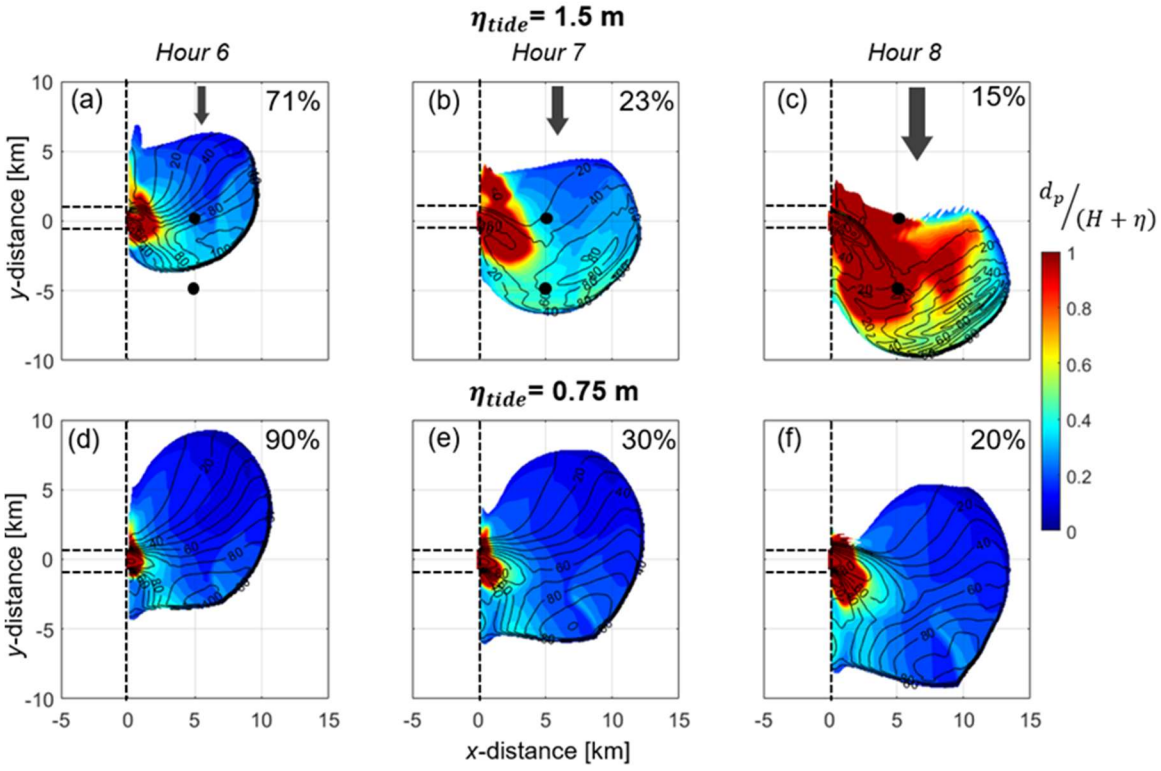


Figure 16: Filled contours plume depth ($d_p$) normalized by total water depth ($H + \eta$) and labeled contours of $\phi$ (in Joules) for $Q$ = 1000 m$^3$ s$^{-1}$, $\eta_{tide}$= 1.5 m (a – c) and $\eta_{tide}$= 0.75 m (d – f) experiments. Snapshots show hour 6 (a, d), hour 7 (b, e), and hour 8 (c, d) as ebb tidal currents increase. The spatial percentage of active interfacial mixing, based on $d_\tau$ (not shown), is denoted for each plot. Vertical axes are *y*-distance in km and horizontal axes are *x*-distance in km. Current direction is denoted by the dark gray arrows, and general magnitude with arrow size. Black dots represent the locations of the time series from Fig. 15.

The asymmetric distribution of stratification and position of the plume observed in these experiments are likely also a result of straining and advection of the freshwater discharge and are briefly mentioned here. Straining can enhance or reduce vertical stratification through velocity shears deforming a water parcel, while advection moves the stratified water column via a depth averaged current. Former research on the Rhine river plume (also strongly tidally modulated) consider alongshore straining and advection to be important drivers of the time evolution of $\phi$ in the near and midfield plume (de Boer et al., 2008). Drawing loose comparisons to this work, it is likely that tidal straining is enhanced on both upcoast and downcoast sides of the plume footprint (excluding nearfield and seaward of it) because of significant horizontal density gradients and vertical shear (de Boer et al., 2008). Advection driven by tidal currents then pushes that strained water column into the interior or downcoast side of the plume, moving the plume and simultaneously enhancing stratification downcoast (Fig. 16). We suspect straining and advection driven increases in stratification is why tidal mixing cannot quite dominate the water column downcoast of the mouth.

### 2.5.3. On the Effect of Ambient Stratification

Figs. 15 and 16 shows plumes generally controlled by tidal mixing which can correspond to a sharp decrease in stratification in the water column. It is apparent that the intermediate density class associated with "old" plume water ($20 < \sigma_\theta < 22$ kg m$^{-3}$ beneath $d_p$ in Fig. 15c) plays a part in enhancing the buoyancy flux sub-plume (~ 4 m deep, Fig. 15a) as bottom stresses increase. Near-surface plume water mixes to that buoyancy after the plume interface deteriorates. Ultimately, although buoyancy flux from old plume stratification likely aided in the decay of the plume interface by weakening stratification between the layers, it was deemed insignificant in contributing excess mixing to $M_T$ within the plume itself (Appendix B). Although the simple evaluation provided in Appendix B suggests the effect of ambient stratification is small on a strongly stratified tidal plume, the net influences from old plumes or coastal currents could be notable in some systems, and undoubtedly modifies mixing in some way. It is likely those effects would present themselves more clearly in plumes which originate nearer in salinity to

the ambient shelf, or plumes analyzed at longer time scales than a single tide. Investigating the influence of ambient stratification on plume mixing mechanisms is a worthy topic to investigate in the future. However, for the tidal plumes presented here, we attribute bottom-generated shear production coupled with tidal currents arresting plume spreading as the main destructive mechanisms reducing near-surface shear at the plume interface and homogenizing shear throughout the water column (hours 6 to 6.5, Fig. 15b). Bottom generated shear instabilities then mix the plume stratification and destroy the plume interface, evident in the patterns of $P$ and $\phi$ discussed, which subsequently kills interfacial mixing, connects the plume to the bottom boundary layer, and mixes the plume, sometimes completely away on the sides exposed to strictly ambient currents (upcoast in these simulations). For the relatively weaker tide experiments, interfacial mixing covers a larger spatial extent of the plume and bottom generated $P$ and $\varepsilon$ are weaker and less efficient at mixing near-surface plume waters (not shown).

## 2.6. Discussion

### 2.6.1. Comparison to Theory

A theoretical ratio was developed in Horner-Devine et al. (2015) [hereby called HHM (2015)] to more accurately depict the mixing budget framework of Pritchard and Huntley (2006) and is similar to the ratio we present in Fig. 14. The HHM (2015) ratio, $M_o = 2\frac{BA}{g'_f Q}\gamma T^*$, approximates the rate of energy converted to mixing due to a specific process relative to the total energy required to mix the freshwater discharge from an initial density to a mixed ambient condition (differing from the total plume mixing over a tidal pulse we compare to in Fig. 14). In that estimate, $A$ is the horizontal area over which a buoyancy flux, $B$, acts, $T^*$ is the nondimensional fraction of time mixing occurs over, $Q$ is discharge, and $\gamma = g'_M\left(g'_f - g'_M\right)^{-1}$ with $g'_f$ being the initial freshwater reduced gravity and $g'_M$ is a final mixed reduced gravity. We modified the HHM (2015) mixing ratio to apply to model output by taking a time and volume integral of $B$, and tested it on these data as:

$$M_{o,x} = \frac{2\iint BdVdt}{g'_f Qht}\gamma \qquad (17)$$

where $x$ denotes the mixing process being analyzed ($F$ = frontal, $IF$ = interfacial, and $T$ = tidal), $h$ is the spatiotemporal average of plume depth, and $t$ is the time period being analyzed (12 hours in these runs). Estimates of $M_{o,x}$ are compared to $\frac{\sum M_x}{\sum M}$ in Fig. 14.

The relative importance of each mixing mechanism according to Equation 17 is generally just under half of $\frac{\sum M_x}{\sum M}$ estimates with the same general trends holding (Fig. 14). For small $\langle Ri_E R_o^{-1} \rangle$, tidal mixing ($M_{o,T}$) dominates and causes roughly 40% of plume mixing over a tidal cycle. For the largest $\langle Ri_E R_o^{-1} \rangle$, tidal mixing is near zero and $M_{o,IF}$ dominates with estimates at roughly 40%. The net sums of $M_{o,T}$, $M_{o,F}$, and $M_{o,IF}$ vary from 0.3 to 0.5 and imply that each plume created in these experiments does not completely mix out over one 12 hour tide but rather is mixed about half-way to ambient conditions. This suggests the remaining 50 – 70% of plume mixing occurs in the far-field plume at time scales beyond one tide. The estimates based on HHM (2015) provide context for the results of this work which give us a better understanding of the importance of plume mixing mechanisms on multiple time scales.

### 2.6.2. Applicability to Other, Tidally Pulsed Plumes

In many plume systems, the contribution to mixing from tidally generated bottom friction has been unknown or assumed negligible relative to interfacial and frontal processes. To put other shelf-plume systems in the context of this work, in Figure 17 we normalize $L_x$ and $R_I$ by the deformation radius $R_d = \sqrt{g'h}/f$, presenting the mouth Froude number, $R_I/R_d = U/\sqrt{g'h} = Fr$, to characterize plumes. The Froude number, which relates plume input buoyancy to inertia, tends to increase with relatively higher discharge surface advected plumes that emerge from more time dependent salt wedge-like estuaries (Yankovsky & Chapman, 1997). Note that $R_I \sim R_d$ is a critical plume, e.g., Fr ~1, and therefore the metric $L_x/R_d$ can be interpreted similarly to $Ri_E R_0^{-1}$ as a comparison of the plume to crossflow length scale to plume cross-shore length scale. Figure 17 illustrates when tidal mixing may be more important than interfacial mixing (i.e., tidal mixing mixes away most input buoyancy below the $Ri_E R_0^{-1}$=1 line).

Since *Fr* was approximated for each system with discharge and mouth geometry from literature, both axes contain discharge as input and so all approximation boxes in Fig. 17 slope similarly to the $Ri_E R_0^{-1}$=1 line.

$\langle Ri_E R_0^{-1} \rangle$ estimates are calculated using typical dry to wet season river discharges and spring to neap tidal ranges. Estimates are shown for the Fraser River plume (Halverson & Pawlowicz, 2008;

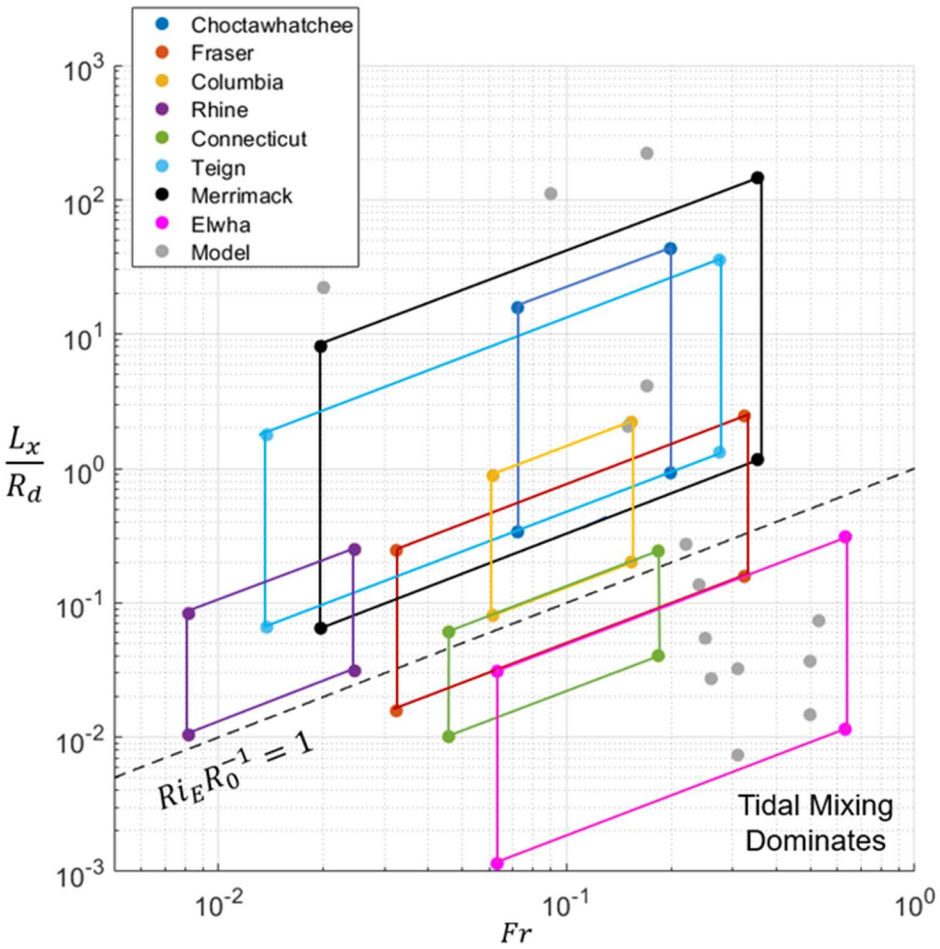


Figure 17: Conceptual diagram showing the possible importance of tidal mixing on other river plume systems. Systems are plotted based on the ratio of plume-to-crossflow length scale to the Rossby radius of deformation (vertical axis on a $\log_{10}$ scale) and mouth Froude number range (horizontal axis on a $\log_{10}$ scale). Each box represents a possible range of values based on spring to neap tidal variation and average to high river discharge cases. The parameter space of this work is plotted as the individual gray dots. Based on the results of this work, tidal mixing energy is prone to dominate the mixing energy budget when near or below the dotted 1:1 line shown ($Ri_E R_0^{-1}$=1).

Kastner et al., 2018), the Columbia River plume (Akan et al., 2018; Spahn et al., 2009), the Rhine ROFI (Flores et al., 2017), the Choctawhatchee Bay plume (Huguenard et al., 2016), the Connecticut River plume (Holleman et al., 2016; Whitney et al., 2016), the Merrimack River plume (Hetland & MacDonald, 2008), the River Teign plume (Pritchard & Huntley, 2006), and the Elwha River plume (Warrick & Stevens, 2011). The Connecticut and Elwha plumes, both of which exhibit shallow discharges and intense tidal modulation, are likely often dominated by tidal mixing. In the Columbia, Rhine, and Fraser River plumes, which all have variable discharges throughout the year, tidal mixing is likely important during some periods. In the Merrimack, River Teign, and Choctawhatchee Bay plumes, tidal currents are relatively weak over the shelf and tidal mixing is likely not important ever. Tides along more realistic, variable bathymetry of the plume systems listed will force a current ellipse different than what we see in these experiments with simple bathymetry and may have a different effect on the tidal mixing term in the energy budget. Further, differences in shelf slope beneath each plume would likely create spatial differences in tidal mixing which are not captured by the depth and spatial average of tidal currents utilized in calculating the nondimensional numbers of Fig. 17. Plumes over steep shelf slopes may experience weakened tidal mixing due to a diminishing bottom boundary layer relative to total water depth. Results from the relatively gradual slope utilized in these simulations suggest tidal currents are slightly more effective at mixing plumes deeper into the water column nearer to shore in the shallow regions (Fig. 16). Nonetheless, these results provide a general framework which shows when tidal mixing could be more important than interfacial and frontal mechanisms.

### 2.6.3. Frontal Mixing

Another noteworthy result of this work is the relative weakness of frontal mixing to interfacial and tidal processes in all experiments. The contribution of frontal mixing to a mixing budget has been highly uncertain. Estimates range from 100% (Pritchard & Huntley, 2006) to 60% (Huguenard et al., 2016) to 20% (Orton & Jay, 2005) and even less (Cole et al., 2020). The results of this work are most

nearly consistent with that of Cole et al. (2020), as frontal mixing never surpasses 10% of the total budget.

Frontal mixing is the mechanism least sensitive to changes in tide and discharge (Fig. 14), emphasizing that it never becomes important to the budget. Mixing magnitudes in the modeled front were often comparable to elsewhere in the plume (see Fig. 10b) meaning frontal mixing is likely sensitive to the plume area defined as the frontal zone, for which a definition will be more thoroughly addressed in future work. That area was small in all the experiments presented here relative to the remainder of the plume, even with the multiple liberal calculations of the frontal zone width which we employed. It is likely that smaller spatial scale plumes would exhibit a more important frontal mixing term within the budget, more in line with results from Pritchard and Huntley (2006). That said, frontal mixing may include significant convective instabilities which are not captured in this hydrostatic study. Applying a similar study to a non-hydrostatic model would offer more clarity and is an important topic for future research. Although determined from a hydrostatic model, these results still provide robust, synoptic estimates relative to the existing observed and heavily extrapolated point estimates reported in literature.

### 2.7. Conclusions

Tidal mixing has the potential to dominate the mixing budget of tidally pulsed meso/macrotidal river plumes for relatively large tides. Tidal mixing powers are between 50% and 90% of the total mixing for tidal amplitudes that successfully arrest plume spreading ($\langle Ri_E R_0^{-1} \rangle < 1$) whereas interfacial mixing is typically 10% to 40% of mixing for those plumes. Interfacial mixing dominates the budget when spreading is not arrested by tides, accounting for 50% to 95% of the budget. Frontal mixing never dominates the budget in this study, and never exceeds 10% of the total mixing energy. This is the first study to suggest that tidal mixing can exceed that of interfacial and frontal processes and is caused when bottom-generated shear production coupled with tidal currents arresting plume spreading reduce near-surface shear at the plume interface and homogenize shear throughout the water column. Tidal mixing within the plume may therefore be an important mechanism in determining total shelf mixing and

circulation in meso/macrotidal regions influenced by surface advected plumes. The results of this work are thus important to consider for future modeling of river-sourced pollutants and tracers into the ocean.

# CHAPTER 3

# WIND EFFECTS ON NEAR- AND MID-FIELD MIXING IN TIDALLY PULSED RIVER PLUMES

## 3.1. Introduction

The discharge of river-borne water into the coastal ocean is subject to a variety of physical processes which mix fresh and salty water. Mixing dictates pollutant, nutrient, and sediment fate and so can influence coastal ecological health. In general, plumes mix into the coastal ocean by wind, waves, tidal processes, and frontal shear and convergence at plume interfaces (Horner-Devine et al., 2015). Although great advances have been made in recent years observing and modeling plumes, there is still significant uncertainty regarding the importance of mixing mechanisms spatially and temporally in plumes exposed to different environmental conditions.

Coastal winds are a notable environmental condition controlling plume dynamics. Winds can modify circulation patterns over the shelf, which in turn modulate river plume dynamics outside the estuary. Extensive numerical and analytical work have determined upwelling and downwelling favorable wind events, created via along-shelf wind stresses, are important to the vertical and horizontal extent of plume structure and mixing. Upwelling winds often thin plumes and advect them offshore via Ekman transport, leading to significant mixing because of increased vertical shear in horizontal currents (Fong & Geyer, 2001; Lentz, 2004; Whitney & Garvine, 2005). Downwelling winds can augment down-shelf currents, attach plumes to the shore, and subsequently mix the water column by entraining ambient waters into the plume (Moffat & Lentz, 2012; Whitney & Garvine, 2005) or by inducing cross-shore upwelling circulation within the coastal-trapped current (S. Y. Chen & Chen, 2017). Recently, modeling work has expanded to test the impact of cross-shelf winds (Jurisa & Chant, 2013; Tilburg, 2003; Zhang et al., 2014) to plume mixing, finding mixing to be typically determined by the cross-shore advection of salt and the downstream transport of freshwater. However, the research related to along and cross-shelf winds generally focus on large time scale (multiple days) Ekman responses or idealized wind forcing. Realistic

winds are often short in duration and variable, and can create plume responses which differ from large scale Ekman theory (Hunter et al., 2010). It is yet to be determined how important to mixing and stratification realistic, shorter time scale wind forcing can be in smaller, tidal time scale plumes, particularly in their often energetic near and mid-field regions.

Tidally pulsed plumes occur in regions with significant tidal energy, creating an estuary discharge dominated by tides and discharge momentum flux (e.g., the Connecticut River and River Teign plumes). Generally, this manifests as a "new" surface-advected plume every ebb tide which spreads over denser shelf waters. Unlike larger, non-tidal plumes (e.g., the Mississippi River and Amazon River plumes), the dynamic near and midfield regions of tidally pulsed systems often form and evolve on a tidal time scale which creates intratidal variability in dynamics (Horner-Devine et al., 2015). The nearfield is defined as the region near the river mouth where estuary discharge momentum dominates dynamics and generally features the most intense mixing at the very sheared and stratified plume base (Hetland & MacDonald, 2008; MacDonald et al., 2007). The midfield marks the region when Earth's rotation becomes influential and starts turning the plume downcoast of the river mouth (Garvine, 1987; Horner-Devine et al., 2015). Preliminary mixing budgets in tidally pulsed plumes have estimated nearly 50% of mixing during a tidal pulse occurs within the near and midfield plume (chapter 2), outlining the importance of these energetic regions to net plume mixing. The nearfield is considered particularly sensitive to tides (Nash et al., 2009; Spahn et al., 2009) and so wind effects there are often considered negligible in tidal plumes (Horner-Devine et al., 2009). It is in the midfield that wind effects are generally thought to become important in response to longer time scale Ekman dynamics. Recent observations in the tidal Merrimack River plume indicate that tidal time scale, nearfield transport is more sensitive to local winds than previously assumed and it is hypothesized that mixing is sensitive to wind as well (Kakoulaki et al., 2014).

At present, a handful of observational studies have investigated plume dynamics in the near and midfield of tidally pulsed plumes under realistic wind forcing (Flores et al., 2017; Kastner et al., 2018; Rijnsburger et al., 2018). Notably, a drifter observational program performed by Kastner et al. (2018) was

the first to estimate mixing along streamlines in the near and mid-field Fraser River plume under realistic winds. Markedly different mixing regimes were determined based on wind direction which the authors attribute to modifications in plume geometry. Although novel, the former work is restricted in spatial and temporal resolution which limits the diagnosis of mixing mechanisms. Further, wind effects on one particular tidal plume are not connected to the dynamics of succeeding plumes. As of yet, a direct evaluation of plume mixing mechanisms on a tidal time scale under varying, realistic winds has yet to be achieved, particularly for successive tidal pulses.

Quantifying direct relationships between the formation and fate (transport and/or mixing) of stratification generally provide a more complete evaluation of mixing in coastal systems. Multiple techniques have been utilized in recent years to better quantify the evolution of stratification. Budgets based on the buoyancy flux and potential energy anomaly (PEA) equation (Burchard & Hofmeister, 2008; J. H. Simpson et al., 1990) have been popularly used. Although useful, the PEA methods applied to river plumes are often complicated to formulate (de Boer et al., 2008) or indirectly relate the formation of stratification to mixing (Pritchard & Huntley, 2006). The salinity variance equation has recently become a more widely accepted and refined method to evaluate stratification and mixing (Burchard & Rennau, 2008; Li et al., 2018; MacCready et al., 2018; Warner et al., 2020), but has mainly been applied to estuaries. The salinity variance approach is simple in formulation and allows for direct comparisons between net changes in stratification to transport (advection) and destruction (dissipation / mixing) of stratification. Further, the transformation of salinity variance model (Li et al., 2018) adds an additional term which quantifies the creation of stratification through straining of horizontal density gradients. This technique allows for robust spatial and temporal variability in advection, mixing, and straining to be determined and has yet to be applied in analyzing a tidally pulsed river plume.

In this paper, we study the Merrimack River plume, a surface advected tidal plume which spreads and mixes into the Gulf of Maine. The gently sloping, uncomplicated, and shallow shelf bathymetry has made the Merrimack a popular natural laboratory for the study of tidally pulsed plumes over recent years

[e.g. Hetland and MacDonald (2008); MacDonald et al. (2007); Cole et al. (2020)]. The aim of this work is to evaluate stratifying and de-stratifying processes in the near and midfield of a tidally pulsed river plume exposed to realistic wind forcing. The objectives of this study are to (1) quantify the net influence of straining, advection, and mixing on tidal plume stratification under realistic winds and (2) evaluate the mechanisms responsible for variability in mixing within the near and midfield plume regions over multiple tidal pulses under differing winds. The Merrimack River plume model is described in detail in section 3.2.1, an overview of the transformation of salinity variance equation used to evaluate stratification and mixing is given in section 3.2.2, and results outlining significant decreases in stratification over the domain following wind events with a northerly component are presented in sections 3.3.1 – 3.3.3. In section 3.3.4 we diagnose the mechanisms which contribute to increased mixing during those wind events, then expand and verify those mechanisms using the entire analysis period in section 3.3.5. A discussion relating this work to others is given in section 3.4, and conclusions are presented last in section 3.5.

## 3.2. Methods

### 3.2.1. Model

Realistic simulations of the Merrimack River estuary-shelf system (Fig. 18) are used in this study. During periods of moderate to high discharge (300 to 700 $m^3/s$), the Merrimack River outflow produces a classic, radially expanding, tidally pulsed river plume. The Merrimack River plume model used in this work has been applied and validated in other works studying tidal plume hydrodynamics and mixing (F. Chen et al., 2009; Hetland & MacDonald, 2008).

Simulations are created using the Regional Ocean Modeling System (ROMS) (Haidvogel et al., 2008; Shchepetkin & McWilliams, 2005), which is a free-surface, hydrostatic, primitive equation ocean model using terrain following sigma coordinates. A curvilinear grid of the north coast of Massachusetts and New Hampshire (Fig. 18b) is utilized which applies realistic bathymetry and coastal morphology to represent the Merrimack River outflow region. The grid encompasses a region 10 km upstream in the

estuary to 20 km offshore with similar 10 and 20 km (from the river mouth) upcoast and downcoast limits, respectively. Grid resolution is 40 m at the mouth and expands to 100 m at the offshore boundaries. 30 vertical sigma layers define depth coordinates everywhere in the domain. The estuary depth is 6 m at the mouth and 300 m wide. Roughly 500 m seaward from the mouth is a slightly shallower sill where freshwater detaches from the bottom and the surface advected river plume forms during sufficient flows.

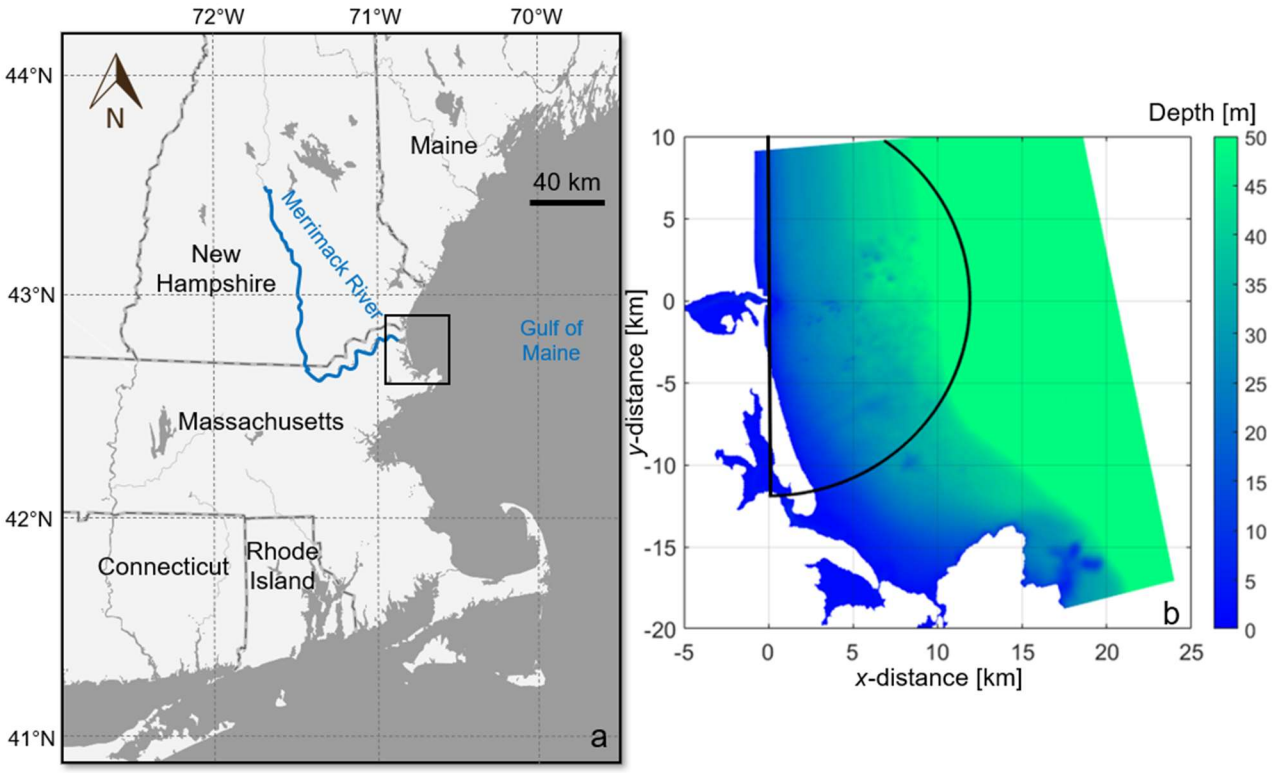


Figure 18: (a) The Merrimack River (blue) shown relative to the Gulf of Maine and surrounding states. (b) Zoom in (black box in panel A) at the mouth of the Merrimack River. Model bathymetry is shown as filled colored contours and the control volume region used in formulating salinity variance terms is outlined in black. The horizontal axis in panel b is the *x*-distance from the river mouth and the vertical is the *y*-distance.

The MPDATA scheme is used to describe horizontal and vertical tracer advection in each simulation (Smolarkiewicz & Grabowski, 1990). A Flather condition is used at each oceanic boundary for 2-D velocities and the free surface (Flather, 1975) while an Orlanski condition is used for 3-D velocities

and salt / temperature tracers (Orlanski, 1976). Vertical mixing is determined using the k-$\varepsilon$ turbulence closure scheme (Umlauf & Burchard, 2003) with Canuto-A stability functions (Canuto et al., 2001). Former work has shown the model to be relatively insensitive to choice of turbulence closure (MacDonald et al., 2007). The momentum equation uses quadratic bottom friction with conservative, parabolic spline reconstruction applied to vertical derivatives in the model.

These ROMS simulations use the hydrostatic assumption, thereby neglecting convective instabilities. It is likely that mixing in the plume front could include significant convective instabilities, and so some error could exist in dissipation of variance or straining estimates there. The front is spatially small relative to the near and midfield plume, though, and has been hypothesized to be unimportant in dictating net plume dynamics (such as mixing) in former work (Cole et al., 2020). For these reasons, the results of this paper would likely be unaffected by a front modeled using a non-hydrostatic formulation.

River discharge is determined from a USGS gage in Lowell, Massachusetts (station #01100000) and is prescribed to the western boundary of the domain as a 0 psu inflow. Wind stresses are applied to the entire domain and are from a NOAA meteorological station on the Isle of Shoals (station IOSN3) in New Hampshire, approximately 25 km northeast of the estuary. Tides are predicted by Xtide, a harmonic tide clock and time predictor software (Flater, 2005), for the 'Plum Island, Merrimack River Entrance, Merrimack River, Massachusetts' station. Xtide uses the same tidal prediction algorithm as NOAA which results in a primarily 1.5 m amplitude (spring/neap average) semidiurnal tide, forced at the ocean boundaries. A 5 cm/s ambient coastal current is applied on the northern boundary, flowing south. This has been considered representative of the Western Maine Coastal Current on this region in former simulations (Cole et al., 2020). The coastal current does not transport any stratification into the domain, as the typical deviations from ambient salinity measured in the current (~2 psu) are well offshore (> 40 km) (Geyer et al., 2004) and considered small relative to contributions from the Merrimack River.

The model is run for the months of April and May in 2019, with April used as the spin-up month and May as the analysis month. Typically, about 1 month is considered sufficient to spin-up the Merrimack estuary, as it is a time dependent salt wedge which reaches realistic estuarine conditions relatively quickly (Cole et al., 2020; Geyer et al., 2008; Ralston, Geyer, Lerczak, et al., 2010). April and May typically produce the largest river discharges of the year in the Merrimack, driven predominantly by locally increased rainfall but also by spring snowmelt from the White Mountains. It is during these months that the most energetic, defined tidal plumes form and so is the ideal timeframe for analysis. Winds are often elevated but variable in direction during these spring months (Fong et al., 1997), making the timeframe even more amiable for this study.

### 3.2.2. Analysis

The analysis utilized in this work stems from the salinity variance equation, first introduced by Burchard & Rennau (2008) and further developed by Li et al. (2018). The relatively simple method links stratification, straining, and mixing in estuarine and coastal systems via deviations in salinity from volume and depth averages while allowing a time and space varying view of each term. As a basis, both vertical and horizontal deviations in salinity must be defined by choosing a control volume representative of the estuary or plume system. Generally, this volume should encompass the most active regions of straining and mixing in the system (Li et al., 2018). Within the control volume, we can state that $S = \langle S \rangle + S'_{tot}$, with $S$ being the salinity at each 3-D coordinate, $\langle S \rangle$ is the volume average of salinity, and $S'_{tot}$ is the anomaly from the total volume average at each point. Decomposing salinity in the vertical direction gives a similar formulation: $S = \bar{S} + S'_v$, where $\bar{S}$ is the depth average of salinity and $S'_v$ is the deviation from the vertical average. Using the total and vertical deviations, we can calculate the corresponding horizontal deviation: $S'_h = S'_{tot} - S'_v$. By squaring each salinity deviation, we can represent the vertical salinity variance, $(S'_v)^2 = (S - \bar{S})^2$, the horizontal variance, $(S'_h)^2 = (\bar{S} - \langle S \rangle)^2$, and the total variance, $(S'_{tot})^2 = (S - \langle S \rangle)^2$, at each 3-D coordinate (with the exception of $(S'_h)^2$, which does not vary with depth). Variance in this context is used as a metric for stratification, i.e., vertical salinity variance

physically represents vertical stratification of salinity and so these terms are used synonymously. Depth integrating each variance term gives the relationship:

$$\int (S'_{tot})^2 dz = \int (S'_h)^2 dz + \int (S'_v)^2 dz \qquad (18)$$

which then allows:

$$\iiint (S'_{tot})^2 dx\, dy\, dz = \iiint (S'_h)^2 dx\, dy\, dz + \iiint (S'_v)^2 dx\, dy\, dz \quad (19)$$

where the left-hand side of Equation 19 represents the total variance in the control volume, while the right-hand terms represent the net horizontal and vertical variances (from left to right, respectively) in the volume.

For volume integrated quantities, a semi-circle with a 12 km radius originating at the river mouth is used to define the tidal plume control volume (Fig. 18b). This volume includes the nearfield and midfield plume for all discharge events during the study period, and omits the estuary, thereby enclosing the most active regions of plume mixing during a tidal pulse. Generally, any portion of the plume which exceeds the 12 km radius is downcoast of the control region and is transitioning to the far-field plume, which mixes less intensely and evolves beyond a tidal time scale. Further, instantaneous wind effects have been considered negligible in their influence on Merrimack River plume dynamics beyond 12 km (Kakoulaki et al., 2014). By applying that region to Equation 19, we can determine bulk variance quantities over the control volume for the entire study period.

An important concept in the approached outlined by Li et al. (2018) is the ability for horizontal variance to be converted to vertical variance through straining. The crux of their solution is the derivation of the conservation of vertical salinity variance which allows for this transformation of (depth integrated) variance (repeated from chapter 1):

$$\frac{\partial \int (S'_v)^2 dz}{\partial t} + \nabla_h \cdot \int \boldsymbol{u_h} (S'_v)^2 dz = \int -2\boldsymbol{u'_v} S'_v \cdot \nabla \bar{S}\, dz - \int 2K_z \left(\frac{\partial S}{\partial z}\right)^2 dz \qquad (20)$$

In Equation 20, $\nabla_h$ is the horizontal gradient operator, $\boldsymbol{u_h}$ is the horizontal velocity vector, $\boldsymbol{u_v'}$ is the deviation of the 3-D velocity vector from a depth average ($\boldsymbol{u} = \overline{\boldsymbol{u}} + \boldsymbol{u_v'}$), and $K_z$ is the vertical eddy diffusivity, determined from the model turbulence closure. The terms in Equation 20 represent the net time rate of change of salinity variance, advection, straining, and dissipation / mixing (from left to right, respectively). Essentially, vertical salinity variance can be input to the system via advection (plume pulses from estuary) or created internally through straining (horizontal salinity gradients strain and create vertical salinity gradients). Vertical variance is destroyed by turbulent dissipation or transported out of the control volume by advection.

Conceptualizing what stratification (vertical variance) means in this work is important, as there are nuances in how many interpret stratification. In this context, $\int (S_v')^2 dz$ scales with the potential for vertical mixing to occur in the water column and does *not* quantify the strength of a density gradient. This means vertical variance and the terms comprising Equation 3 may vary according to water column depth, even if the density gradient of a stratified layer in the water column has an unchanged density gradient. This depth effect was found to be inconsequential to this analysis, and is described in more detail in Appendix D.

### 3.3. Results

#### 3.3.1. Environmental Conditions and Salinity Variance Variability

Typical spring-neap variability in sea surface elevation (Fig. 19a) coupled with a steadily decreasing but significant river discharge (1000 $m^3/s$ dropping to 300 $m^3/s$ in Fig. 19b) created defined, energetic tidal plumes for the entire month of May 2019. Winds over the study period were particularly variable in magnitude and direction (Fig. 19c), allowing an analysis which captured a wide spectrum of realistic wind forcing. Relatively larger wind events ($\tau_w$ ~ 0.1 to 0.2 Pa) were numerous and typically dominated by the north-south component, with a roughly even split between north or south dominance for those events. Enhanced east or west directed wind events were less prevalent. Typically, larger wind events (magnitude > 0.1 Pa) lasted 24 to 48 hours, while moderate events (~0.5 Pa) lasted between 12 and

24 hours. Often rapid transitions (< 12 hours between directional shifts) separated events. Light wind conditions (magnitude < 0.05 pa) occurred but were less frequent than the moderate conditions.

Fig. 19d shows how the volume integrated variance terms generally scale with discharge. That is, the largest variances in all components occur during the first 10 days of May, when river discharge exceeds 500 $m^3/s$. Vertical variance accounted for most of the total variance at this time and varies

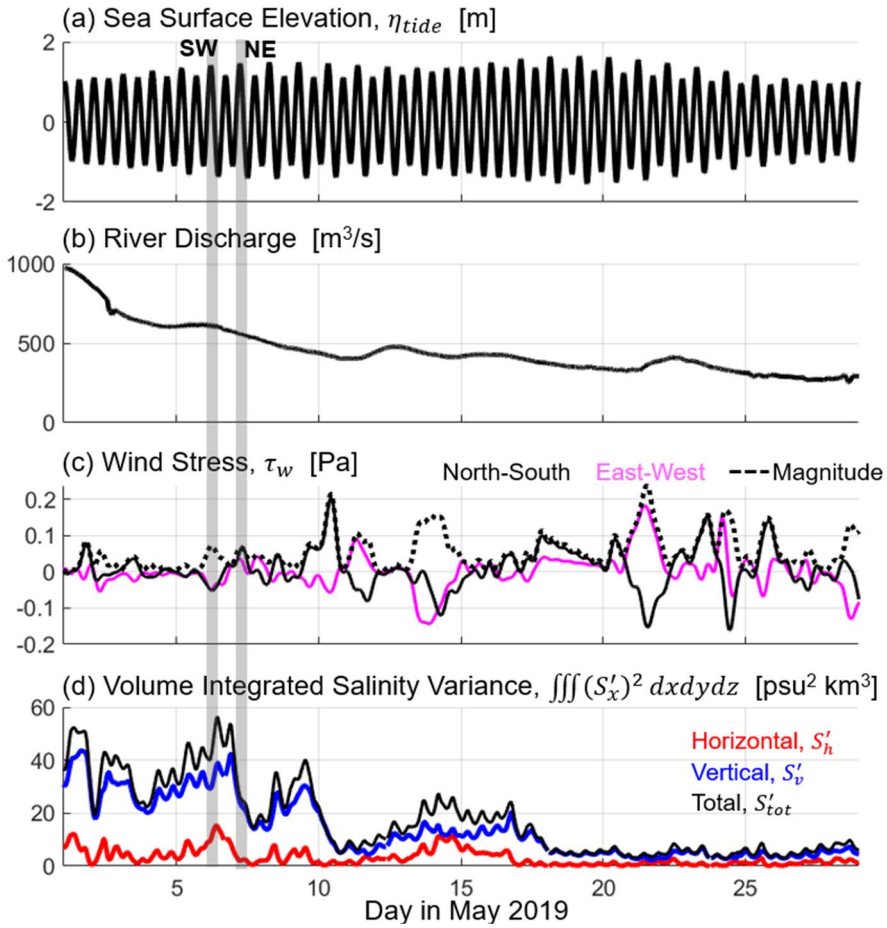


Figure 19: (a) Sea surface elevation, (b) river discharge, and (c) wind stresses in oceanographic convention (east-west as magenta, north-south as solid black, and magnitude as dotted black) at the mouth of the Merrimack River for the month of May 2019. (d) Control volume integrated vertical (blue), horizontal (red), and total (black) salinity variance is also shown for the month. Wind stress was low pass filtered for 6 hours to smooth for this visual. The *x*-axis is the day of May 2019. The times over which plumes SW and NE from the analysis occur are shaded with gray boxes.

between 20 and 40 $psu^2$ $km^3$ while horizontal was much less at 5 to 10 $psu^2$ $km^3$ (Fig. 19d). Both vertical and horizontal variance are markedly smaller (< 10 $psu^2$ $km^3$) after day 10, when discharge drops below 500 $m^3/s$. Similarly, tidal variability in all variance terms is more evident for the larger discharges (> 500 $m^3/s$) over the study period, with 12-hour ebb-flood oscillations in signal typically between 5 and 8 $psu^2$ $km^3$ (before day 10, Fig. 19d). For the smaller discharges, the intratidal differences are less than half that (2 to 4 $psu^2$ $km^3$ after day 10, Fig. 19d).

Although discharge likely plays an important role in determining the general magnitude of variance over the study period, it is evident wind direction, particularly in the along-shore direction, mainly dictates whether variance increases or decreases. At the Merrimack River mouth, winds in the north-south direction are aligned alongshore, whereas east-west is cross-shore. The more noted reductions in total, vertical, and horizontal variance occur at roughly days 2, 3, 7, 10, and 17 and always follow, or coincide with, an alongshore wind stress directed north (in oceanographic convention, Fig. 19c, d, hereby referred to as northward). Interestingly, the magnitude of the northward wind is seemingly unimportant in its ability to reduce variance, as both relatively larger (0.2 Pa, day 10) and moderate (0.08 Pa, day 7) northward wind events can reduce vertical variance by similar amounts (~25 $psu^2$ $km^3$ for each). The disconnect between wind magnitude and vertical variance suggests direct wind stress mixing is not of major importance to the destruction of stratification (discussed further in section 3.3.3). Further, horizontal variance typically begins decreasing when vertical variance is maximizing during northward wind events (i.e., day 7), suggesting straining enhances vertical variance to some extent under northward winds. Vertical variance often continues to decrease for up to 12 hours following northward wind events, suggesting a plume-shelf condition is modified which is not directly wind-driven (see days 1, 3, and 10, Fig. 19). Further, large wind events in other directions (such as the strong southward wind event prior to day 15 in Fig. 19c) have minimal influence on vertical variance (Fig. 19d). During periods of gradually increasing variance (e.g., days 4 to 6 and 12 to 16) winds are either near zero or have a south directed

alongshore component (Fig. 19c, d, hereby called southward). For the entire study period, the cross-shore wind stress has little effect on variance.

The Merrimack River plume has been found to be transported and sensitive to the alongshore component to wind, regardless if larger scale Ekman circulation patterns are or are not established, due to the plume's smaller spatial scales (Kakoulaki et al., 2014). The wind patterns identified in Fig. 19 likely advect vertical variance in and out of the control volume in some accordance with the findings of Kakoulaki et al. (2014). To confirm the role of wind on advecting plume water, and to identify the more ambiguous roles of dissipation and straining in controlling stratification under varying wind, we next decompose the spatial variability in dynamics between tidal plumes exposed to differing moderate wind conditions.

### 3.3.2. Spatial Variability: Stratification

Two tidal pulses occurring roughly 24 hours apart from each other were analyzed to identify variability in plume dynamics between a wind blowing northeastward (hereby called plume "NE") and one blowing opposite, southwestward (called plume "SW", both labeled in Fig. 19). NE and SW were chosen as they occur during similar tide and discharge conditions, have winds in opposing directions but same in magnitude, and are only 24 hours apart, allowing for relatively easy visualization of the transition from one plume to the next. Plume NE generally advects offshore, differing from the prototypical downcoast turning, coastal-trapped plume, which occur for most other winds conditions (like SW, discussed below). Analyzing plumes NE and SW therefore allows a relatively simple comparison between two dynamically different scenarios which occur within a day of each other.

During southwest winds (Fig. 20a, b) the Merrimack River plume spreads out from the estuary and turns to the right. Surface currents are directed primarily to the right of the wind (toward west / northwest) and decrease in magnitude nearer to shore (Fig. 20a), likely from an opposing barotropic pressure gradient created by both alongshore (downwelling favorable) and cross shore (onshore) wind-

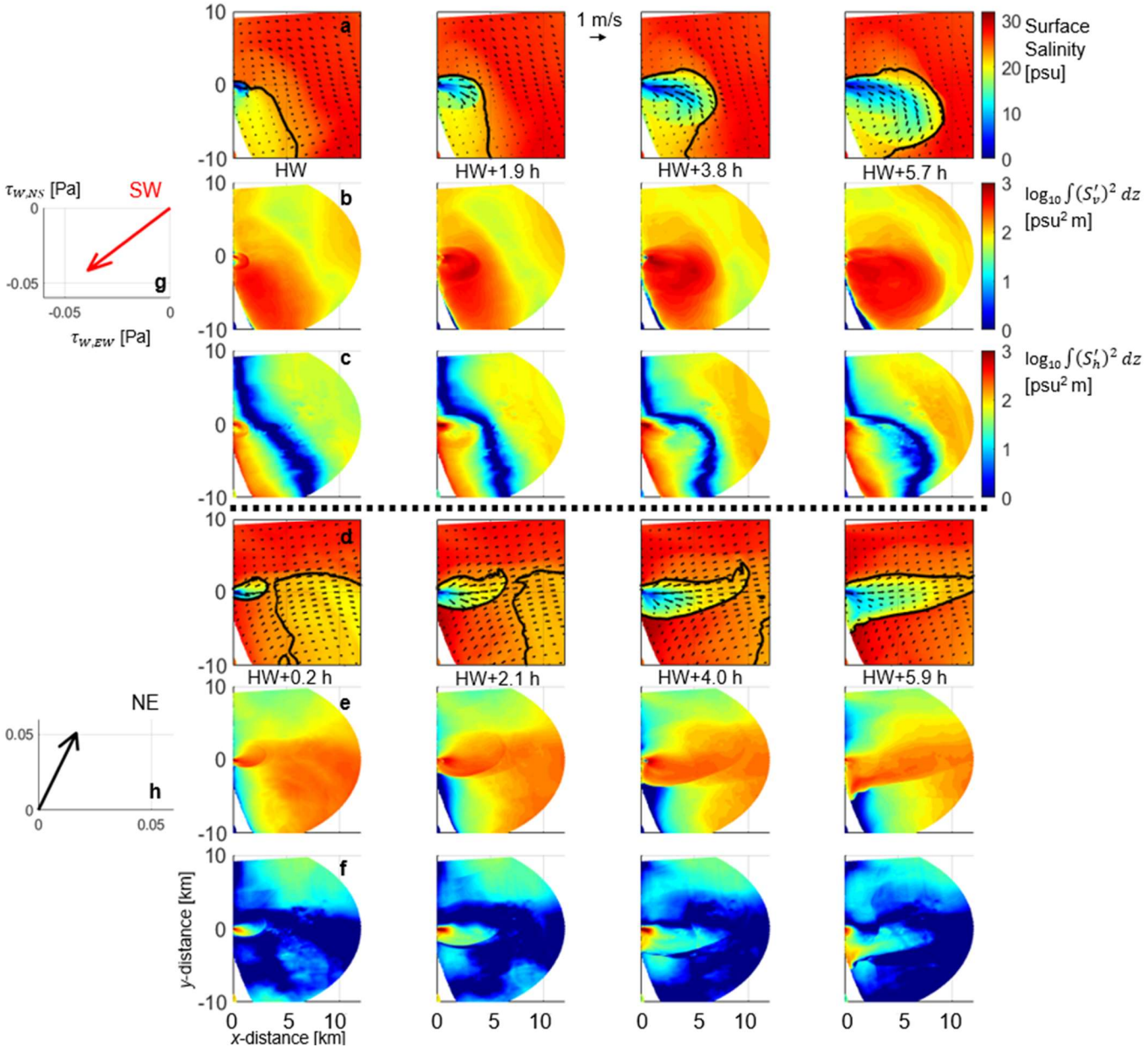


Figure 20: Snapshots of plume SW (a - c) and NE (d - f) over a tidal pulse. Surface salinity contours are shown for each case with the 23 psu isohaline given as a solid line and surface current vectors as black arrows (a, d) as well as the depth integrated vertical salinity variance (b, e) and horizonal salinity variance (c, f) on a $\log_{10}$ scale. Each plume is depicted over a roughly 6-hour tidal pulse, with times in reference to high water (HW) shown (a, d). Mean wind stresses (with north-south [NS] and east-west [EW] components) over each plume are given as vectors (g, h). Horizontal axes are the *x*-distance and vertical are *y*-distance.

driven sea level setup (Lentz & Fewings, 2012). The relatively weaker surface currents nearshore ($x$ < 5 km) allow the plume to spread prototypically outward from the river mouth, but landward surface velocities in deeper water (x > 5 km) slow offshore propagation of the plume and Earth's rotation turns the plume downcoast (Fig. 20e and Fig. 20a, respectively) in the direction of Kelvin wave propagation (i.e., anticyclonic). Enhanced vertical salinity variance over the shelf [$\log_{10}(\int (S_v')^2\, dz \sim 2.5$ psu$^2$ m) in Fig. 20b] indicates ambient coastal waters are stratified from former plumes not mixing or advecting out of the domain completely during the light wind conditions which occurred prior (Fig. 19), allowing residual stratification to remain over the shelf. The remaining vertical variance then accumulates nearshore due to the landward surface currents. The new plume which pulses over the shelf adds to that stratification ($\log_{10} \int (S_v')^2\, dz \sim 3$ psu$^2$ m in Fig. 20b) as mixing again does not destroy all variance and surface flow promotes shoreward, anticyclonic plume advection, keeping the stratified water column trapped in the control volume. Horizontal variance is maximized at the river mouth where the plume begins spreading seaward [$\log_{10}(\int (S_h')^2\, dz \sim 3$ psu$^2$ m) in Fig. 20c] but is also enhanced downcoast of the mouth [$\log_{10}(\int (S_h')^2\, dz \sim 2 - 2.5$ psu$^2$ m), Fig. 20c] in the region of shore-trapped vertical variance. Horizontal variance remains elevated and does not exhibit significant variability over the tidal pulse.

The role of advection in steering plume and ambient shelf water clearly differs during the opposing northeast wind case as the plume advects mainly offshore (Fig. 20d). Surface currents are mainly directed with the wind (toward northeast) or to the right of it (east) and are similar in magnitude both nearshore (x < 5 km) and in deeper water. Unlike plume SW, the offshore and upwelling favorable wind components likely prevent an opposing barotropic flow (Fig. 20d). The plume advects offshore more readily, exhibiting a sensitivity to the shelf's surface current wind response (Fig. 20h) [similar to findings in Kakoulaki et al. (2014)]. Consequently, residual vertical variance over the shelf from former tidal pulses (the light then SW winds) is pushed offshore with the new plume (Fig. 20e). This advection of vertical variance out of the control volume results in a nearly homogenous water column over the inner shelf in the vicinity of the nearfield river plume (< 5 km from shore, $\log_{10} \int (S_v')^2\, dz \sim 0.5$ psu$^2$ m in Fig.

20e). During plume NE, horizontal variance is again maximized at the river mouth ($\log_{10} \int (S_v')^2 \, dz \sim 3$ psu$^2$ m in Fig. 20e) but is notably diminished in the remainder of the control volume relative to SW, suggesting straining may be more active in converting horizontal variance to vertical under northward winds.

Former work in the Merrimack found the plume to generally follow the direction of wind, regardless of duration, due to the short time and spatial scales over which it exists on the shelf (Kakoulaki et al., 2014), and supports the advection trends outlined here. Here, we see a similar sensitivity of the ambient stratification to wind direction. Although we hypothesize straining is modulated by wind direction, it remains unclear, as is the wind effect on the mixing of variance. We next analyze the spatial structure of straining and dissipation for plumes SW and NE to identify where each term is most dominant spatially and what that implies in the context of plume dynamics.

### 3.3.3. Spatial Variability: Mixing and Straining

For plume SW, the nearfield region (< 5 km from mouth) dominates straining for the entire tidal pulse ($\int -2u_v'S_v' \cdot \nabla \bar{S} \, dz >$ 0.1 psu$^2$ m s$^{-1}$, Fig. 21a) as the estuarine outflow shoals, thins, and spreads over saltier receiving waters, converting horizontal variance to vertical. The frontal region can be identified in each snapshot as the band of relatively intense negative straining ($\int -2u_v'S_v' \cdot \nabla \bar{S} \, dz =$ -0.01 to -0.1 psu$^2$ m s$^{-1}$, Fig. 21a) which propagates outward from the river mouth over the tidal pulse. Negative straining occurs near the plume front because horizontal variance is added to the shelf as the plume front passes. Between the front and nearfield plume, straining is generally positive but smaller in magnitude (often by an order of magnitude or more) than the nearfield ($\int -2u_v'S_v' \cdot \nabla \bar{S} \, dz \sim$ 0.01 psu$^2$ m s$^{-1}$, Fig. 21a). Dissipation of vertical variance in the nearfield dominates relative to the remainder of the plume footprint (< 5 km from mouth, $\int -2u_v'S_v' \cdot \nabla \bar{S} \, dz >$ 0.1 psu$^2$ m s$^{-1}$, Fig. 21b). Dissipation decreases significantly beyond the nearfield and is at least an order of magnitude less in most of the plume interior (> 5 km from mouth, $\int -2u_v'S_v' \cdot \nabla \bar{S} \, dz \sim$ 0.01 psu$^2$ m s$^{-1}$, Fig. 21b). For plume NE, patterns in straining and dissipation are largely the same, i.e., the nearfield dominates regardless of wind direction (Fig. 21c,

d). For both plumes SW and NE dissipation is largely near 0 outside the plume foot print, suggesting that direct surface wind mixing is likely of secondary importance to stratified shear mixing during moderate wind events, as has been hypothesized in former work (Horner-Devine et al., 2015).

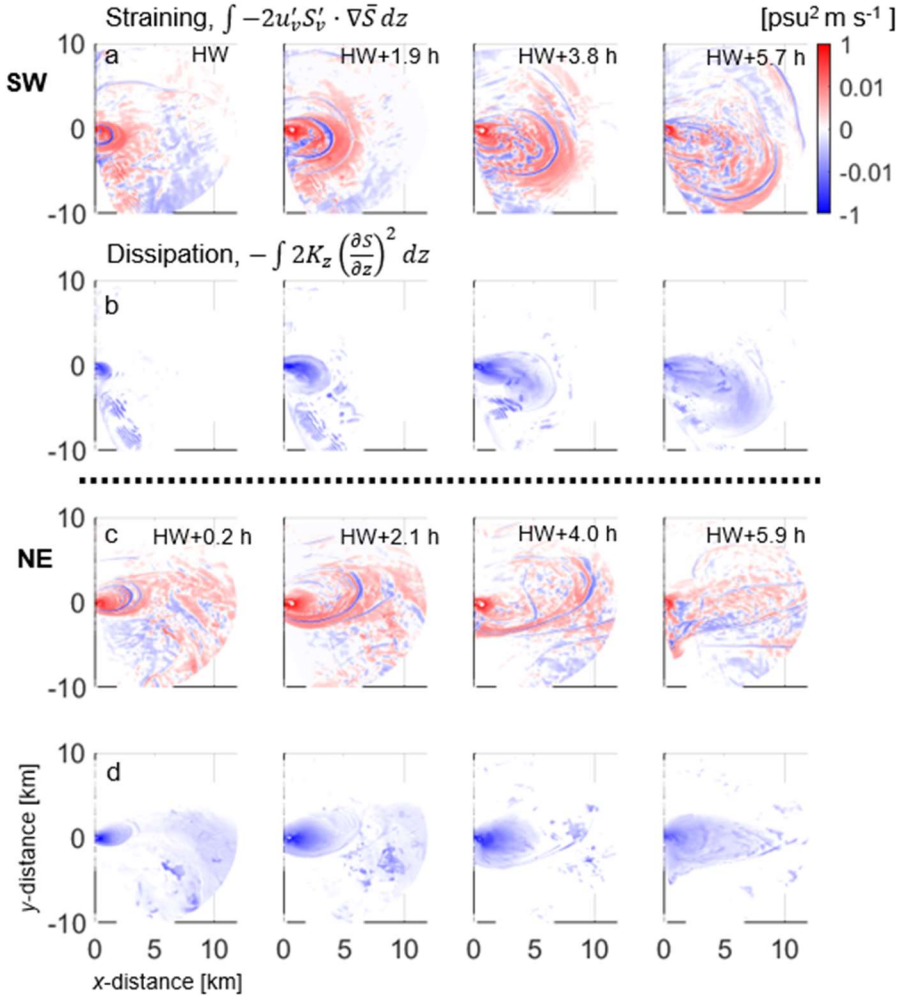


Figure 21: Plan view snapshots of straining (a, c) and dissipation of vertical variance (b, d) on a $\log_{10}$ scale for plumes SW (a, b) and NE (c, d). Time steps match those from Fig. 20. Horizonal axes are the *x*-distance and vertical are *y*-distance.

Straining and dissipation dominate in the nearfield plume, regardless of wind, but it is difficult to identify variability in the terms between the river mouth and front. To better quantify spatial variability in the terms, a salinity coordinate approach was utilized (Hetland, 2005). Salinity coordinates are useful as they translate with the plume as it progresses over an ebb pulse. Differences in dynamics between plume

regions can be isolated and identified more easily when comparing regions of similar salinity versus static locations. The coordinates here are based on surface salinities, as they are broadly representative of plume-layer salinities and easily compared to Fig. 20. In general, there are larger spatial regions of the 5 to 23 psu surface salinity class in plume SW relative to plume NE, which persist over the entire tidal pulse (Fig. 22). A rough comparison to Fig. 20a, c indicates that the 0 to 10 psu class roughly corresponds to the nearfield plume (minimal rotation downcoast), while 10 to 23 psu matches the midfield plume (remainder of plume area). Some ambient shelf water from residual stratification falls in the 20 – 23 psu range and thereby skews isohaline areas up in that range. Size discrepancies between SW and NE below 20 – 23 psu, in the near and midfield plume, are not skewed by shelf salinity, and indicate variability in straining and dissipation exists in those regions.

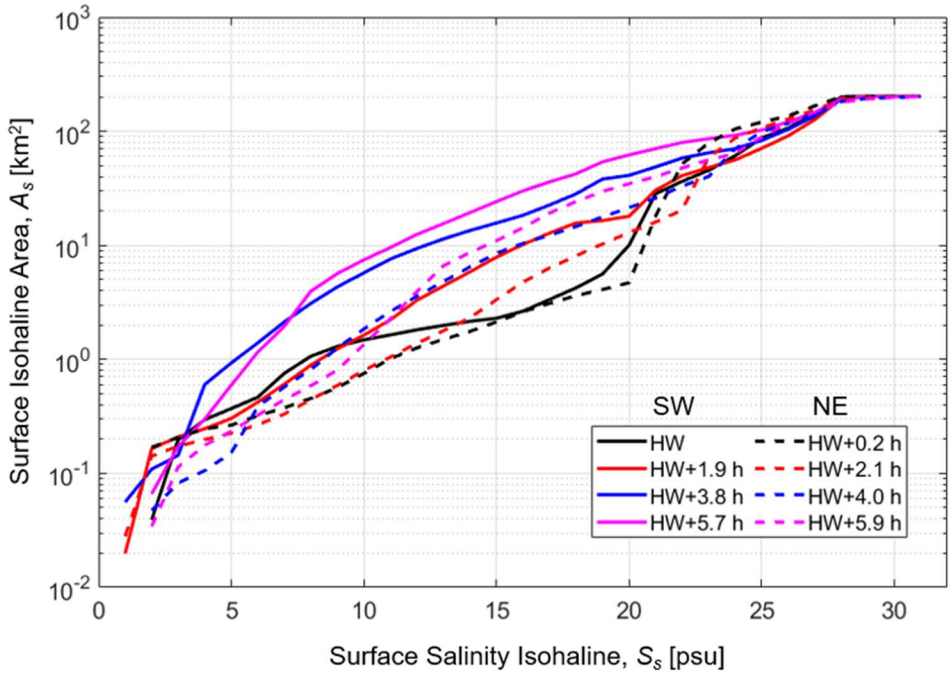


Figure 22: Area ($y$-axis) enclosed by each surface salinity contour ($x$-axis) at four similar times (relative to high water [HW]) during plume SW (solid lines) and plume NE (dashed lines). Time steps match those from Figures 20 and 21.

The intensity of vertical variance dissipation, along with straining, was quantified following salinity coordinates to determine variability. Here we consider intensity to be the volume integral of either

dissipation or straining (magnitude), divided by the area over which it acts: $\frac{\iiint x\, dV_s}{A_s}$, with $x$ representing absolute values of either straining ($|2u_v'S_v' \cdot \nabla\bar{S}|$) or dissipation $\left(\left|2K_z\left(\frac{\partial S}{\partial z}\right)^2\right|\right)$, and $V_s$ being the volume beneath the area, $A_s$, enclosed by isohaline, $s$ (area from Fig. 22). A larger intensity in either term indicates more dissipation and/or straining per unit area. For all plume regions enclosed by the ~23 psu salinity class or less, both straining and dissipation are generally more intense in plume NE (Fig. 23). Using the 10 psu isohaline as example, during mid-pulse (~ 4 hours after high water, blue lines in Fig. 23), dissipation intensity is nearly 1 order of magnitude larger in the plume exposed to NE winds than SW (Fig. 23). Differences between each plume are much less noted beyond the 23 psu isohaline, confirming the lessening importance of dissipation and straining processes moving away from the nearfield into the

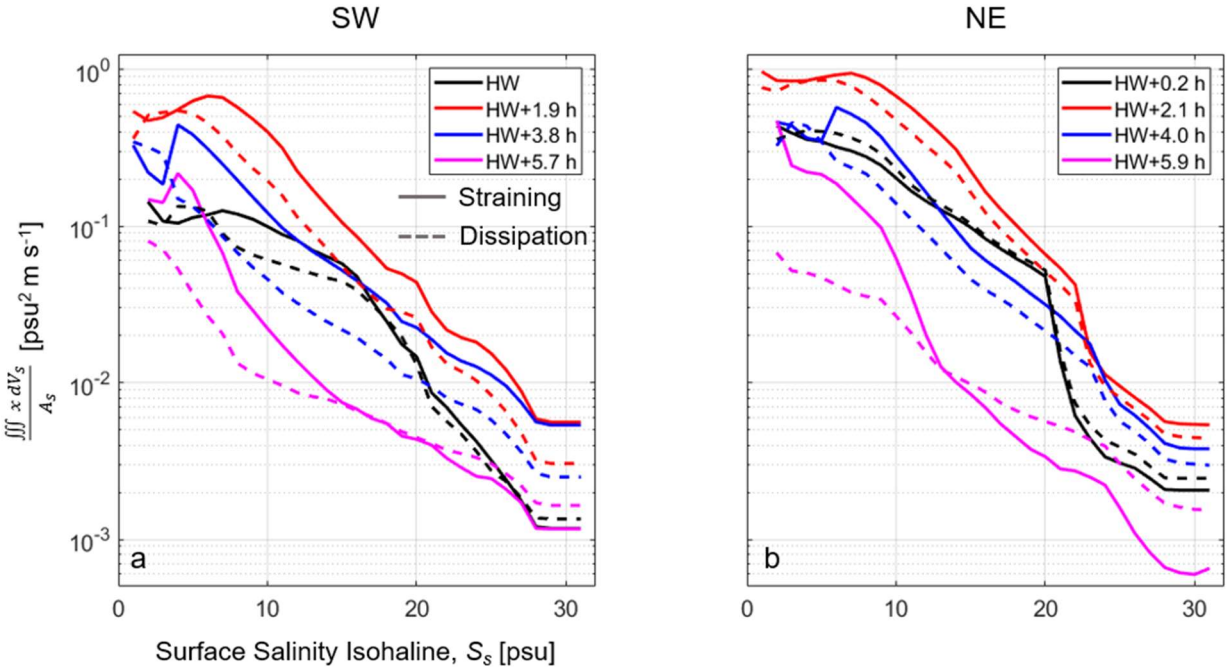


Figure 23: Intensity ($y$-axis) of straining ($x = |2u_v'S_v' \cdot \nabla\bar{S}|$) and dissipation of vertical variance $\left(x = \left|2K_z\left(\frac{\partial S}{\partial z}\right)^2\right|\right)$ for a given region bounded by each surface isohaline ($x$-axis) at similar times (relative to high water [HW]) for plume SW (a) and plume NE (b). Intensity is determined by taking the volume integral of $x$ over the region $A_s$, then dividing by $A_s$. Straining is shown as solid lines while dissipation is dashed. Time steps match those from Figures 20, 21, and 22.

midfield and ambient shelf (Fig. 23). Collectively, the relative area of the near and midfield plume for plume NE is less than that of SW but dissipation and straining are significantly more important.

### 3.3.4. Mixing and Straining Mechanisms in the Nearfield Plume

In comparing two tidal plumes created by similar river discharges, we have shown that moderate wind stresses opposing the direction of Kelvin wave propagation can alter the dynamics of the Merrimack River plume-shelf system, notably by advecting vertical variance offshore, thereby homogenizing the water column nearshore, and increasing straining and dissipation of vertical variance in the near to midfield river plume. We now investigate the physical mechanisms which lead to dissipation and straining to connect the terms to wind direction, the ambient shelf condition, and the strength of the nearfield plume density gradient (which is not directly quantified via $(S'_v)^2$).

Time and depth varying salinity and currents at a nearfield plume location ($x$ = 1 km, $y$ = -1 km from the river mouth) portray changes in hydrography as winds transition from SW to NE (Fig. 24). When the wind change occurs (roughly day 6.7 in Fig. 24) successive plumes become thinner than SW (see dashed line approach surface, Fig. 24b). Although thinner, surface waters in NE are just as fresh as SW (~ 10 psu, Fig. 24a) and offshore advection of variance creates a saltier ambient shelf condition beneath NE (30 psu isohaline moves toward surface over time, Fig. 24b), creating a stronger density gradient at the plume base. Further, winds during plume NE enhance ebb current velocities within the thinned plume ($\sqrt{u^2 + v^2}$ increases from 0.5 to 0.8 m/s, Fig. 24b), subsequently increasing shear in the nearfield of NE relative to SW. Increased plume velocities are likely a result of increased offshore transport in the plume due to wind augmenting ebb tide and discharge momentum. A recent study in the Fraser River plume supports this: winds opposing Kelvin wave propagation created a faster moving, offshore advected plume, whereas winds in the opposite direction created a “typical”, slower, onshore rotating plume (Kastner et al., 2018). These wind-induced increases in shear likely create the enhanced straining observed in the near and midfield plume (as quantified in Fig. 23b) which thin the plume, as

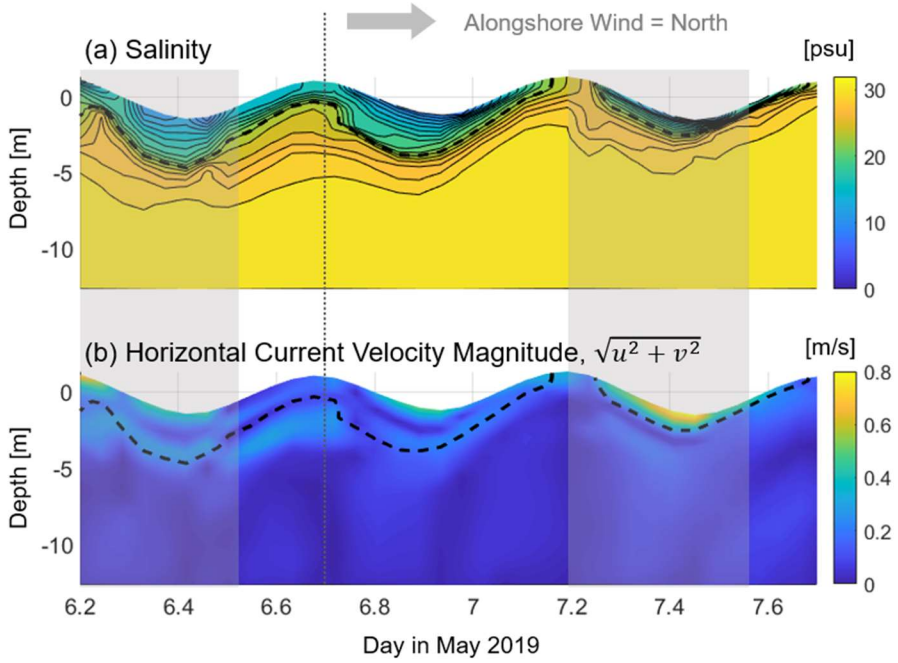


Figure 24: (a) Salinity and (b) horizontal current velocity magnitude at a nearfield plume location [$x$ = 1 km, $y$ = -1 km] during days 6 and 7 of May 2019 ($x$-axis). Plumes SW and NE are outlined with gray boxes and labeled. The 23 psu isohaline is marked with a dashed line. Contours in (a) mark every other isohaline between 32 and 0 psu. The point where winds shift towards the north is marked with a dotted gray line and labeled. The $y$-axes are water depth.

described here. Wind enhanced straining has been observed similarly in estuaries, where winds blowing in the same direction as surface currents increase shear in the water column (Scully et al., 2005).

We next link the salinity variance method to classic turbulence theory at the same nearfield plume location ($x$ = 1 km, $y$ = -1 km) to identify how wind straining of plume NE over a saltier shelf can modulate mixing. Shear production, $P = -\overline{u'w'}\left(\frac{\partial u}{\partial z}\right) - \overline{v'w'}\left(\frac{\partial v}{\partial z}\right)$ (where $\overline{u'w'}$ and $\overline{v'w'}$ are the Reynold's stresses in the $x$ and $y$ directions, respectively), quantifies turbulent energy created through velocity shear in the vertical, and is most intense in the wind-strained NE plume ($10^{-4}$ $m^2s^{-3}$, Fig. 25a) relative to SW ($10^{-5.5}$ $m^2s^{-3}$, Fig. 25a). The elevated $P$ acts directly on the stronger density gradient at the base of plume NE, whereas it is confined within the plume layer of SW (Fig. 25a). Shear production is

then compared to the turbulent buoyancy flux, $B = -\frac{g}{\rho_0} K_z \frac{\partial \rho}{\partial z}$ (where $\rho_0$ is a reference density and $\frac{\partial \rho}{\partial z}$ is the vertical gradient in density), to identify how elevated *P* acting on a more intense density gradient at the plume base translates to mixing. Like *P*, buoyancy flux at the plume base is larger in magnitude during NE ($10^{-5}$ $m^2s^{-3}$, Fig. 25c) relative to SW ($10^{-6.5}$ $m^2s^{-3}$, Fig. 25c). The depth averaged *B* is similar for both plumes ($10^{-5.5}$ $m^2s^{-3}$, Fig. 25d), indicating mixing in the plume layer becomes more concentrated, or

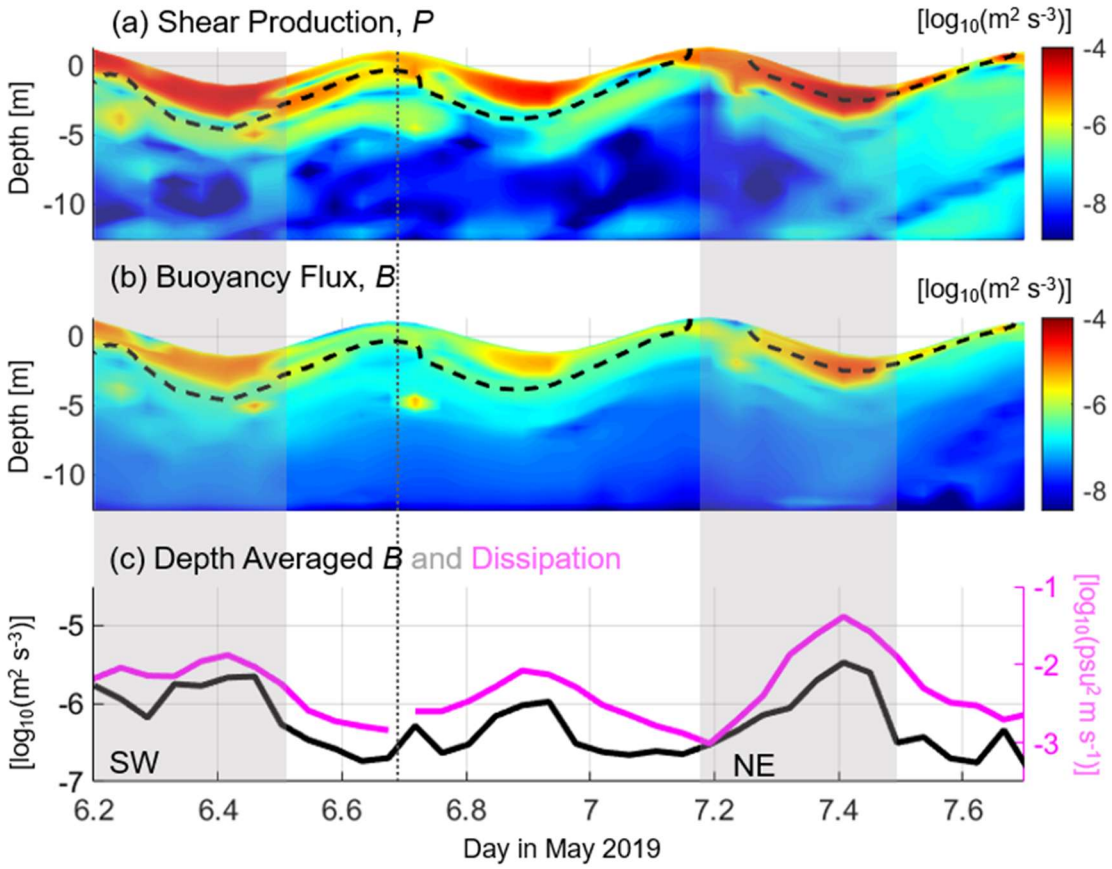


Figure 25: Filled contours of (a) turbulent shear production, *P*, and (b) turbulent buoyancy flux, *B*, at a nearfield plume location [*x* = 1 km, *y* = -1 km] during days 6 and 7 of May 2019 (*x*-axis). Line plots show (c) depth averaged *B* (black) and dissipation, $\int 2K_z \left(\frac{\partial S}{\partial z}\right)^2 dz$ (magenta). All data is sub-sampled to hourly resolution. Color bars (a, b) and y-axes (c) are on a $\log_{10}$ scale. Plumes SW and NE are outlined with gray boxes and labeled. The 23 psu isohaline is marked with a dashed line. The point where winds shift towards the north is marked with a dotted gray line. The *y*-axes in (a) and (b) are water depth.

intense, at the interface of the thinned NE plume. The dissipation of variance term, being sensitive to both $K_z$ (increases with $P$) and $\frac{\partial S}{\partial z}$ (increases from advection of stratification offshore) maximizes during NE (Fig. 25d). In essence, Fig. 25 outlines how larger shear production occurs due to wind straining and acts on a larger density gradient at the plume base (created from wind straining thinning the plume and advection setting up saltier water beneath) subsequently allowing the local dissipation of vertical variance to maximize.

### 3.3.5. Major Trends and Relative Importance of Mixing to Straining

We now expand these findings to the remainder of the tidal plumes in the study period and identify exceptional cases. The terms in the conservation of vertical variance equation (Equation 20) were evaluated and averaged over the control volume for the entire month (Fig. 26). As established in Fig. 21, the nearfield and midfield plume dominate overall dissipation and straining in the control volume, so general variability shown in Fig. 26 can be considered controlled by those plume regions with negligible influence from the ambient shelf. Straining is largely balanced by dissipation, which is opposite in sign but often smaller in amplitude, particularly for larger river discharges in the beginning of the month (Fig. 26a). The excess variance which is not destroyed by dissipation is generally accounted for via advection (Fig. 26a). At subtidal scales (30 h. low-pass filtered terms, Fig. 26b) advection and the net time rate of change of vertical variance are nearly identical, and so similar to Li et al. (2018) we regard them as one in the same. Negative advection therefore indicates transport of excess stratification out of the domain, while positive indicates an accumulation of stratification within the domain. Residual stratification remaining in the domain and that which is immediately advected out will ultimately contribute to the far-field plume and persist at time scales longer than tidal. The northward wind events identified as strong de-stratifying events (e.g., days 2, 3, 7, 10, 17, etc. in Fig. 19c, d) nearly always result in transport of stratification out of the domain (negative advection, Fig. 26) due to offshore and/or upcoast (opposing Kelvin wave) surface currents which counter the anticyclonic tendency of the plume. Most plumes exposed to northward winds are also generally accompanied by enhanced straining and dissipation of variance (Fig.

26), confirming analysis in prior sections. Interestingly, the greatest dissipation enhancement from northward winds tend to also occur on the tide immediately following the negative advection (northward wind) event (Fig. 26a). Maximum straining does not lag advection, indicating the northward winds have an immediate effect on advection and straining, as expected, but maximum dissipations seem more prone to occur after the ambient shelf is cleared of residual stratification following a wind event.

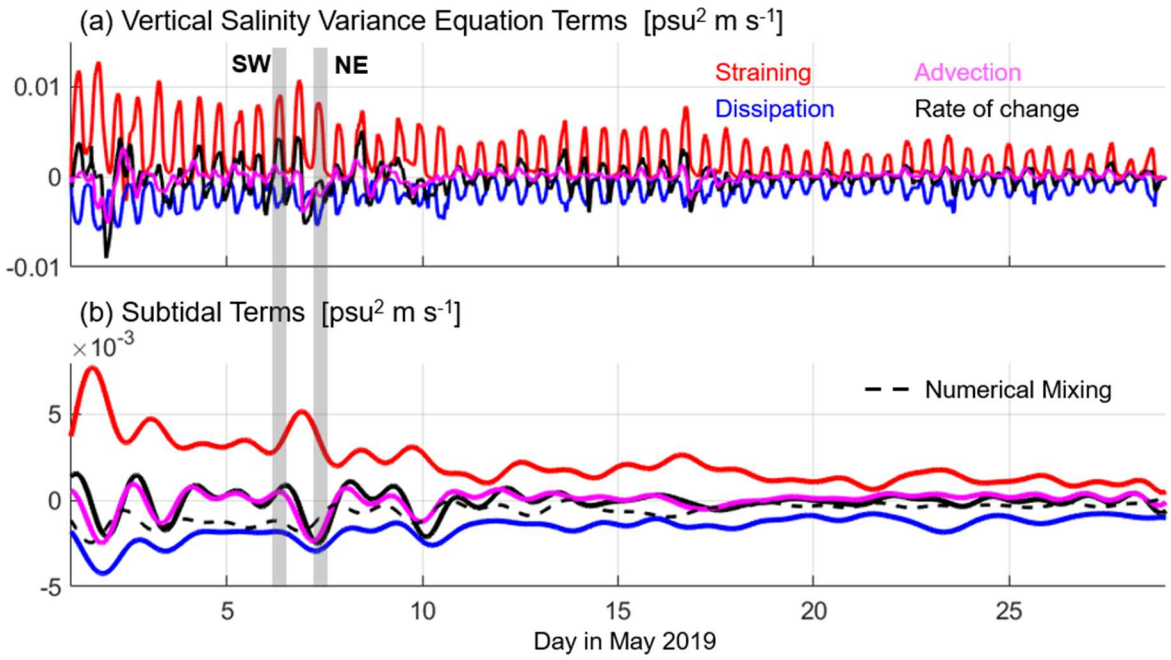


Figure 26: (a) Area averaged vertically integrated salinity variance equation terms (straining in red, dissipation of variance in blue, advection in magenta, and net rate of change of vertical variance in black) and (b) the 30-hour low-pass filtered (subtidal) version of panel a with numerical mixing added (dashed black). The *x*-axis is the day of May 2019. The times over which plumes SW and NE from the analysis occur are shaded with gray boxes.

It has been determined that northward winds enhance negative advection, plume straining, and dissipation of variance, while dissipation can remain elevated following north wind events. It remains unclear if dissipation is more effective at eliminating vertical variance created by straining during or after the north wind events relative to typical conditions. We quantified the ratio of dissipation to straining for every tidal plume in the month of May 2019 to investigate. We found the plume dissipation – straining

ratio is most connected to the initial ambient shelf stratification prior to a tidal pulse (high water) which in turn is linked to the average wind from the previous 12 hours. The initial shelf stratification, quantified as a volume integral of vertical variance ($\iiint (S_v')^2\, dxdydz$ ) outside the estuary prior to each plume in May 2019, is smallest typically following wind events with a northward component and negative net advection when stratification is pushed offshore and out of the control volume ($y$-axis, Fig. 27). A few notable southward wind events also result in diminished variance on the shelf, but these events are the minority relative to winds aimed north (Fig. 27). The tidal plumes which develop after the northward, negative advection events then tend to have the largest ratio of dissipation to straining, with both terms volume and

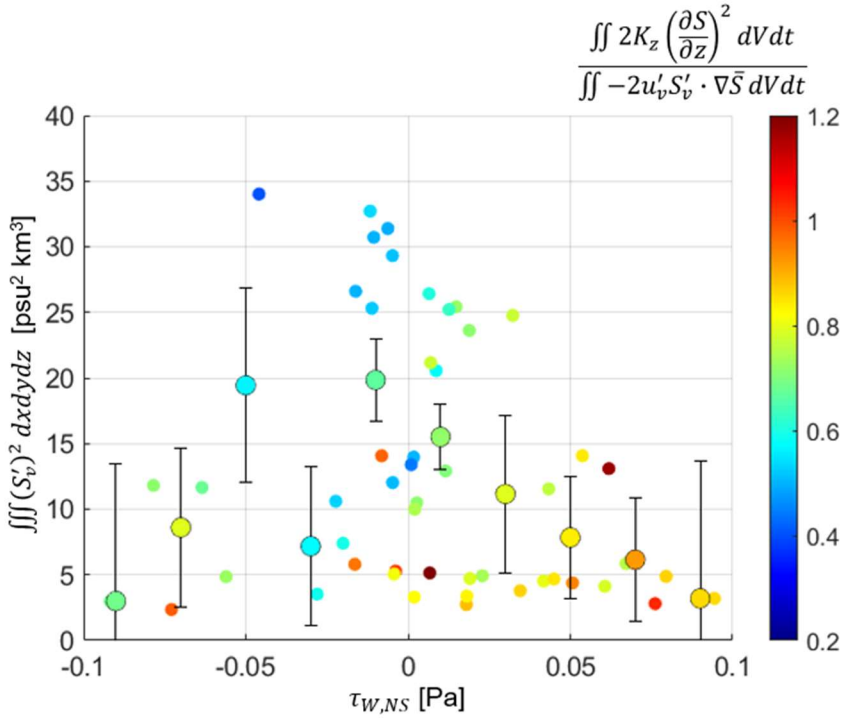


Figure 27: Pre-ebb pulse volume integrated vertical salinity variance on the shelf ($y$-axis) versus the average north-south wind stress over the 12 hours prior to each plume ($x$-axis), with positive indicating a wind blowing north, for every tidal plume in the month of May 2019 (dot = different plume). Colors denote volume and time integrated ratios of dissipation of vertical variance to straining over each ebb pulse. Bin averaged $x$-axis and color bar values are given as the large, outlined dots with error bars representing the standard error of all dissipation – straining ratios.

time integrated over the tidal pulse (colored dots each represent a different tidal plume, Fig. 27). A dissipation – straining ratio greater than 1 in this context indicates more vertical variance is diminished over a 12 h. tide than internally produced (vertical variance input via advection can be destroyed as well, thus allowing the ratio to exceed 1), whereas the same ratio less than 1 means not all the stratification produced from straining on a tidal pulse is destroyed over the tidal pulse. The largest ratios (> 0.8) are almost exclusively produced after northward wind events, with only a few exceptional south wind events producing similar ratios. Fig. 27 therefore provides two main insights: 1.) stratification produced by straining (dominated by the nearfield plume) is most effectively mixed away by dissipation following north wind events when dissipation is enhanced but straining is no longer wind-enhanced, and 2.) dissipation – straining ratios during south or light wind scenarios are generally less than 0.8, indicating more excess vertical variance is created which persists beyond a tidal pulse (ranging from 20 – 60%).

### 3.4. Discussion

Winds which initiate surface currents opposing the direction of Kelvin wave propagation on the shelf tend to decrease net stratification over the control volume most effectively (Fig. 19). After analysis of two tidal plumes under varying winds and all plumes in the full month of May 2019, we attribute the decrease in net stratification to advection of ambient stratification offshore and a subsequent increase in stratified shear mixing in the near and midfield river plume from wind straining and intensified density gradients at the plume base (Fig. 28a). Conversely, winds creating surface currents aimed in the direction of Kelvin wave propagation or weak in magnitude advect the plume and ambient shelf variance nearshore, decrease wind straining relative to the former case, and create a less intense density gradient at the plume base which subsequently leads to less intense mixing (Fig. 28b). Dissipation of variance was

found to remain enhanced following wind events, as long as the ambient shelf is clear of "old" plume stratification.

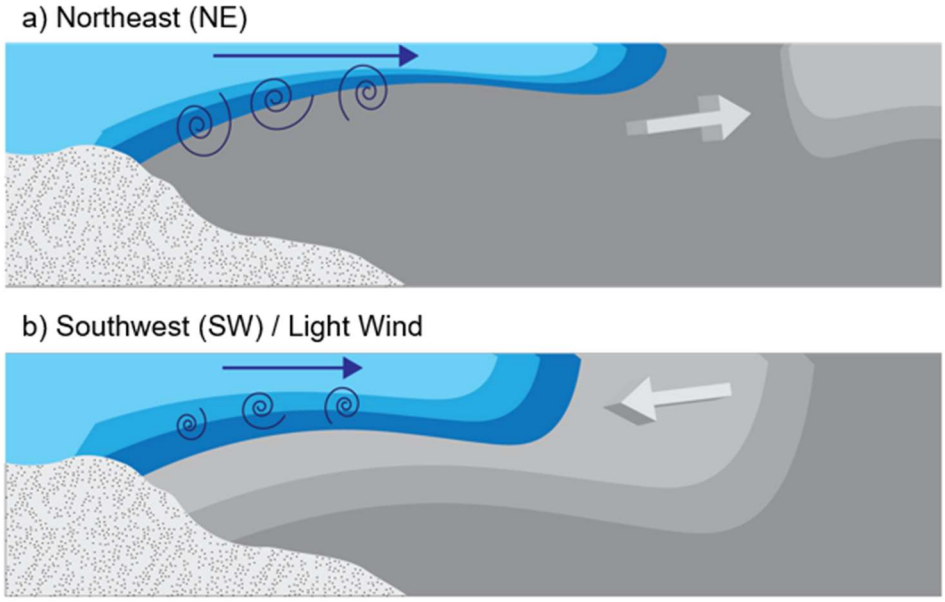


Figure 28: Conceptual diagram showing when mixing in the nearfield of a tidal plume can increase due to wind effects. Blue and gray contours represent water of similar density. Light blue is the freshest plume water, whereas dark gray is the saltiest ambient water. Blue arrows scale with plume velocity magnitude and white 3D arrows point in the direction which winds and surface shelf waters are moving. Mixing intensity scales with the dark blue swirls. Scenarios depict (a) northeastward (NE) and (b) southwestward (SW) / light wind scenario.

### 3.4.1. Tidal Time Scale Wind Transport Effects in the Merrimack and Beyond

This work describes when mixing of a tidal plume may be enhanced under certain winds. Past research investigating wind effects on plumes has primarily identified the far-field region as being prone to modification from wind (e.g., Fong & Geyer, 2001; Hetland, 2005; Lentz, 2004). This study confirms the hypothesis of Kakoulaki et al. (2014): wind can in fact modify nearfield mixing in tidal plumes, and expands on the work of Kastner et al. (2018), who first identified differing nearfield mixing rates from winds. Here we find it valuable to place this work within the context of the Merrimack study by

Kakoulaki et al. (2014), Fraser plume work of Kastner et al. (2018), and others to intercompare and extrapolate these results elsewhere.

A major concept presented in this study is the relatively quick response of both the plume and shelf waters to wind stresses. The advection of plume and shelf stratification offshore, and subsequent replenishment of the near-coast shelf with salty water during northward wind events can occur on a tidal time scale, much more quickly than what typical upwelling-driven Ekman transport would dictate (subtidal). This aligns with results from Kakoulaki et al. (2014) who found instantaneous winds to generally dictate advection in the Merrimack plume when above a 4 m/s threshold (equivalent to the ~0.5 Pa wind stress seen here) and within a 12 km offshore distance from the river mouth, as those winds create surface currents on the order of the barotropic tidally produced plume velocities with relatively fast adjustment times. Winds less than that allow rotation and plume discharge to dominate transport, and the authors speculate larger scale circulation patterns would gain influence in deeper water beyond the midfield plume, or nearshore if winds sustain direction and magnitude at subtidal time scales. Because the Merrimack plume evolves mainly at tidal time scales (similarly to the wind) and is spatially smaller than other major plumes (i.e., the Columbia River), the plume is not influenced in a meaningful way by Ekman processes. Further, the relatively shallower shelf over which the Merrimack plume spreads is less likely to be influenced by significant upwelling or downwelling circulations due to enhanced frictional effects (unlike plumes which discharge over the deeper Pacific shelves for example), allowing ambient shelf stratification to be similarly sensitive to wind (see Fig. 20). Therefore, the direct enhancement or diminishment of velocities in the interior plume during wind events in this study (mainly over 4 m/s, not shown) was considered a significant control on near and midfield straining and dissipation of variance and builds on the work of Kakoulaki et al. (2014).

In the Fraser River plume, Kastner et al. (2018) observed a plume relatively sensitive to wind which dynamically changed depending on whether wind opposed or supported Coriolis in the plume momentum balance. For opposing winds, faster plume currents are produced, and transport is offshore

directed (like in the Merrimack). When winds support the Coriolis force, the plume rotates shoreward relatively more slowly (also like the Merrimack). The findings of Kastner et al. (2018) aid this research in explaining the dynamical behavior of plume transport and velocities under differing winds. We augment the results of Kastner et al. (2018) by connecting wind to straining and advection driven modulation of interior plume variance dissipation, building on and perhaps explaining the mixing trends observed in their work. Although net mixing was larger in the offshore advecting Fraser plume, intensity in the nearfield was not relative to their typical case. It is likely that the deep, tidally flushed Strait of Georgia which controls ambient stratification flushes variance from the river mouth more effectively than at the Merrimack, regardless of wind. Mixing dynamics would therefore rely more on plume geometry [as outlined in Kastner et al. (2018)] and likely the straining discussed in this work rather than the more indirect ambient shelf stratification effects also introduced here.

In the much larger Columbia River plume, winds gain influence on plume dynamics mainly after Ekman dynamics are established (Hickey et al., 1998, 2010). These upwelling / downwelling subtidal circulations are typical over the deep shelf in the region of the Columbia mouth, and stronger than what would be expected in the shallower regions near the Merrimack River mouth. It is likely the findings presented in this work would not apply in the Columbia, as subtidal wind effects are presumably of more importance. That said, results from this study should be extendable to other small to medium sized tidally pulsed plumes over shallow shelves.

### 3.4.2. Limitations and Future Work

Application of the salinity variance equation via numerical methods was particularly amiable in investigating this topic, as real-life conditions often make sampling river plumes in moderate to heavy winds difficult to impossible. That said, there are a few limitations to this research which are worth addressing.

Waves were not modeled in these simulations. Former work has identified breaking waves can have a substantial impact on plume structure and some dynamics, but likely not modify mixing with ambient waters in a meaningful way (Gerbi et al., 2013; Kastner et al., 2018). Further, mixing in the plume front is likely not captured correctly given the hydrostatic assumption utilized in these simulations. Convective instabilities there could create more mixing beyond what is determined in the current experiments and subsequently change the plume footprint and transport.

Numerical mixing of tracers (such as salt) can be created due to discretization errors of tracer advection schemes in numerical ocean models (Burchard & Rennau, 2008). This phenomenon is physically unreal and can result in spurious additional mixing. In the calculations presented, the dissipation term from Equation 20 directly calculates physical mixing and so our estimates of mixing omit numerical errors. That said, numerical mixing can still indirectly modify vertical salinity gradients which consequently modify straining and mixing estimates (Burchard & Rennau, 2008), and so is important to mention. Here, we quantified numerical mixing as the residual of the balance given in Equation 20. Generally, the numerical mixing is small (< 30%) relative to physical mixing during the study period (Fig. 26b) but can become enhanced (> 50%) during some strong straining / mixing events. This is in-line with the findings of Rennau (2011), who found numerically induced mixing may be of similar magnitude to physical mixing when modeling the advection of larger density gradients, such as those around a river plume.

### 3.5. Conclusions

During winds which create surface flow opposing Kelvin wave propagation (typically northward), the Merrimack River plume and ambient shelf stratification advect offshore. Instantaneous wind generally dictates plume and ambient shelf stratification transport due to the short, tidal time scale of plume development and relatively small spatial scales of spreading which prevent subtidal Ekman dynamics from taking influence over the shallow, frictional shelf. Collectively, a relatively homogenous, salty shelf condition is created nearshore. Saltier water beneath the plume creates larger density gradients

at the plume base while offshore directed surface currents increase straining, thereby increasing interfacial mixing intensity in the near and midfield plume relative to other wind directions. Dissipation of vertical variance was found to peak in magnitude on the tide following a northward wind event when straining was less intense, but the shelf was set to a saltier ambient condition, outlining the greater influence of shelf stratification to mixing than straining.

During winds with a southward component or light wind scenarios, the Merrimack River plume behaves as a "typical" tidal plume, spreading out from the river mouth then rotating downcoast due to Coriolis. Advection accumulates excess stratification on the shelf nearshore and straining in the near and midfield is un-enhanced as wind-induced surface velocities oppose the plume and slow offshore propagation, decreasing shear in the plume interior relative to the northward wind case. Less wind straining and a deeper plume base create a less intense interfacial mixing environment between plume and ambient water.

This is the first study providing an evaluation of tidal time scale, realistic wind effects on nearfield and midfield mixing in a medium sized tidally pulsed river plume. Analysis shows the importance of winds in dictating ambient shelf stratification and plume straining, both of which act as controls on mixing (dissipation of variance) in the interior plume. The results of this work are important to consider for future modeling of tracers from land to sea, as transport and mixing can be strongly connected to the wind, even in tidal plumes.

# CHAPTER 4

# EVOLVING INTERIOR MIXING REGIMES IN A TIDAL RIVER PLUME

## 4.1. Introduction

River plumes deliver freshwater laden with sediments, pollutants, nutrients, and other land-sourced tracers to the coastal ocean which can alter biogeochemical processes. Mixing in plumes dilutes freshwater with salty receiving waters and is a major mechanism dictating tracer fate (Horner-Devine et al., 2015). To better track river-borne materials in the coastal zone, it is important to collect observations in real river plumes which provide insight into spatiotemporal variability in mixing and the mechanisms which cause it.

Tidal river plumes pulse a "new" plume seaward on each ebb and exhibit dynamical variability on a tidal time scale. In calm winds, tidal plume mixing is dominated by stratified-shear instabilities in the nearfield region, created by velocity shear and density differences between plume and ambient waters (e.g., Kilcher et al., 2012; MacDonald et al., 2007). Intense mixing is often also observed in the energetic, convergent plume front (Orton & Jay, 2005). Observational data may be used to quantify mixing via the turbulent vertical buoyancy flux, $B$, which can be parameterized using the turbulent kinetic energy (TKE) dissipation rate, $\varepsilon$. To date, observations of $\varepsilon$ and/or $B$ in tidal plumes have either focused on a single region [e.g., the front (Horner-Devine et al., 2013; O'Donnell et al., 2008; Orton & Jay, 2005) or nearfield (Kilcher et al., 2012; MacDonald et al., 2007; MacDonald & Geyer, 2004)] or envelope larger spatial regions but are limited temporally (e.g., Kilcher & Nash, 2010, snapshot at peak ebb discharge). Between nearfield and front, tidal plume mixing is more ambiguous, but likely evolves with intratidally varying currents and stratification in both the plume and ambient shelf [similar to ROFI observations in Simpson et al. (2002)]. It remains unclear how spatiotemporal variability in mixing develops, particularly seaward of the nearfield.

Vertical microstructure profiles of velocity shears provide direct measurements of $\varepsilon$ and capture variability in local mixing which may be omitted using other approaches (e.g., control volume and/or overturn analysis). In this work, we present a novel data set of plume structure and turbulent mixing in the tidal Merrimack River (MR) plume by using microstructure profiling techniques. Measurements connect the plume source to front for three separate transects over an ebb pulse, provide exceptional spatiotemporal resolution in turbulence, and allow us to characterize stratified shear mixing regimes throughout the plume interior as it evolves.

## 4.2 Data Collection and Analysis

### 4.2.1 Study Area and Environmental Conditions

Data were collected in the MR plume in Massachusetts, USA (Fig. 29a) on April 20, 2021. The MR plume is a prototypical surface advected tidal plume which radially expands from the river outflow under calm winds before rotating downcoast (e.g., Hetland & MacDonald, 2008). The plume detaches from the bottom at a 5 m deep sill just seaward of the outflow during ebb when the estuarine salt wedge is forced seaward. At the time of sampling, river discharge (USGS gage #01100000, Lowell, MA) was 260 $m^3s^{-1}$ and the semidiurnal tidal amplitude at the outflow was typical of neap conditions (~1 m, USGS gage #01100870, Newburyport, MA). Winds measured at Isle of Shoals (IOSN3, 15 km north of MR outflow) were calm (< 5 m $s^{-1}$) for the first two sampling transects and a light sea breeze (10 m $s^{-1}$) from the SE began during the third. Wave heights were negligible throughout sampling.

### 4.4.2 Sampling and Processing

Three shipboard source – to – front transects (T1 thru T3) were performed over a ~6 hr. tidal pulse (Fig. 29b, c). T1 occurred ~1.5 hr. after high water just after the plume front exited the river mouth, T2 during maximum ebb discharge, and T3 at the end of ebb near low water. The transecting was designed to follow a streamline mimicking a typical path of plume water under calm conditions. As such, each transect followed the same streamline but became elongated with time as the front moved further

from the mouth. The transect line was roughly calculated using the tracks of four surface bucket drifters [for drifter configuration, see Kakoulaki et al. (2014)] deployed in the MR plume under similar conditions the day prior (April 19, 2020, Fig. 29b).

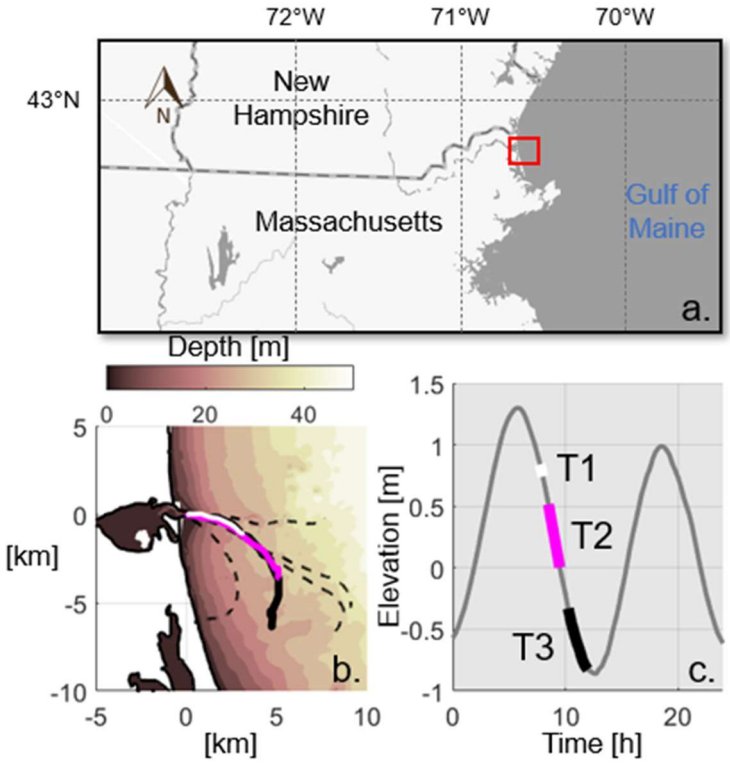


Figure 29: (a) Study location (red box). (b) Zoom in on MR outflow (red box in panel a), with transect routes T1 (white), T2(magenta), and T3 (black) and drifter tracks from previous day (dashed black). Depths are contoured. (c) Sampling times of T1 thru T3 relative to tidal elevation in MR estuary.

On each transect, the vessel towed a 1200 kHz RDI Workhorse Sentinel Acoustic Doppler Current Profiler (ADCP) downward facing on a trimaran at speeds near 2 m $s^{-1}$. The ADCP sampled in "Mode 12", providing east-west ($u$) and north-south ($v$) velocities at 2 Hz. Measurements were taken in 0.15 m bins starting 0.6 m below surface and extended ~16 m deep. Velocity data were ensemble averaged (10 ensembles per average) and data in the bottom 10% of the water column were excluded due to bathymetric interference (if data reached bottom).

Six fixed stations were established along the transecting route (S1 thru S6, Fig. 30). S1 was located between the jetties at the river outflow and is representative of estuary / plume lift-off. S2 featured nearfield plume characteristics during all transects and S3 thru S6 were characteristic of a transitional region between nearfield and midfield ("offshore" stations). The stations were used as waypoints to guide each transect, and if the vessel reached a station after the plume front passed, profiles were collected with a Rockland Scientific MicroCTD. If the vessel reached the front prior to a station, profiles were collected in the front and the transect ended (stations F1 thru F3). During T2, profiles were collected in the ambient waters seaward of the front (station A2). During T3, station S1 was not sampled due to rough water between the jetties. The front was identified visually each time and noted by a defined foam line and/or gradient in water surface roughness. During T2 and T3, the front became more diffuse (multiple foam lines) which made identification of the primary front difficult.

During profiling, engines were turned off, and the vessel drifted freely with the plume. The MicroCTD was deployed in upriser mode and sampled on the ascent from bottom to surface. In deeper water (>10 m), the instrument was released mid water column (~10 m) for temporal efficiency. Two shear probes at the nose of the instrument measured vertical shear in horizontal velocity ($\partial u/\partial z$ and $\partial v/\partial z$) at 512 Hz which was used to estimate $\varepsilon$. Five profiles were taken at each station and averaged together to limit bias from small scale intermittency (Huguenard et al., 2019). Conductivity, temperature, and depth (CTD) data were also measured at 64 Hz to determine density, $\rho$, and density anomaly, $\sigma_t$, then station averaged.

### 4.2.3 Turbulence and Mixing

TKE dissipation rates were determined by integrating the velocity shear spectrum, $\psi$, in wavenumber space with the assumption that turbulence is homogenous and isotropic (Lueck et al., 2002):

$$\varepsilon = \frac{15}{2}\frac{\mu}{\rho}\overline{\left(\frac{\partial u}{\partial z}\right)^2} = \frac{15}{2}\frac{\mu}{\rho}\int \psi(k)\, dk \qquad (20)$$

with $\mu$ being the dynamic viscosity of seawater and $k$ the wavenumber. The Rockland Scientific processing software, ODAS, was used to perform the Equation 20 calculation for each shear probe and utilizes a Nasmyth spectrum to integrate beyond the unresolved part of the spectral variance. A Fast Fourier transform (FFT) length of 0.5 s was used to resolve wavenumbers of interest. Several quality control checks were implemented on each profile to ensure reliable $\varepsilon$ estimates. A Goodman noise removal algorithm was used to correct $\varepsilon$ for instrument vibrations (Goodman et al., 2006). Any portion of an $\varepsilon$ profile with instrument inclination exceeding 10° or ascent speeds exceeding +/- 0.1 m $s^{-1}$ of the terminal velocity (0.9 m $s^{-1}$) was removed. At each depth, the two shear probe estimates of $\varepsilon$ were averaged, and if values differed by more than a factor of 2 the larger value was omitted as it was likely a result of particulates hitting the shear probe (Stips, 2005). The averaged profile of $\varepsilon$ at each station was then interpolated onto the same depth grid as the ADCP.

Buoyancy flux at each station was estimated as:

$$B = -K_z N^2 \qquad (21)$$

where $K_z$ is the eddy diffusivity and $N^2 = -\frac{g}{\rho_0}\frac{\partial \rho}{\partial z}$ is the buoyancy frequency. $K_z$ was parameterized following a processes similar to that of Kay & Jay (2003) in a stratified estuary:

$$K_z = \frac{\varepsilon}{N^2}\Gamma \qquad (22)$$

Where $\Gamma = \frac{R_f}{1-R_f}$ is the mixing efficiency and $R_f$ is the flux Richardson number. Here we model $R_f$ using the gradient Richardson number, $Ri$, and the turbulent Prandtl number, $Pr_t$, as $R_f = Ri\ Pr_t$ . $Ri = \frac{N^2}{S^2}$ is calculated using station-averaged profiles of velocity and density, with $S^2 = \left(\frac{\partial v}{\partial z}\right)^2 + \left(\frac{\partial v}{\partial z}\right)^2$. $Pr_t$ is a function of $Ri$ according to the Tjernstrom parameterization: $Pr_t = \sqrt{1 + 4.47Ri}$ (Tjernstrom, 1993). An upper limit to $R_f$ was set to 0.18, as values above that do not allow turbulence to be maintained at a steady state (Osborn, 1980). The above parameterizations and $R_f$ limit resulted in maximal mixing

efficiencies near ~0.2 in the most intensively stratified and mixed regions of the plume [consistent with former work (Horner-Devine et al., 2015; Ivey & Imberger, 1991)] and < 0.1 in less stratified ambient water.

### 4.3. Plume Structure and Evolution

A two-layer structure was comprised of a relatively fresh but stratified tidal plume ($\sigma_t$ =10 - 24 kg m$^{-3}$) underlain by salty ambient water ($\sigma_t$ =24 - 25 kg m$^{-3}$, Fig. 30g – 2i). In each, the interface between plume and ambient is taken as the deepest local maxima in $N^2$ > 0.025 s$^{-1}$ [similar to Fisher et al. (2018)]. In general, density increases with depth within and below the plume layer (excluding small scale instabilities).

The initial transect (T1) is characteristic of a nearfield jet, with plume velocities unidirectionally offshore (positive *u*, east) and downcoast (negative *v*, south) from source to front (Fig. 30a, 2d). Maximal plume velocity magnitudes in both components (~1 m s$^{-1}$) occur between the lift-off (S1) and S2 and decay vertically and offshore to the plume front (Fig. 30a, 2d). Significant TKE dissipation rates are present over the sill (S1: $\varepsilon$~10$^{-5}$ m$^2$ s$^{-3}$, Fig. 30g) and maximized near surface just offshore (S2: $\varepsilon$~10$^{-4}$ m$^2$ s$^{-3}$) where the plume thins, and shear intensifies. Substantial stratification (S1: $\Delta\sigma_t$ =13 kg m$^{-3}$, S2: $\Delta\sigma_t$ =6 kg m$^{-3}$, Fig. 30g) coincides with large $\varepsilon$ which remains elevated even beneath the plume at S2 ($\varepsilon$~10$^{-6}$ m$^2$ s$^{-3}$, Fig. 30g), suggesting an energetic mixing environment exists from surface to plume base. Intense shear, stratification, and $\varepsilon$ at S2 are characteristic of a nearfield plume (MacDonald et al., 2007), and we refer to the location as such. Below the plume, ambient tidal velocities aim onshore ($u$ ~ 0.2 m s$^{-1}$) and downcoast ($v$ ~ 0.2 m s$^{-1}$), consistent with recorded tidal behavior in the region (Moody et al., 1984).

By mid-ebb (T2), dynamics at the lift-off (S1) and nearfield (S2) resemble T1, with the exception that outflow velocities increase (~1.2 m s$^{-1}$, Fig. 30b, 2e) and the stratified plume deepens (Fig. 2h) as the estuarine salt wedge is pushed closer to the sill. $\varepsilon$ profiles remain maximized near surface in the nearfield (S2: $\varepsilon$~10$^{-4}$ m$^2$ s$^{-3}$) and elevated from surface to sill at lift-off (S1: $\varepsilon$~10$^{-5}$ m$^2$ s$^{-3}$, Fig. 30h), likely due to influence from bottom-generated turbulence. Offshore of the nearfield, velocity isotachs progressively

shoal to the surface, indicating a continued thinning in the vertical extent of intense shear and a slowing of average plume velocities as outflow momentum is lost (Fig. 30b, 2e). $u$ approaches ~0 m $s^{-1}$ within 1 km of the front while $v$ sustains near -0.4 m/s, signifying a downcoast rotation and transition to midfield plume dynamics (e.g., Horner-Devine et al., 2015) at the plume periphery (Fig. 30b, 2e). $\varepsilon$ profiles in this offshore, transitional region (S3, S4) maximize near surface ($10^{-5}$ $m^2$ $s^{-3}$) but decay to the noise limit at the plume base, likely from lessened shear at depth relative to S1 (Fig. 30h). Moderate stratification holds in the plume (S3, S4: $\Delta\sigma_t$ =6 kg $m^{-3}$), presumably allowing substantial stratified shear mixing above the interface.

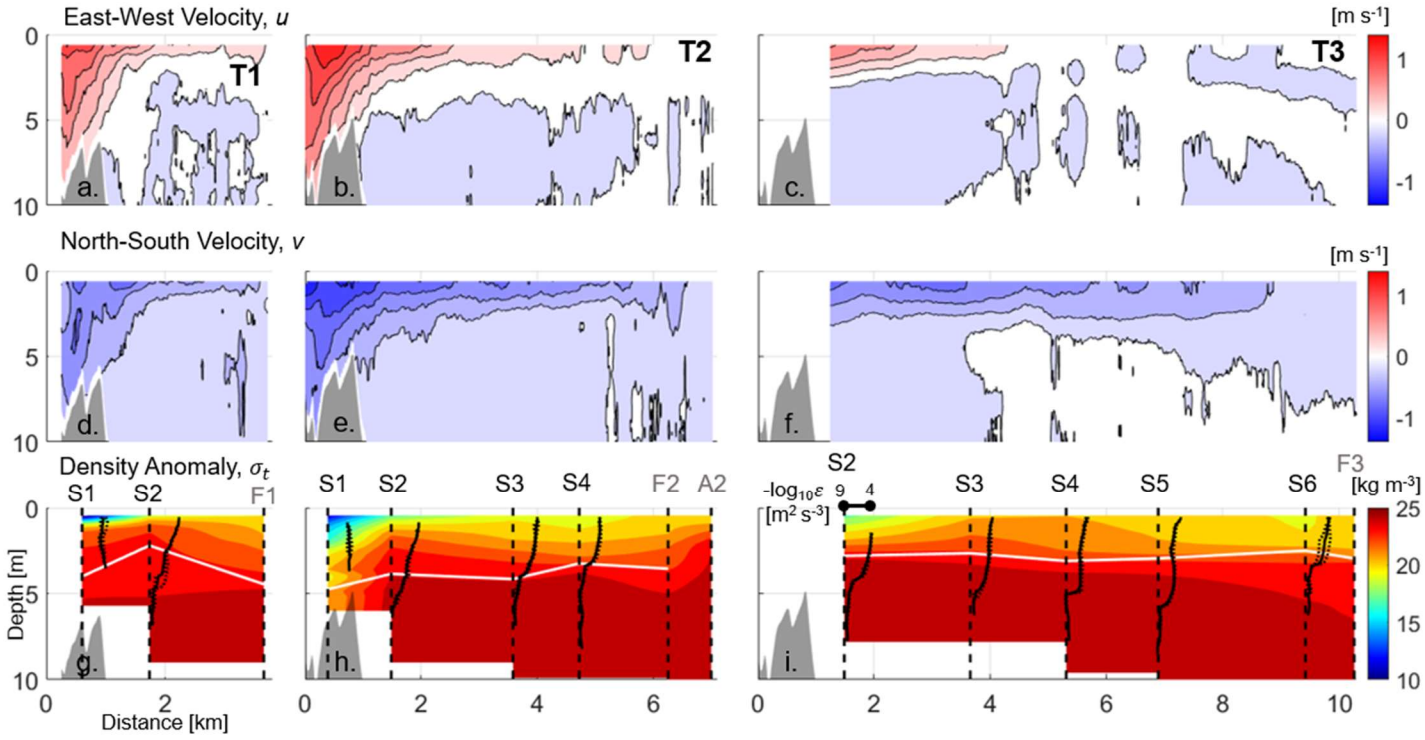


Figure 30: Contours of (a-c) east-west velocities, (d-f) north-south velocities, and (g-i) linearly interpolated density anomaly. Average station locations are labeled and marked with dashed black lines (g-i). Line plots of station averaged TKE dissipation ($log_{10}$) are given at each station with 1 standard deviation (dotted black). White lines (g-i) denote the plume base. Velocity contours are given every 0.2 m $s^{-1}$ and density every 1 kg $m^{-3}$.

At the end of ebb (T3) the nearfield plume (S2) thins as the salt wedge likely begins retreating into the estuary, but outflow velocities remain elevated (~0.8 m $s^{-1}$, Fig. 30c, 2f) and vertically sheared, sustaining enhanced $\varepsilon$ in the plume and below the base ($10^{-5}$ $m^2$ $s^{-3}$, Fig. 30i). Offshore (S3 – S6), a larger region of slow, downcoast propagating plume water exists relative to T2 ($u$ = 0 m $s^{-1}$, $v$ = 0.2 – 0.6 m $s^{-1}$) and areas of ~0 m $s^{-1}$ velocities ($u$ and $v$) approach the plume base from bottom (Fig. 30c, 2f), coinciding with a switch in tidal phase on the shelf. Tidal velocities lead elevation in the region by ~1 h and begin rotating north/east prior to low water (Moody et al., 1984). The switch in ambient tide direction occurs first at depth, allowing the plume layer to continue propagating downcoast (Fig. 30f) but increases shear and $\varepsilon$ at and below the base (S3 – S6: $\varepsilon$~$10^{-6}$ $m^2$ $s^{-3}$, Fig. 30i). $\varepsilon$ within the plume moderates ($\varepsilon$~$10^{-6}$-$10^{-5}$ $m^2$ $s^{-3}$, Fig. 30i) with slowing velocities, as does stratification ($\Delta\sigma_t$ =2 - 4 kg $m^{-3}$, Fig. 30i), likely from sustained mixing over the former ~5 hours.

### 4.4. Turbulent Mixing Regimes

Seaward of the liftoff (S1), two broad types of $\varepsilon$ profiles are evident in each transect: those maximizing near surface and minimizing at the plume base (i.e., T2: S3, S4) and those minimizing below the plume base (i.e., T1: S2, T2: S2, T3: S2 – S6); all being consistent with internally generated shear instability (no bottom influence). Here, we identify if shear and stratification which modulate $\varepsilon$ profiles promote buoyant mixing at each interior location (section 4.4.1), then present estimates of mixing (buoyancy flux) and distinguish differences in mixing regimes which correspond to the aforementioned $\varepsilon$ types (section 4.4.2).

#### 4.4.1 Stratification vs. Velocity Shear

Turbulence is expected to mix buoyancy when $Ri$ is less than a critical value between 0.25 and 0.32 (or decomposed as $S^2 > 4N^2$ for $Ri$ < 0.25) (Thorpe, 1987), but can sometimes approach 1 (Giddings et al., 2011). We use $Ri$ to identify when stratified shear mixing is expected in the interior plume and explicitly link mixing-prone conditions to shear and stratification trends previously outlined.

Throughout ebb, shear is enhanced ($S^2$~$10^{-1.5}$-$10^{-1}$ $s^{-2}$) over the full plume layer in the nearfield (S2, T1 – T3, Fig. 31a, 3b, 3e) and dominates stratification ($4N^2$). Subsequently, mixing is likely from plume base to surface ($Ri < 0.25$), as is typical of nearfield plumes (i.e., MacDonald et al., 2007). Surface maxima in $S^2$ suggests shear is driven mainly by outflow inertia, typical of a buoyant jet (Luketina & Imberger, 1987).

Intratidal variability in *Ri* develops offshore of the nearfield as the plume grows. Near mid ebb (T2), $S^2$ decreases at the plume base (~$10^{-2}$ $s^{-2}$) moving offshore (S3, S4) as plume velocities slow away from the outflow and the nearfield jet shear decays. Conversely, $4N^2$ increases at the base (~$10^{-1}$ $s^{-2}$), as diminished $\varepsilon$ there allows stratification to stabilize. *Ri* exceeds 0.25, signifying a transition to unfavorable

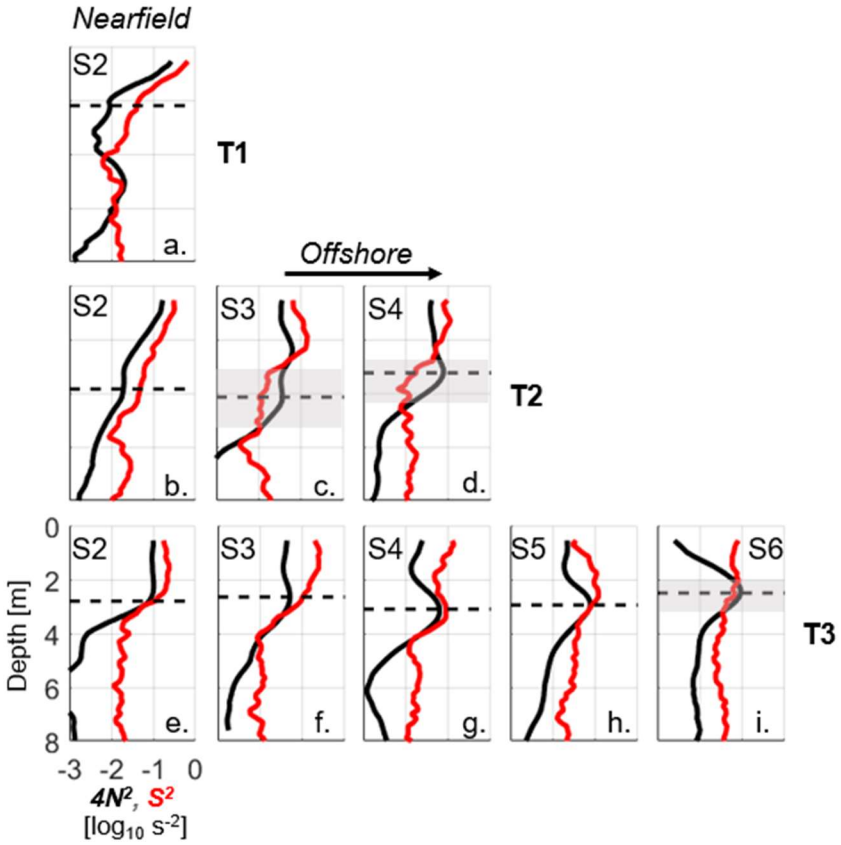


Figure 31: Station averaged squared shear (red) and 4x buoyancy frequency (black) for (a) T1, (b-d) T2, and (e-i) T3 on a $\log_{10}$ scale (*x*-axis). Dashed black lines indicate plume base depth. Gray boxes shade regions of $Ri > 0.25$ at or above the plume base. Profiles are smoothed over 5 vertical coordinates.

mixing conditions at the plume interface. Above the interface, shear remains dominant over stratification, and mixing is expected ($Ri < 0.25$, Fig. 31c, 3d).

At the end of ebb (T3), stratification at the plume base offshore (S3 – S6) is largely unchanged ($4N^2$~$10^{-1}$ $s^{-2}$), but shear increases ($S^2$~$10^{-1}$ $s^{-2}$) relative to T2 as ambient tidal currents rotate at depth. Local enhancement of $S^2$ at depth relative to former transects acts on the pycnocline [not unlike that observed in an estuary (Giddings et al., 2011)], differing from the surface maximized shear described previously. Subsequently, *Ri* decreases below 0.25 at the plume base at S3 thru S5 and is near 0.35 at S6. Above the base at the same stations (S3 – S6), shear decreases ($S^2$~$10^{-1.5}$-$10^{-1}$ $s^{-2}$) relative to T2 as the plume continues to slow, as does stratification ($4N^2$~$10^{-2}$-$10^{-1.5}$ $s^{-2}$) from presumably large mixing in the plume layer throughout the tide. Even so, *Ri* remains below 0.25, and mixing is expected from interface to surface (Fig. 31f – 3i).

### 4.4.2 Buoyancy Flux and Mixing Regimes

*Ri* profiles suggest when mixing conditions are likely but do not directly quantify mixing. The vertical turbulent buoyancy flux (Equation 21) is evaluated to quantify mixing and is sorted by density class to condense data from multiple stations. A corresponding buoyancy Reynold's number ($Re_b = \frac{\varepsilon}{\nu N^2}$, with $\nu$ being the kinematic viscosity of seawater) is also given to nondimensionalize the effectiveness of turbulence at mixing buoyancy and corroborate *Ri* trends which fail to characterize turbulent behavior (Fig. 32). $Re_b$ below a value ranging from 15 to 30 indicates stratification completely suppresses mixing and near zero entrainment. $Re_b$ increasing above 30 means turbulence is capable of initiating vertical entrainment and buoyant mixing with increasing effectiveness (Luketina & Imberger, 1989). Using $Re_b$, we identify three stratified shear mixing regimes: plume layer mixing ($Re_b > 30$ above plume base), nearfield interfacial mixing ($Re_b > 30$ at/below plume base in nearfield), and tidal interfacial mixing ($Re_b > 30$ at/below plume base offshore of nearfield). Each regime is described below. $Re_b$ was not calculated for $\varepsilon$ near the noise limit ($10^{-9}$-$10^{-8}$ $m^2$ $s^{-3}$) to constrain *x*-axis limits (Fig. 32b, 32e, 32h).

During the initial nearfield jet (T1), $B$ maximizes in the plume layer ($10^{-5}$ m$^2$ s$^{-3}$) and decays sharply over the plume base ($10^{-6}$ to $10^{-8}$ m$^2$ s$^{-3}$, Fig. 32a), showing intense mixing from surface to interface. $Re_b$ above 30 holds over the plume's vertical extent ($Re_b$ ~1000) and at the base ($Re_b$ ~3000, Fig. 32b). As such, we identify internal shear generated turbulence to be effective at mixing buoyancy in the nearfield via two regimes: mixing of density classes within the plume (plume layer mixing) and between plume and underlying ambient water (interfacial nearfield mixing, Fig. 32c). Both regimes are driven by surface maximized jet-like shear, which decays with depth but remains significant enough to promote mixing from surface to base. The well-developed stratified shear mixing in the nearfield is expected (Horner-Devine et al., 2015) and matches trends in $Ri$ outlined above. Further, $B$ profiles hold mid-plume maxima, typical of actively spreading regions like the nearfield (Yuan & Horner-Devine, 2013).

At mid ebb (T2), plume layer $B$ in the nearfield (S2) dominates other stations, sustaining values near $10^{-5}$ m$^2$ s$^{-3}$, with moderation at the interface ($10^{-7}$ m$^2$ s$^{-3}$, Fig. 32d) relative to T1. Correspondingly, $Re_b$ exceeds 30 in the plume and at the base but is notably decreased (~100) around the interface relative to T1 (Fig. 32e), indicating less intense interfacial mixing (Fig. 32f) from an increase in outflow stratification at max ebb. Offshore, plume layer $B$ decreases with distance from mouth (S3: $10^{-6}$ m$^2$ s$^{-3}$, S4: $10^{-7}$ m$^2$ s$^{-3}$) and becomes nearly negligible at the plume base (S3, S4: $10^{-8}$ m$^2$ s$^{-3}$), like $\varepsilon$. $Re_b$ above 30 in the plume layer (~500) and between 15 - 30 at the base (Fig. 32e) confirm plume layer mixing to be effective, but interfacial mixing to be suppressed beyond the nearfield (Fig. 32f). Lessening jet-like shear (from slower plume velocities) and increasing stratification at the interface offshore of the nearfield account for this dynamical change. Importantly, the diminishment of interfacial mixing indicates the plume propagates for some time near max ebb with minimal exchange (offshore of nearfield) with the ambient shelf in a transitional state not depicted in previous literature.

Plume layer and interfacial $B$ in the nearfield (S2) remains strong ($10^{-5}$ m$^2$ s$^{-3}$, Fig. 32g), even at the end of ebb (T3), with correspondingly large $Re_b$ (~1000, Fig. 32h, 32i). Seaward of the nearfield (S3 – S6), plume layer $B$ moderates ($10^{-7}$ m$^2$ s$^{-3}$, Fig. 32g) as shear and stratification decrease relative to T2. Meanwhile, shear and $\varepsilon$ at the plume base increase, driven by a directional shift in tidal currents, allowing modest mixing to develop at and below the plume base (~$10^{-7}$ m$^2$ s$^{-3}$, Fig. 32g), similar in magnitude to mixing above the base. On average, $Re_b$ offshore (S3-S6) is of order 50 (Fig. 32h), indicating $B$ can, in some capacity, mix plume water with ambient (Fig 32i). Interfacial mixing offshore is driven by locally intensified shear at the pycnocline created by evolving ambient currents, differing from interfacial mixing

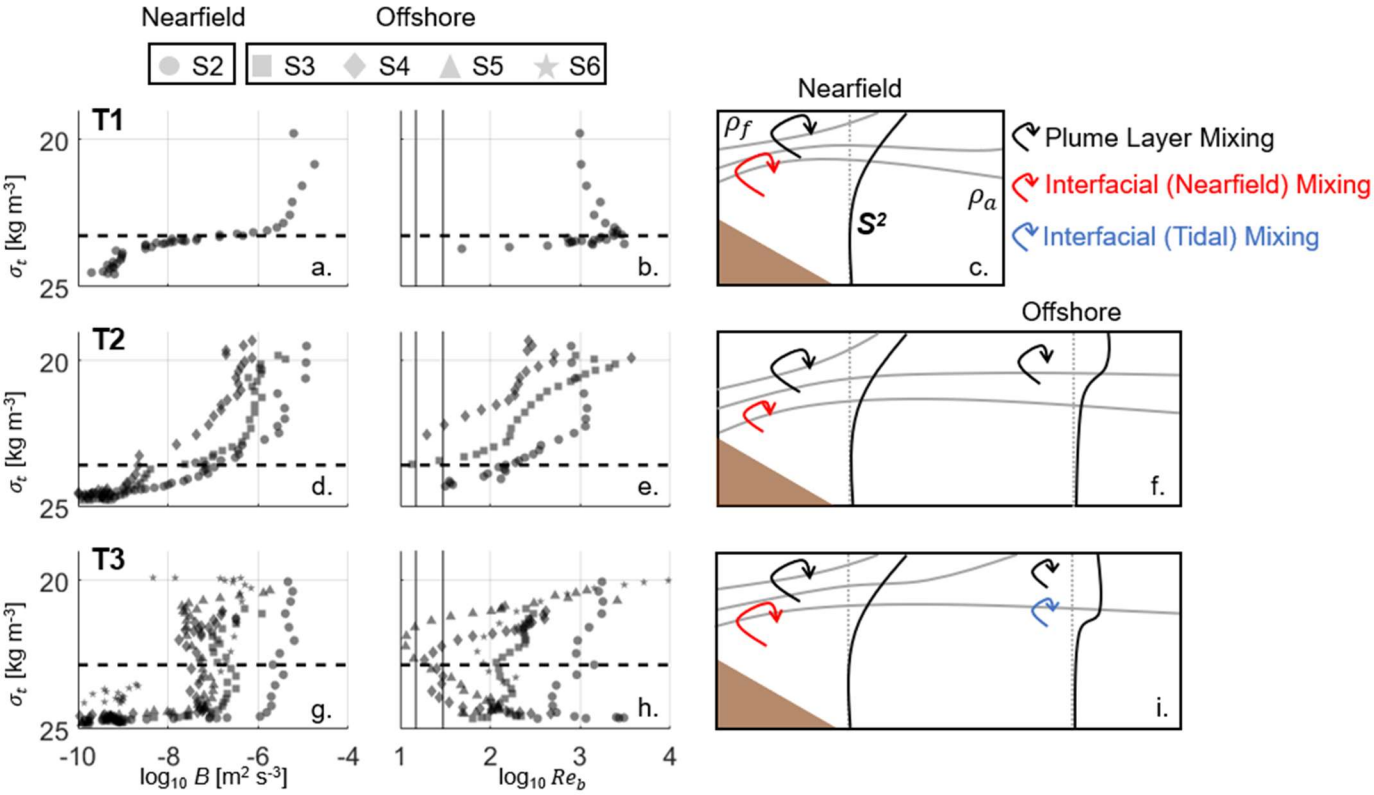


Figure 32: (a, d, g) Density class sorted buoyancy flux at S2 – S6. (b, e, h) Corresponding buoyancy Reynolds numbers, omitting when $\varepsilon < 10^{-8}$. Average plume base $\sigma_t$ is shown with a dashed black line and vertical lines (b, e, h) denote $Re_b = 15$ and 30. (c, f, i) Conceptual schematic of plume isopycnals (gray) ranging from fresh water ($\rho_f$) to salty, ambient water ($\rho_a$), shear (black curves), and mixing regimes (circle arrows).

driven by the nearfield jet. This "tidal" interfacial mixing produces significant variability in $Re_b$ station to station, though, and is most effective at the plume base near S3 and S6 ($Re_b$~100) and ineffective at S4 and S5 ($Re_b$< 30), highlighting a transient nature to turbulence and the mechanism. Regardless of spatial variability, all offshore locations see $Re_b > 30$ immediately above and below the plume base, indicating mixing occurs on both sides of the interface which likely destroys the boundary with time. Intermittent mixing at the interface and larger *B* at depth are more characteristic of a far-field plume (A. W. Fisher et al., 2018), demonstrating further transition from tidal plume to coastal current.

To estimate the relative importance of tidal interfacial mixing to the other regimes, the mixing ratio of Horner-Devine et al. (2015), *M*, was evaluated for each regime:

$$M = 2\frac{\sum B_n A_n}{g'_f Q}\gamma T^* \qquad (23)$$

and describes the rate of energy converted to mixing from a specific process to the total potential energy of the plume layer leaving the estuary. In Equation 23, *A* is an estimated horizontal area over which *B* from station *n* acts while $\gamma = g'_M\left(g'_f - g'_M\right)^{-1}$, $g'_M$ is the reduced gravity at a final mixed state, $g'_f$ is the reduced gravity at the mouth, *Q* is river discharge, and $T^*$ is the fraction of the tidal cycle for which a process occurs. Estimates indicate plume layer mixing accounts for 41% of mixing energy ($M$ = 0.41) while nearfield interfacial accounts for 14% and tidal interfacial 2%. Summing the mechanisms suggests 57% of the plume potential energy mixes away on an ebb pulse, leaving a remaining 43% to mix out in the far-field plume, and is consistent with recent estimates of net mixing (Chapter 1). The calm wind and ambient shelf state shown in this work gives perhaps one of the least significant tidal interfacial mixing scenarios, yet it still occurs and perhaps increases in importance progressing into the flood tide. It is likely tidal interfacial mixing is quite important for plumes over strongly tidal shelves (i.e., Connecticut and Rhine River plumes) or those with shelf currents sensitive to wind (i.e., the MR plume during windy conditions).

### 4.5. Summary

Detailed observations in the interior MR plume over a tidal pulse characterize the spatiotemporal evolution of multiple stratified shear mixing regimes (plume layer, nearfield interfacial, and tidal interfacial). Plume layer mixing acts on stratification within the plume itself while nearfield and tidal interfacial mixing transfer buoyancy across the plume base. Significant surface maximized, jet-like shear and stratification in the nearfield allow sustained plume layer and interfacial mixing ($B$~$10^{-6}$-$10^{-5}$ $m^2$ $s^{-3}$) which dominate spatially throughout the ebb tide. As the plume grows near mid-ebb, surface flow slows and shear at the plume base decreases offshore of the nearfield, subsequently suppressing interfacial mixing and moderating plume layer mixing ($B$~$10^{-7}$-$10^{-6}$ $m^2$ $s^{-3}$). At the end of ebb, tidal currents reverse direction below the plume, locally increase shear at the plume base, and initiate modest tidal interfacial mixing ($B$~$10^{-7}$ $m^2$ $s^{-3}$) while plume layer mixing moderates further ($B$~$10^{-7}$ $m^2$ $s^{-3}$). We hypothesize that the ambient shelf current structure is important in controlling interfacial mixing offshore of the nearfield, and likely varies significantly system to system, with these results depicting a relatively weaker tidal interfacial mixing case.

These observations outline the transition of a tidal plume from nearfield jet to transitional states characteristic of mid and far-field plumes. It is likely the mixing regimes described vary in importance depending on a variety of factors (environmental, bathymetric, etc.) and should be explored more in future work. Increasing spatial and temporal resolution in plume mixing estimates is important to better understanding the fate of river water transported to the coastal ocean.

# CHAPTER 5

# CONCLUSIONS

This dissertation explores the mechanisms which contribute to mixing tidally pulsed river plumes into shelf seas. Both local and global mixing analyses are performed. We outline numerous ways stratified shear mixing may be modulated by environmental conditions (river discharge, tides, wind) and how it evolves spatially and temporally in a "typical" plume. Further, we quantify the relative importance of stratified shear mixing (interfacial) to bottom generated (tidal) and frontal mixing under variable forcing. The research questions outlined in Section 1.2 are addressed with realistic and idealized numerical modeling simulations, as well as observational data taken in the Merrimack River plume. In all experiments, observations, and analyses, a common theme was identified: the ambient shelf condition, defined by coastal stratification and currents, can be a significant control on tidal plume mixing. From this overarching theme, three major conclusions are formed.

First, bottom generated tidal mixing has the potential to dominate the net mixing of a tidal plume during an ebb discharge. When tidal power on the shelf exceeds the buoyant input from river discharge (here, defined as $Ri_E R_o^{-1} < 1$), bottom generated mixing may comprise up to 90% of total plume mixing. When buoyant input exceeds tidal power ($Ri_E R_o^{-1} > 1$), interfacial mixing dominates. In other words, significant tidal currents under a plume have the potential to control how that plume mixes, and the relative importance of tidal mixing is influenced by the strength of river discharge. This study is the first to outline the importance of bottom-generated mixing from tides on some surface advected plumes. In all tide and discharge cases studied, frontal mixing never exceeds 10% of the net mixing budget and is another notable finding.

Second, winds varying at short, tidal time scales can modulate interfacial mixing in the near and midfield plume by modulating plume currents and coastal stratification. Winds which generally counter the downcoast (in direction of Coriolis force) rotation of tidal plumes, regardless of magnitude, are

effective at advecting ambient shelf stratification offshore and increasing plume layer velocities. When stratification is pushed away from the river mouth, a saltier ambient shelf forms, subsequently increasing the vertical salinity gradient at the plume base. Simultaneously, the faster plume enhances vertical shear between plume and ambient. The intensified salinity gradient coupled with increased shear allow for stratified shear mixing magnitudes to increase, particularly in the nearfield. Although straining is also enhanced, thereby increasing stratification, the relative importance of de-stratifying processes (mixing) is greater than stratifying processes (straining). This work is the first to quantify and diagnose the net changes in tidal plume nearfield mixing caused by wind-driven modulation to the shelf condition.

Lastly, we found that stratified shear mixing may act to dilute plume water via three different regimes in a tidal plume during calm winds: we name them nearfield interfacial mixing, plume layer mixing, and tidal interfacial mixing. Nearfield interfacial mixing mixes over the plume – ambient interface in the energetic, jet-like nearfield and sustains intense, concentrated mixing over a tidal pulse near the river mouth. Plume layer mixing is responsible for mixing buoyancy within the stratified plume and always exists but becomes weaker offshore of the nearfield as the tide progresses. Tidal interfacial mixing occurs near the end of ebb tide when ambient shelf currents begin switching direction at depth, thereby enhancing shear, and mixing at the plume base. Plume layer mixing contributes the most to net mixing energy (~40%) as it encompasses the majority of the plume volume over the entire ebb tide. Each form of interfacial mixing contributes less as they act over smaller spatial (nearfield interfacial, ~14%) or temporal (tidal interfacial, ~2%) scales, but are likely important in setting initial and final tidal plume dynamics. This is the first study to capture the evolution of interior mixing observationally in a tidal plume as it evolves from nearfield jet to a rotational, mid-field plume. Further, this work is the first to identify how ambient tidal currents may modulate interfacial plume mixing.

Although this research improves our understanding of tidal plume mixing processes, and how the ambient shelf may adjust mixing, there are still gaps in our understanding to be addressed in future and partnering work. Currently, partnering work is more comprehensively studying the role of the front in

tidal plume mixing, particularly how the front itself evolves over spatial and temporal scales, and its contribution to total plume mixing. Although this work takes a first step at incorporating frontal mixing into a mixing budget, the hydrostatic framework utilized in ROMS is likely unable to capture defining frontal characteristics such as convective instabilities at the plunging, bore-like head which create further mixing. Further, the front presumably changes in width and energetics with time and should be defined by a similarly dynamic length scale for analysis. Observational data allowing for the determination of the spatiotemporal evolution of frontal turbulence and volume will build on this work considerably, as well as non-hydrostatic modeling of the plume and front.

There is amble opportunity to distinguish the relative importance of bottom-generated tidal mixing to tidal interfacial mixing in plumes. In this work, we have identified the two mechanisms, with analyses focusing on one or the other. It seems likely the two processes occur simultaneously, and presumably influence tidal plume dynamics to varying degrees based on location, forcing, etc. Further observational and numerical modeling work in strongly tidal plume-shelf systems like the Connecticut River plume and Long Island Sound would allow a more holistic investigation of the topic. Additionally, observational data capturing local bottom-generated tidal mixing on real surface plumes will reinforce the idealized modeling work presented here.

This work has drawn connections between plume-shelf interactions and tidal plume mixing. Other important research questions and lines of work can be derived from this theme. For one, if variable shelf-dictated conditions modify plume conditions, how does the estuary respond? The estuary and plume together are typically not studied as one whole system, particularly when analyzing mixing. There is opportunity to integrate the two and analyze the trickle-down effects of shelf conditions (stratification, currents, topography, bathymetry) through the entire system. Further, how do storm-driven shelf conditions (i.e., surge, extreme winds, and extreme waves) affect mixing and transport in tidal plumes? As climate change increases storminess in many regions, it becomes important to understand storm

effects more completely to inform predictive models of tracers. New ocean observing technology (unmanned drifters, for example) and numerical modeling can be used to address this question.

In general, this dissertation enhances the current knowledge base on buoyancy driven flows in the coastal environment and can be utilized in improving predictive modeling of tidal river plumes. Enhancing our understanding of the fundamental physics which govern river plumes is critical in accurately assessing the plethora of biogeochemical processes occurring in the coastal zone (i.e., hypoxia, algal blooms, plankton growth, fishery health, etc.) which are modulated by circulation and mixing of ocean and river water. Further, by bettering local and global mixing estimates at estuarine outflows, river inputs to large scale ocean models become better integrated and connected, improving the accuracy of much larger scale simulations and analyses (i.e., ocean climate models). This work has broad applicability and is a considerable contribution improving our understanding of the evolution of mixing in tidal river plumes.

## BIBLIOGRAPHY


Ackleson, S. G., & O'Donnell, J. (2011). Small-scale variability in suspended matter associated with the Connecticut River plume front. *Journal of Geophysical Research*, *116*(C10), C10013. https://doi.org/10.1029/2011JC007053

Akan, Ç., McWilliams, J. C., Moghimi, S., & Özkan-Haller, H. T. (2018). Frontal dynamics at the edge of the Columbia River plume. *Ocean Modelling*. https://doi.org/10.1016/j.ocemod.2017.12.001

Avicola, G., & Huq, P. (2002). Scaling Analysis for the Interaction between a Buoyant Coastal Current and the Continental Shelf: Experiments and Observations. *Journal of Physical Oceanography*, *32*(11), 3233–3248. https://doi.org/10.1175/1520-0485(2002)032<3233:SAFTIB>2.0.CO;2

Bennett, D. C., O'Donnell, J., Bohlen, W. F., & Houk, A. (2010). Tides and Overtides in Long Island Sound. *Journal of Marine Research*, *68*(1), 1–35. https://doi.org/10.1357/002224010793079031

de Boer, G. J., Pietrzak, J. D., & Winterwerp, J. C. (2006). On the vertical structure of the Rhine region of freshwater influence. In *Ocean Dynamics*. https://doi.org/10.1007/s10236-005-0042-1

de Boer, G. J., Pietrzak, J. D., & Winterwerp, J. C. (2008). Using the potential energy anomaly equation to investigate tidal straining and advection of stratification in a region of freshwater influence. *Ocean Modelling*. https://doi.org/10.1016/j.ocemod.2007.12.003

Bowman, M. J., & Esaias, W. E. (1981). Fronts, stratification, and mixing in Long Island and Block Island sounds. *Journal of Geophysical Research*. https://doi.org/10.1029/jc086ic05p04260

Burchard, H., & Hofmeister, R. (2008). A dynamic equation for the potential energy anomaly for analysing mixing and stratification in estuaries and coastal seas. *Estuarine, Coastal and Shelf Science*. https://doi.org/10.1016/j.ecss.2007.10.025

Burchard, H., & Rennau, H. (2008). Comparative quantification of physically and numerically induced mixing in ocean models. *Ocean Modelling*, *20*(3), 293–311. https://doi.org/10.1016/j.ocemod.2007.10.003

Burchard, H., Lange, X., Klingbeil, K., & MacCready, P. (2019). Mixing Estimates for Estuaries. *Journal of Physical Oceanography*, *49*(2), 631–648. https://doi.org/10.1175/JPO-D-18-0147.1

Canuto, V. M., Howard, A., Cheng, Y., & Dubovikov, M. S. (2001). Ocean turbulence. Part I: One-point closure model-momentum and heat vertical diffusivities. *Journal of Physical Oceanography*. https://doi.org/10.1175/1520-0485(2001)031<1413:OTPIOP>2.0.CO;2

Chapman, D. C. (1985). Numerical treatment of cross-shelf open boundaries in a barotropic coastal ocean model. *J. PHYS. OCEANOGR.* https://doi.org/10.1175/1520-0485(1985)015<1060:ntocso>2.0.co;2

Chen, F., MacDonald, D. G., & Hetland, R. D. (2009). Lateral spreading of a near-field river plume: Observations and numerical simulations. *Journal of Geophysical Research*, *114*(C7), C07013. https://doi.org/10.1029/2008JC004893

Chen, S. Y., & Chen, S. N. (2017). Generation of upwelling circulation under downwelling-favorable wind within bottom-attached, buoyant coastal currents. *Journal of Physical Oceanography*. https://doi.org/10.1175/JPO-D-16-0271.1

Cole, K. L. (2014). *A numerical study of the mid-field river plume*. Texas A&M University.

Cole, K. L., & Hetland, R. D. (2016). The effects of rotation and river discharge on net mixing in small-mouth Kelvin number plumes. *Journal of Physical Oceanography*. https://doi.org/10.1175/JPO-D-13-0271.1

Cole, K. L., MacDonald, D. G., Kakoulaki, G., & Hetland, R. D. (2020). River plume source-front connectivity. *Ocean Modelling*. https://doi.org/10.1016/j.ocemod.2020.101571

Deignan-Schmidt, S. R., & Whitney, M. M. (2018). A Model Study on the Summertime Distribution of River Waters in Long Island Sound. *Estuaries and Coasts*, *41*(4), 1002–1020. https://doi.org/10.1007/s12237-017-0348-5

Devine, J. (2014). *The Impacts of Beach Pollution*. *Testing the Waters: 24th Edition*.

Fischer, H. B. (1972). Mass transport mechanisms in partially stratified estuaries. *Journal of Fluid Mechanics*. https://doi.org/10.1017/S0022112072000412

Fisher, A. W., Nidzieko, N. J., Scully, M. E., Chant, R. J., Hunter, E. J., & Mazzini, P. L. F. (2018). Turbulent Mixing in a Far-Field Plume During the Transition to Upwelling Conditions: Microstructure Observations From an AUV. *Geophysical Research Letters*. https://doi.org/10.1029/2018GL078543

Fisher, N. R., Simpson, J. H., & Howarth, M. J. (2002). Turbulent dissipation in the Rhine ROFI forced by tidal flow and wind stress. In *Journal of Sea Research*. https://doi.org/10.1016/S1385-1101(02)00194-6

Flater, D. (2005). XTide: Harmonic tide clock and tide predictor. Retrieved from https://flaterco.com/xtide/

Flather, R. A. (1975). A tidal model of the north-west European continental shelf. *MEM. SOC. ROYALE SCI. DE LIEGE, SER.6*.

Flores, R. P., Rijnsburger, S., Horner-Devine, A. R., Souza, A. J., & Pietrzak, J. D. (2017). The impact of storms and stratification on sediment transport in the Rhine region of freshwater influence. *Journal of Geophysical Research: Oceans*. https://doi.org/10.1002/2016JC012362

Fong, D. A., & Geyer, W. (2001). Response of a river plume during an upwelling favorable wind event. *Journal of Geophysical Research: Oceans*. https://doi.org/10.1029/2000JC900134

Fong, D. A., & Geyer, W. R. (2002). The Alongshore Transport of Freshwater in a Surface-Trapped River Plume*. *Journal of Physical Oceanography*, *32*(3), 957–972. https://doi.org/10.1175/1520-0485(2002)032<0957:TATOFI>2.0.CO;2

Fong, D. A., Geyer, W. R., & Signell, R. P. (1997). The wind-forced response on a buoyant coastal current: Observations of the western Gulf of Maine plume. *Journal of Marine Systems*, *12*(1–4), 69–81. https://doi.org/10.1016/S0924-7963(96)00089-9

Garvine, R. W. (1974). PHYSICAL FEATURES OF THE CONNECTICUT RIVER OUTFLOW DURING HIGH DISCHARGE. *J. GEOPHYSICAL RES.* https://doi.org/10.1029/jc079i006p00831

Garvine, R. W. (1977). OBSERVATIONS OF THE MOTION FIELD OF THE CONNECTICUT RIVER PLUME. *J Geophys Res*. https://doi.org/10.1029/JC082i003p00441

Garvine, R. W. (1984). Radial spreading of buoyant, surface plumes in coastal waters. *Journal of Geophysical Research*, *89*(C2), 1989. https://doi.org/10.1029/JC089iC02p01989

Garvine, R. W. (1987). Estuary plumes and fronts in shelf waters: a layer model. *J. PHYS. OCEANOGR.* https://doi.org/10.1175/1520-0485(1987)017<1877:epafis>2.0.co;2

Garvine, R. W., & Monk, J. D. (1974). Frontal Structure of a River Plume. *Journal of Geophysical Research*. https://doi.org/10.1029/jc079i015p02251

Gerbi, G. P., Chant, R. J., & Wilkin, J. L. (2013). Breaking Surface Wave Effects on River Plume Dynamics during Upwelling-Favorable Winds. *Journal of Physical Oceanography*, *43*(9), 1959–1980. https://doi.org/10.1175/JPO-D-12-0185.1

Geyer, W. R., & MacCready, P. (2014). The Estuarine Circulation. *Annual Review of Fluid Mechanics*. https://doi.org/10.1146/annurev-fluid-010313-141302

Geyer, W. R., Signell, R. P., Fong, D. A., Wang, J., Anderson, D. M., & Keafer, B. A. (2004). The freshwater transport and dynamics of the western Maine coastal current. *Continental Shelf Research*, *24*(12), 1339–1357. https://doi.org/10.1016/j.csr.2004.04.001

Geyer, W. R., Scully, M. E., & Ralston, D. K. (2008). Quantifying vertical mixing in estuaries. In *Environmental Fluid Mechanics*. https://doi.org/10.1007/s10652-008-9107-2

Geyer, W. R., Lavery, A. C., Scully, M. E., & Trowbridge, J. H. (2010). Mixing by shear instability at high Reynolds number. *Geophysical Research Letters*, *37*(22), n/a-n/a. https://doi.org/10.1029/2010GL045272

Giddings, S. N., Fong, D. A., & Monismith, S. G. (2011). Role of straining and advection in the intratidal evolution of stratification, vertical mixing, and longitudinal dispersion of a shallow, macrotidal, salt wedge estuary. *Journal of Geophysical Research*, *116*(C3), C03003. https://doi.org/10.1029/2010JC006482

Goodman, L., Levine, E. R., & Lueck, R. G. (2006). On measuring the terms of the turbulent kinetic energy budget from an AUV. *Journal of Atmospheric and Oceanic Technology*. https://doi.org/10.1175/JTECH1889.1

Gregg, M. . (2004). Small-scale processes in straits. *Deep Sea Research Part II: Topical Studies in Oceanography*, *51*(4–5), 489–503. https://doi.org/10.1016/j.dsr2.2003.08.003

Haidvogel, D. B., Arango, H., Budgell, W. P., Cornuelle, B. D., Curchitser, E., Di Lorenzo, E., et al. (2008). Ocean forecasting in terrain-following coordinates: Formulation and skill assessment of the Regional Ocean Modeling System. *Journal of Computational Physics*. https://doi.org/10.1016/j.jcp.2007.06.016

Halverson, M. J., & Pawlowicz, R. (2008). Estuarine forcing of a river plume by river flow and tides. *Journal of Geophysical Research: Oceans*. https://doi.org/10.1029/2008JC004844

Hetland, R. D. (2005). Relating river plume structure to vertical mixing. *Journal of Physical Oceanography*. https://doi.org/10.1175/JPO2774.1

Hetland, R. D. (2010). The effects of mixing and spreading on density in near-field river plumes. *Dynamics of Atmospheres and Oceans*, *49*(1), 37–53. https://doi.org/10.1016/j.dynatmoce.2008.11.003

Hetland, R. D., & DiMarco, S. F. (2008). How does the character of oxygen demand control the structure of hypoxia on the Texas–Louisiana continental shelf? *Journal of Marine Systems*, *70*(1–2), 49–62. https://doi.org/10.1016/j.jmarsys.2007.03.002

Hetland, R. D., & MacDonald, D. G. (2008). Spreading in the near-field Merrimack River plume. *Ocean Modelling*. https://doi.org/10.1016/j.ocemod.2007.11.001

Hickey, B. M., Pietrafesa, L. J., Jay, D. A., & Boicourt, W. C. (1998). The Columbia River Plume Study: Subtidal variability in the velocity and salinity fields. *Journal of Geophysical Research: Oceans*, *103*(C5), 10339–10368. https://doi.org/10.1029/97JC03290

Hickey, B. M., Kudela, R. M., Nash, J. D., Bruland, K. W., Peterson, W. T., MacCready, P., et al. (2010). River Influences on Shelf Ecosystems: Introduction and synthesis. *Journal of Geophysical Research*, *115*, C00B17. https://doi.org/10.1029/2009JC005452

Holleman, R. C., Geyer, W. R., & Ralston, D. K. (2016). Stratified turbulence and mixing efficiency in a salt wedge estuary. *Journal of Physical Oceanography*. https://doi.org/10.1175/JPO-D-15-0193.1

Horner-Devine, A. R. (2009). The bulge circulation in the Columbia River plume. *Continental Shelf Research*, *29*(1), 234–251. https://doi.org/10.1016/j.csr.2007.12.012

Horner-Devine, A. R., Jay, D. A., Orton, P. M., & Spahn, E. Y. (2009). A conceptual model of the strongly tidal Columbia River plume. *Journal of Marine Systems*, *78*(3), 460–475. https://doi.org/10.1016/j.jmarsys.2008.11.025

Horner-Devine, A. R., Chickadel, C. C., & MacDonald, D. G. (2013). Coherent Structures and Mixing at a River Plume Front. In *Coherent Flow Structures at Earth's Surface*. https://doi.org/10.1002/9781118527221.ch23

Horner-Devine, A. R., Hetland, R. D., & MacDonald, D. G. (2015). Mixing and Transport in Coastal River Plumes. *Annual Review of Fluid Mechanics*. https://doi.org/10.1146/annurev-fluid-010313-141408

Houghton, R. W., Chant, R. J., Rice, A., & Tilburg, C. (2009). Salt flux into coastal river plumes: Dye studies in the Delaware and Hudson river outflows. *Journal of Marine Research*. https://doi.org/10.1357/002224009792006142

Huguenard, K., Bogucki, D. J., Ortiz-Suslow, D. G., Laxague, N. J. M., MacMahan, J. H., Özgökmen, T. M., et al. (2016). On the nature of the frontal zone of the Choctawhatchee Bay plume in the Gulf of Mexico. *Journal of Geophysical Research: Oceans*. https://doi.org/10.1002/2015JC010988

Huguenard, K., Bears, K., & Lieberthal, B. (2019). Intermittency in Estuarine Turbulence: A Framework toward Limiting Bias in Microstructure Measurements. *Journal of Atmospheric and Oceanic Technology*. https://doi.org/10.1175/jtech-d-18-0220.1

Hunter, E. J., Chant, R. J., Wilkin, J. L., & Kohut, J. (2010). High-frequency forcing and subtidal response of the Hudson River plume. *Journal of Geophysical Research*, *115*(C7), C07012. https://doi.org/10.1029/2009JC005620

Itsweire, E. C., Koseff, J. R., Briggs, D. A., & Ferziger, J. H. (1993). Turbulence in stratified shear flows: implications for interpreting shear-induced mixing in the ocean. *Journal of Physical Oceanography*. https://doi.org/10.1175/1520-0485(1993)023<1508:TISSFI>2.0.CO;2

Ivey, G. N., & Imberger, J. (1991). On the Nature of Turbulence in a Stratified Fluid. Part I: The Energetics of Mixing. *Journal of Physical Oceanography*, *21*(5), 650–658. https://doi.org/10.1175/1520-0485(1991)021<0650:OTNOTI>2.0.CO;2

Ivey, G. N., Winters, K. B., & Koseff, J. R. (2008). Density Stratification, Turbulence, but How Much Mixing? *Annual Review of Fluid Mechanics*. https://doi.org/10.1146/annurev.fluid.39.050905.110314

Jia, Y., & Whitney, M. M. (2019). Summertime Connecticut River Water Pathways and Wind Impacts. *Journal of Geophysical Research: Oceans*. https://doi.org/10.1029/2018JC014486

Jones, G. R., Nash, J. D., Doneker, R. L., & Jirka, G. H. (2007). Buoyant surface discharges into water bodies. I: Flow classification and prediction methodology. *Journal of Hydraulic Engineering*. https://doi.org/10.1061/(ASCE)0733-9429(2007)133:9(1010)

Jurisa, J. T., & Chant, R. J. (2013). Impact of offshore winds on a buoyant river plume system. *Journal of Physical Oceanography*. https://doi.org/10.1175/JPO-D-12-0118.1

Jurisa, J. T., Nash, J. D., Moum, J. N., & Kilcher, L. F. (2016). Controls on Turbulent Mixing in a Strongly Stratified and Sheared Tidal River Plume. *Journal of Physical Oceanography*, *46*(8), 2373–2388. https://doi.org/10.1175/JPO-D-15-0156.1

Kakoulaki, G. (2015). Using Lagrangean Surface Drifters to Study Wind Forcing and Lateral Spreading in a Buoyant River Plume. *Thesis*.

Kakoulaki, G., Macdonald, D., & Horner-Devine, A. R. (2014). The role of wind in the near field and midfield of a river plume. *Geophysical Research Letters*. https://doi.org/10.1002/2014GL060606

Kakoulaki, G., MacDonald, D. G., & Cole, K. (2020). Calculating lateral plume spreading with surface Lagrangian drifters. *Limnology and Oceanography: Methods*. https://doi.org/10.1002/lom3.10356

Kastner, S. E., Horner-Devine, A. R., & Thomson, J. (2018). The Influence of Wind and Waves on Spreading and Mixing in the Fraser River Plume. *Journal of Geophysical Research: Oceans*. https://doi.org/10.1029/2018JC013765

Kay, D. J., & Jay, D. A. (2003). Interfacial mixing in a highly stratified estuary 1. Characteristics of mixing. *Journal of Geophysical Research C: Oceans*. https://doi.org/10.1029/2000jc000252

Kilcher, L. F., & Nash, J. D. (2010). Structure and dynamics of the Columbia River tidal plume front. *Journal of Geophysical Research: Oceans*. https://doi.org/10.1029/2009JC006066

Kilcher, L. F., Nash, J. D., & Moum, J. N. (2012). The role of turbulence stress divergence in decelerating a river plume. *Journal of Geophysical Research: Oceans*. https://doi.org/10.1029/2011JC007398

Kourafalou, V. H., & Androulidakis, Y. S. (2013). Influence of Mississippi River induced circulation on the Deepwater Horizon oil spill transport. *Journal of Geophysical Research: Oceans*, *118*(8), 3823–3842. https://doi.org/10.1002/jgrc.20272

Lentz, S. (2004). The response of buoyant coastal plumes to upwelling-favorable winds. *Journal of Physical Oceanography*. https://doi.org/10.1175/JPO2647.1

Lentz, S., & Fewings, M. R. (2012). The wind- and wave-driven inner-shelf circulation. *Annual Review of Marine Science*. https://doi.org/10.1146/annurev-marine-120709-142745

Li, X., Geyer, W. R., Zhu, J., & Wu, H. (2018). The Transformation of Salinity Variance: A New Approach to Quantifying the Influence of Straining and Mixing on Estuarine Stratification. *Journal of Physical Oceanography*, *48*(3), 607–623. https://doi.org/10.1175/JPO-D-17-0189.1

Lorenz, M., Klingbeil, K., & Burchard, H. (2021). Impact of Evaporation and Precipitation on Estuarine Mixing. *Journal of Physical Oceanography*, *51*(4), 1319–1333. https://doi.org/10.1175/JPO-D-20-0158.1

Lueck, R. G., Wolk, F., & Yamazaki, H. (2002). Oceanic velocity microstructure measurements in the 20th century. *Journal of Oceanography*. https://doi.org/10.1023/A:1015837020019

Luketina, D. A., & Imberger, J. (1987). Characteristics of a surface buoyant jet. *Journal of Geophysical Research: Oceans*. https://doi.org/10.1029/JC092iC05p05435

Luketina, D. A., & Imberger, J. (1989). Turbulence and entrainment in a buoyant surface plume. *Journal of Geophysical Research*, *94*(C9), 12619. https://doi.org/10.1029/JC094iC09p12619

MacCready, P., Banas, N. S., Hickey, B. M., Dever, E. P., & Liu, Y. (2009). A model study of tide- and wind-induced mixing in the Columbia River Estuary and plume. *Continental Shelf Research*. https://doi.org/10.1016/j.csr.2008.03.015

MacCready, P., Geyer, W. R., & Burchard, H. (2018). Estuarine Exchange Flow Is Related to Mixing through the Salinity Variance Budget. *Journal of Physical Oceanography*, *48*(6), 1375–1384. https://doi.org/10.1175/JPO-D-17-0266.1

MacDonald, D. G., & Chen, F. (2012). Enhancement of turbulence through lateral spreading in a stratified-shear flow: Development and assessment of a conceptual model. *Journal of Geophysical Research: Oceans*, *117*(C5), n/a-n/a. https://doi.org/10.1029/2011JC007484

MacDonald, D. G., & Geyer, W. R. (2004). Turbulent energy production and entrainment at a highly stratified estuarine front. *Journal of Geophysical Research C: Oceans*. https://doi.org/10.1029/2003JC002094

MacDonald, D. G., & Horner-Devine, A. R. (2008). Temporal and spatial variability of vertical salt flux in a highly stratified estuary. *Journal of Geophysical Research: Oceans*. https://doi.org/10.1029/2007JC004620

MacDonald, D. G., Goodman, L., & Hetland, R. D. (2007). Turbulent dissipation in a near-field river plume: A comparison of control volume and microstructure observations with a numerical model. *Journal of Geophysical Research: Oceans*. https://doi.org/10.1029/2006JC004075

MacDonald, D. G., Carlson, J., & Goodman, L. (2013). On the heterogeneity of stratified-shear turbulence: Observations from a near-field river plume. *Journal of Geophysical Research: Oceans*, *118*(11), 6223–6237. https://doi.org/10.1002/2013JC008891

Marchesiello, P., McWilliams, J. C., & Shchepetkin, A. (2001). Open boundary conditions for long-term integration of regional oceanic models. *Ocean Modelling*. https://doi.org/10.1016/S1463-5003(00)00013-5

Marmorino, G. O., & Trump, C. L. (2000). Gravity current structure of the Chesapeake Bay outflow plume. *Journal of Geophysical Research: Oceans*, *105*(C12), 28847–28861. https://doi.org/10.1029/2000JC000225

McCabe, R. M., Hickey, B. M., & MacCready, P. (2008). Observational estimates of entrainment and vertical salt flux in the interior of a spreading river plume. *Journal of Geophysical Research: Oceans*. https://doi.org/10.1029/2007JC004361

McCabe, R. M., MacCready, P., & Hickey, B. M. (2009). Ebb-Tide Dynamics and Spreading of a Large River Plume*. *Journal of Physical Oceanography*, *39*(11), 2839–2856. https://doi.org/10.1175/2009JPO4061.1

Miles, J. W. (1961). On the stability of heterogeneous shear flows. *Journal of Fluid Mechanics*. https://doi.org/10.1017/S0022112061000305

Milligan, T. G., Hill, P. S., & Law, B. A. (2007). Flocculation and the loss of sediment from the Po River plume. *Continental Shelf Research*, *27*(3–4), 309–321. https://doi.org/10.1016/j.csr.2006.11.008

Moffat, C., & Lentz, S. (2012). On the response of a buoyant plume to downwelling-favorable wind stress. *Journal of Physical Oceanography*. https://doi.org/10.1175/JPO-D-11-015.1

Moody, J. A., Butman, B., Beardsley, R. C., Brown, W. S., Daifuku, P., Irish, J. D., et al. (1984). *Atlas of Tidal Elevation and Current Observations on the Northeast American Continental Shelf and Slope*. Alexandria, VA.

Moum, J. N., Gregg, M. C., Lien, R. C., & Carr, M. E. (1995). Comparison of Turbulence Kinetic Energy Dissipation Rate Estimates from Two Ocean Microstructure Profilers. *Journal of Atmospheric and Oceanic Technology*. https://doi.org/10.1175/1520-0426(1995)012<0346:cotked>2.0.co;2

Nash, J. D., & Moum, J. N. (2005). River plumes as a source of large-amplitude internal waves in the coastal ocean. *Nature*. https://doi.org/10.1038/nature03936

Nash, J. D., Kilcher, L. F., & Moum, J. N. (2009). Structure and composition of a strongly stratified, tidally pulsed river plume. *Journal of Geophysical Research: Oceans*. https://doi.org/10.1029/2008JC005036

O'Donnell, J. (1997). Observations of near-surface currents and hydrography in the Connecticut River plume with the surface current and density array. *Journal of Geophysical Research C: Oceans*. https://doi.org/10.1029/97JC01008

O'Donnell, J., Ackleson, S. G., & Levine, E. R. (2008). On the spatial scales of a river plume. *Journal of Geophysical Research: Oceans*. https://doi.org/10.1029/2007JC004440

O'Donnell, J., Wilson, R. E., Lwiza, K., Whitney, M., Bohlen, W. F., Codiga, D., et al. (2014). The Physical Oceanography of Long Island Sound. https://doi.org/10.1007/978-1-4614-6126-5_3

Orlanski, I. (1976). A simple boundary condition for unbounded hyperbolic flows. *Journal of Computational Physics*, *21*(3), 251–269. https://doi.org/10.1016/0021-9991(76)90023-1

Orton, P. M., & Jay, D. A. (2005). Observations at the tidal plume front of a high-volume river outflow. *Geophysical Research Letters*. https://doi.org/10.1029/2005GL022372

Osborn, T. R. (1980). Estimates of the Local Rate of Vertical Diffusion from Dissipation Measurements. *Journal of Physical Oceanography*. https://doi.org/10.1175/1520-0485(1980)010<0083:eotlro>2.0.co;2

Pritchard, M., & Huntley, D. A. (2006). A simplified energy and mixing budget for a small river plume discharge. *Journal of Geophysical Research: Oceans*. https://doi.org/10.1029/2005JC002984

Ralston, D. K., Geyer, W. R., & Lerczak, J. A. (2010). Structure, variability, and salt flux in a strongly forced salt wedge estuary. *Journal of Geophysical Research*, *115*(C6), C06005. https://doi.org/10.1029/2009JC005806

Ralston, D. K., Geyer, W. R., Lerczak, J. A., & Scully, M. (2010). Turbulent mixing in a strongly forced salt wedge estuary. *Journal of Geophysical Research: Oceans*. https://doi.org/10.1029/2009JC006061

Ralston, D. K., Cowles, G. W., Geyer, W. R., & Holleman, R. C. (2017). Turbulent and numerical mixing in a salt wedge estuary: Dependence on grid resolution, bottom roughness, and turbulence closure. *Journal of Geophysical Research: Oceans*, *122*(1), 692–712. https://doi.org/10.1002/2016JC011738

Rascle, N., Chapron, B., Molemaker, J., Nouguier, F., Ocampo-Torres, F. J., Osuna Cañedo, J. P., et al. (2020). Monitoring Intense Oceanic Fronts Using Sea Surface Roughness: Satellite, Airplane, and In Situ Comparison. *Journal of Geophysical Research: Oceans*, *125*(8). https://doi.org/10.1029/2019JC015704

Rennau, H. (2011). *Natural, numerical and structure-induced mixing in dense gravity currents: Idealised and realistic model studies*. University of Rostock.

Rijnsburger, S., Flores, R. P., Pietrzak, J. D., Horner-Devine, A. R., & Souza, A. J. (2018). The Influence of Tide and Wind on the Propagation of Fronts in a Shallow River Plume. *Journal of Geophysical Research: Oceans*. https://doi.org/10.1029/2017JC013422

Rijnsburger, S., Flores, R. P., Pietrzak, J. D., Horner-Devine, A. R., Souza, A. J., & Zijl, F. (2021). The Evolution of Plume Fronts in the Rhine Region of Freshwater Influence. *Journal of Geophysical Research: Oceans*, *126*(7). https://doi.org/10.1029/2019JC015927

Scully, M. E., Friedrichs, C., & Brubaker, J. (2005). Control of estuarine stratification and mixing by wind-induced straining of the estuarine density field. *Estuaries*, *28*(3), 321–326. https://doi.org/10.1007/BF02693915

Shchepetkin, A. F., & McWilliams, J. C. (2005). The regional oceanic modeling system (ROMS): a split-explicit, free-surface, topography-following-coordinate oceanic model. *Ocean Modelling*, *9*(4), 347–404. https://doi.org/10.1016/j.ocemod.2004.08.002

Sherman, F. S., Imberger, J., & Corcos, G. M. (1978). TURBULENCE AND MIXING IN STABLY STRATIFIED WATERS. *Annu Rev Fluid Mech*. https://doi.org/10.1146/annurev.fl.10.010178.001411

Simmon, R. (2011). Sediment Spews from Connecticut River. Retrieved January 3, 2022, from https://earthobservatory.nasa.gov/images/52059/sediment-spews-from-connecticut-river

Simpson, J. H., & Bowers, D. (1981). Models of stratification and frontal movement in shelf seas. *Deep Sea Research Part A, Oceanographic Research Papers*. https://doi.org/10.1016/0198-0149(81)90132-1

Simpson, J. H., Brown, J., Matthews, J., & Allen, G. (1990). Tidal straining, density currents, and stirring in the control of estuarine stratification. *Estuaries*. https://doi.org/10.2307/1351581

Simpson, John H., Burchard, H., Fisher, N. R., & Rippeth, T. P. (2002). The semi-diurnal cycle of dissipation in a ROFI: Model-measurement comparisons. In *Continental Shelf Research*. https://doi.org/10.1016/S0278-4343(02)00025-0

Smolarkiewicz, P. K., & Grabowski, W. W. (1990). The multidimensional positive definite advection transport algorithm: nonoscillatory option. *Journal of Computational Physics*. https://doi.org/10.1016/0021-9991(90)90105-A

Smyth, W. D., & Moum, J. N. (2000). Length scales of turbulence in stably stratified mixing layers. *Physics of Fluids*. https://doi.org/10.1063/1.870385

Smyth, W. D., Moum, J. N., & Caldwell, D. R. (2001). The Efficiency of Mixing in Turbulent Patches: Inferences from Direct Simulations and Microstructure Observations. *Journal of Physical Oceanography*, *31*(8), 1969–1992. https://doi.org/10.1175/1520-0485(2001)031<1969:TEOMIT>2.0.CO;2

Spahn, E. Y., Horner-Devine, A. R., Nash, J. D., Jay, D. A., & Kilcher, L. (2009). Particle resuspension in the Columbia River plume near field. *Journal of Geophysical Research: Oceans*. https://doi.org/10.1029/2008JC004986

Stacey, M. T., Rippeth, T. P., & Nash, J. D. (2012). Turbulence and Stratification in Estuaries and Coastal Seas. In *Treatise on Estuarine and Coastal Science*. https://doi.org/10.1016/B978-0-12-374711-2.00204-7

Stashchuk, N., & Vlasenko, V. (2009). Generation of internal waves by a supercritical stratified plume. *Journal of Geophysical Research*, *114*(C1), C01004. https://doi.org/10.1029/2008JC004851

Stips, A. (2005). Dissipation measurement: Theory. In H. Z. Baumert, J. H. Simpson, & J. Sundermann (Eds.), *Marine turbulence: Theories, observations and models* (pp. 115–126). Cambridge, U.K.: Cambridge University Press.

Thomson, J. (2012). Wave Breaking Dissipation Observed with “SWIFT” Drifters. *Journal of Atmospheric and Oceanic Technology*, *29*(12), 1866–1882. https://doi.org/10.1175/JTECH-D-12-00018.1

Thomson, J., Horner-Devine, A. R., Zippel, S., Rusch, C., & Geyer, W. (2014). Wave breaking turbulence at the offshore front of the Columbia River Plume. *Geophysical Research Letters*. https://doi.org/10.1002/2014GL062274

Thorpe, S. A. (1969). Experiments on the Stability of Stratified Shear Flows. *Radio Science*, *4*(12), 1327–1331. https://doi.org/10.1029/RS004i012p01327

Thorpe, S. A. (1971). Experiments on the instability of stratified shear flows: miscible fluids. *Journal of Fluid Mechanics*, *46*(2), 299–319. https://doi.org/10.1017/S0022112071000557

Thorpe, S. A. (1987). Transitional phenomena and the development of turbulence in stratified fluids: A review. *Journal of Geophysical Research*, *92*(C5), 5231. https://doi.org/10.1029/JC092iC05p05231

Tilburg, C. E. (2003). Across-Shelf Transport on a Continental Shelf: Do Across-Shelf Winds Matter? *Journal of Physical Oceanography*, *33*(12), 2675–2688. https://doi.org/10.1175/1520-0485(2003)033<2675:ATOACS>2.0.CO;2

Tjernstrom, M. (1993). Turbulence length scales in stably stratified free shear flow analyzed from slant aircraft profiles. *Journal of Applied Meteorology*. https://doi.org/10.1175/1520-0450(1993)032<0948:TLSISS>2.0.CO;2

Trenberth, K. E., Smith, L., Qian, T., Dai, A., & Fasullo, J. (2007). Estimates of the global water budget and its annual cycle using observational and model Data. *Journal of Hydrometeorology*. https://doi.org/10.1175/JHM600.1

Umlauf, L., & Burchard, H. (2003). A generic length-scale equation for geophysical turbulence models. *Journal of Marine Research*. https://doi.org/10.1357/002224003322005087

Valle-Levinson, A. (2010). *Contemporary issues in estuarine physics*. *Contemporary Issues in Estuarine Physics*. https://doi.org/10.1017/CBO9780511676567

Visser, A., Souza, A. J., Hessner, K., & Simpson, J. H. (1994). The effect of stratification on tidal current profiles in a region of freshwater influence. *Oceanologica Acta*, *17*(4), 369–381.

Wang, T., & Geyer, W. R. (2018). The Balance of Salinity Variance in a Partially Stratified Estuary: Implications for Exchange Flow, Mixing, and Stratification. *Journal of Physical Oceanography*, *48*(12), 2887–2899. https://doi.org/10.1175/JPO-D-18-0032.1

Warner, J. C., Geyer, W. R., Ralston, D. K., & Kalra, T. (2020). Using Tracer Variance Decay to Quantify Variability of Salinity Mixing in the Hudson River Estuary. *Journal of Geophysical Research: Oceans*, *125*(12). https://doi.org/10.1029/2020JC016096

Warrick, J. A., & Stevens, A. W. (2011). A buoyant plume adjacent to a headland-Observations of the Elwha River plume. *Continental Shelf Research*. https://doi.org/10.1016/j.csr.2010.11.007

Whitney, M. M., & Garvine, R. W. (2005). Wind influence on a coastal buoyant outflow. *Journal of Geophysical Research C: Oceans*. https://doi.org/10.1029/2003JC002261

Whitney, M. M., Ullman, D. S., & Codiga, D. L. (2016). Subtidal exchange in eastern Long Island Sound. *Journal of Physical Oceanography*. https://doi.org/10.1175/JPO-D-15-0107.1

Whitney, M. M., Jia, Y., Cole, K. L., MacDonald, D. G., & Huguenard, K. D. (2021). Freshwater composition and connectivity of the Connecticut River plume during ambient flood tides. *Frontiers in Marine Science*.

Winters, K. B., Lombard, P. N., Riley, J. J., & D'Asaro, E. A. (1995). Available potential energy and mixing in density-stratified fluids. *Journal of Fluid Mechanics*. https://doi.org/10.1017/S002211209500125X

Wunsch, C., & Ferrari, R. (2004). VERTICAL MIXING, ENERGY, AND THE GENERAL CIRCULATION OF THE OCEANS. *Annual Review of Fluid Mechanics*. https://doi.org/10.1146/annurev.fluid.36.050802.122121

Yankovsky, A. E., & Chapman, D. C. (1997). A simple theory for the fate of buoyant coastal discharges. *Journal of Physical Oceanography*. https://doi.org/10.1175/1520-0485(1997)027<1386:ASTFTF>2.0.CO;2

Yellen, B., Woodruff, J. D., Cook, T. L., & Newton, R. M. (2016). Historically unprecedented erosion from Tropical Storm Irene due to high antecedent precipitation. *Earth Surface Processes and Landforms*, *41*(5), 677–684. https://doi.org/10.1002/esp.3896

Yellen, B., Woodruff, J. D., Ralston, D. K., MacDonald, D. G., & Jones, D. S. (2017). Salt wedge dynamics lead to enhanced sediment trapping within side embayments in high-energy estuaries. *Journal of Geophysical Research: Oceans*, *122*(3), 2226–2242. https://doi.org/10.1002/2016JC012595

Yuan, Y., & Horner-Devine, A. R. (2013). Laboratory investigation of the impact of lateral spreading on buoyancy flux in a river plume. *Journal of Physical Oceanography*. https://doi.org/10.1175/JPO-D-12-0117.1

Zhang, Z., Hetland, R., & Zhang, X. (2014). Wind-modulated buoyancy circulation over the Texas-Louisiana shelf. *Journal of Geophysical Research C: Oceans*. https://doi.org/10.1002/2013JC009763

## APPENDIX A

Interior Grid Points (*k*-points):

***Condition 1**: $d_\tau > d_p$ (Interfacial Mixing Only, Fig. 4a)*

$$M_{IF} = \rho_0 \sum_{i=0}^{k} A_i \int_{d_{p_i}}^{\eta} B_i \, dz \tag{A1}$$

$$M_T = 0 \tag{A2}$$

***Condition 2**: $d_\tau < d_p$ (Interfacial and Tidal Mixing, Fig. 4c)*

$$M_{IF} = \rho_0 \sum_{i=0}^{k} A_i \int_{d_{\tau_i}}^{\eta} B_i \, dz \tag{A3}$$

$$M_T = \left[\rho_0 \sum_{i=0}^{k} A_i \int_{d_{p_i}}^{\eta} B_i \, dz\right] - \left[\rho_0 \sum_{i=0}^{k} A_i \int_{d_{\tau_i}}^{\eta} B_i \, dz\right] \tag{A4}$$

***Condition 3**: $d_\tau$ does not exist (Tidal Mixing Only, Fig. 4b)*

$$M_{IF} = 0 \tag{A5}$$

$$M_T = \rho_0 \sum_{i=0}^{k} A_i \int_{d_{p_i}}^{\eta} B_i \, dz \tag{A6}$$

Frontal Grid Points (*j*-points):

***Condition 1**: $d_\tau > d_f$ (Frontal Mixing Only)*

$$M_{FR} = \rho_0 \sum_{i=0}^{j} A_i \int_{d_{f_i}}^{\eta} B_i \, dz \tag{A7}$$

$$M_T = 0 \tag{A8}$$

***Condition 2**: $d_\tau < d_f$ (Frontal and Tidal Mixing)*

$$M_{FR} = \rho_0 \sum_{i=0}^{j} A_i \int_{d_{\tau_i}}^{\eta} B_i \, dz \quad \text{(A9)}$$

$$M_T = \left[\rho_0 \sum_{i=0}^{j} A_i \int_{d_{f_i}}^{\eta} B_i \, dz\right] - \left[\rho_0 \sum_{i=0}^{j} A_i \int_{d_{\tau_i}}^{\eta} B_i \, dz\right] \quad \text{(A10)}$$

***Condition 3****: $d_\tau$ does not exist (Tidal Mixing Only)*

$$M_{FR} = 0 \quad \text{(A11)}$$

$$M_T = \rho_0 \sum_{i=0}^{j} A_i \int_{d_{f_i}}^{\eta} B_i \, dz \quad \text{(A12)}$$

## APPENDIX B

An empirical orthogonal function (EOF) analysis was performed for a large tide run which related tidal mixing power within the plume layer (Equation 14) to tidal mixing power in the ambient layer beneath the plume: $M_A = \left[\rho_0 \sum_{i=0}^{n} A_i \int_{d_{p_i}}^{H} B_i \, dz\right]$, where $H$ is the total depth of the water column. The modes in Fig. B1 are interpreted as:

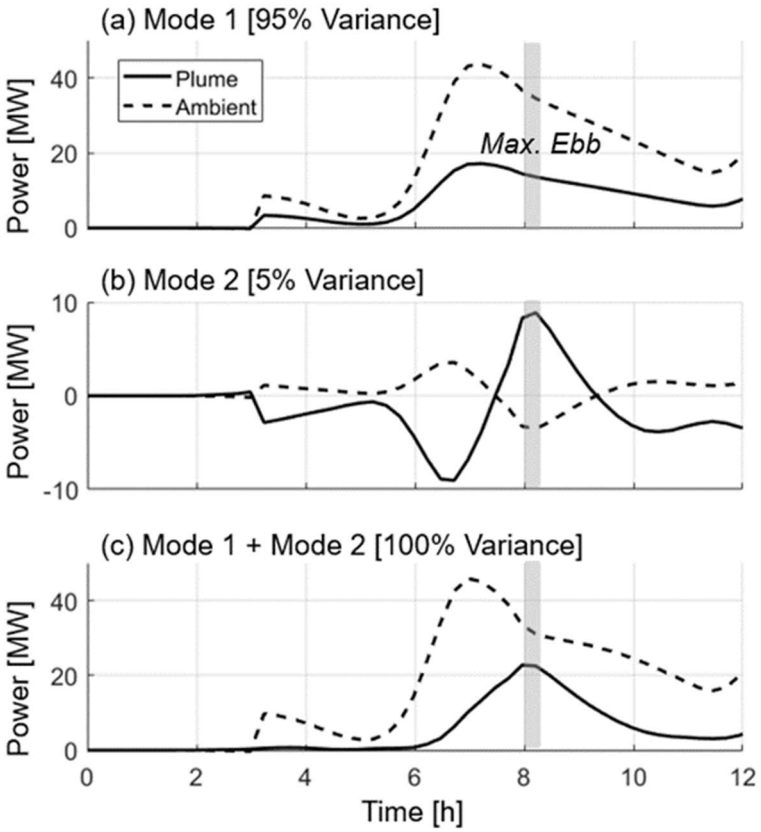


Figure B. 1: EOF analysis modes of tidal power ($M_T$) for the plume (solid, see Fig. 11d) and beneath-plume ambient (dashed) layers for $Q$ = 1000 m$^3$ s$^{-1}$ and $\eta_{tide}$= 1.5 m. Modes 1 (a), 2 (b), and the sum of 1 and 2 (c) are plotted. The *x*-axis is time in hours, and the *y*-axis is power in megawatts. Max ebb currents are marked with a gray box.

- Mode 1 is the tidal mode: the buoyancy flux and mixing power are completely from tidal mixing (comparable to Fig. 12d) which contributes a positive flux to both ambient and plume layers that maximizes near low water when currents are strongest.

- Mode 2 is the entrainment mode: it elucidates when buoyancy flux and mixing power is lost from one layer and given to the other. Mode 2 only accounts for 5% of the signal variance, implying buoyancy flux from ambient stratification beneath the plume does not significantly modify $M_T$ as calculated here (i.e. by adding excess buoyancy to the plume).

## APPENDIX C

A moderate discharge and tide experiment ($Q$ = 500 m$^3$/s, $\eta_{tide}$= 0.75 m) was re-run and analyzed using the U3H horizontal advection scheme in ROMS (all other simulations in this work use MPDATA) (Fig. C1). The purpose of testing a different advection scheme was to identify the influence of numerical mixing on the energy budget approach utilized in this study. The U3H scheme causes the smallest amount of numerical mixing relative to other commonly used schemes, which is why it was chosen to compare to here (Kalra et al. 2019). Numerical mixing is created by the discretization of the tracer transport advection term and can create spurious vertical mixing in 3D numerical models which would not exist in the real world. Numerical mixing can smear energy at salinity fronts which leads to a loss in the finer spatial structure at the front and a decrease in physical (real) mixing (Kalra et al. 2019). To accurately model and predict river plume mixing it is therefore important to estimate the importance of numerical mixing.

The most notable variation in mixing between advection schemes is in the frontal mixing term, $M_F$, with variation up to 0.03 MW existing between the MPDATA and U3H runs (Fig. C1a). Differences between interfacial, tidal, and total mixing powers are less noted because of larger scaled *y*-axes, but are likely of similar magnitude (Fig. C1b, c, d). MPDATA tends to underestimate frontal mixing but slightly overestimate the other terms.

The U3H scheme has been found to produce larger physical mixing than MPDATA (Kalra et al. 2019), indicating the larger $M_F$ relative to MPDATA is not a product of increased numerical mixing, but rather from an increased physical mixing that is not saturated by numerical mixing. If our calculations of frontal mixing (with MPDATA) were larger than the U3H values, this would indicate an estimate over-saturated with numerical mixing. These results fall in line with those of Kalra et al. (2019), as they found idealized, structured-grid experiments with strong external forcing produce the smallest relative contributions of numerical mixing. In general, this check between advection schemes indicates MPDATA

is performing in a satisfactory manner, and ultimately changing schemes has a negligible effect on total plume mixing or the relative importance of each term to total mixing (Fig. C1).

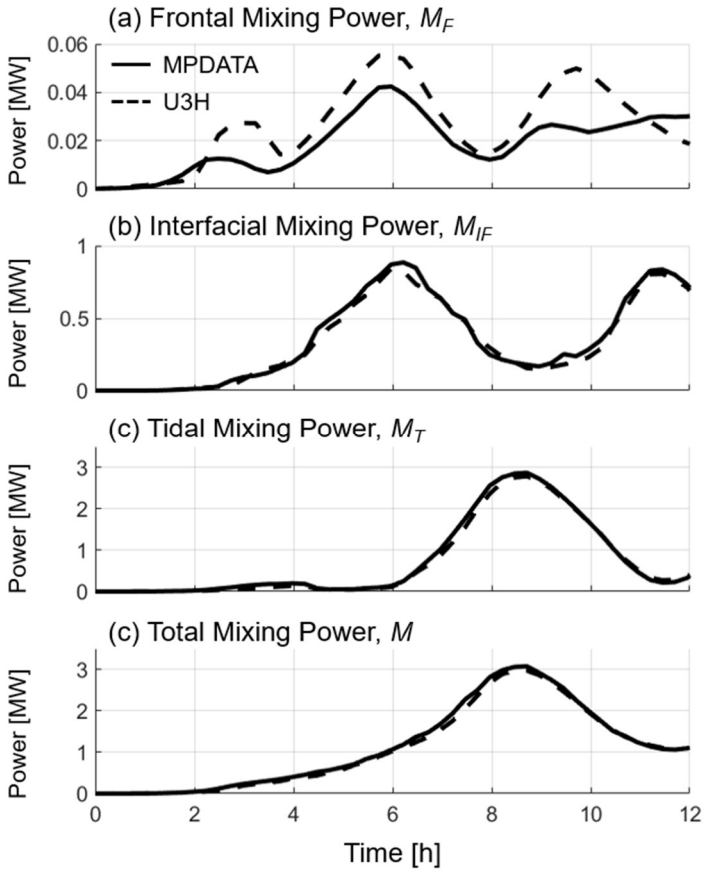


Figure C. 1: Time varying instantaneous energy budget terms for the $Q$ = 500 m$^3$ s$^{-1}$, $\eta_{tide}$= 0.75 m experiment for two horizontal advection schemes. Panels show frontal mixing power, $M_F$ (a), interfacial mixing power, $M_{IF}$ (b), tidal mixing power, $M_T$ (c), and total plume mixing power $M$ (d). Horizontal axes are time in hours. Solid lines denote the experiment run with MPDATA and dashed lines correspond to the experiment run with U3H.

## APPENDIX D

Here we expand on how stratification is quantified via vertical salinity variance and what to consider when interpreting it. Consider a plume underlain by a relatively shallow, salty shelf (Fig. D.1a) relative to the same plume over a deeper shelf of the same salinity (Fig. D.1b). The vertical average of salinity, $\bar{S}$ (and the salinity which would comprise the entire water column if fully mixed) will be greater for the plume over deeper water (Fig. D.1, right panels), subsequently increasing the depth averaged and integrated values of $(S_v')^2$. Although the density gradient between plume and salty water is unchanged, it would take more mixing to homogenize the deeper water column and so $\int (S_v')^2 dz$ scales up (not unlike stratification quantified via the potential energy anomaly (Simpson et al., 1990)). Similarly, most terms in Equations 20 (net rate of change, advection, and straining) would increase over the deeper water column

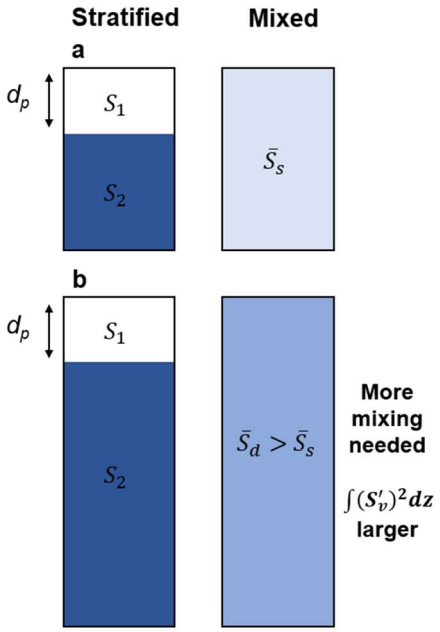


Figure D. 1: Conceptual schematic of plume of thickness $d_p$ and salinity $S_1$ overlaying relatively saltier water (salinity $S_2$)for a (a) shallow and (b) deep shelf (left panels). Final water column salinity assuming full mixing is shown for each (right panels) and equals the depth average of left panel salinities: $\bar{S}_s$ for shallow and $\bar{S}_d$ for deep. Color scales with salinity (white is fresh, dark blue is saltiest). Differing final, mixed water column salinities indicates differing $\int (S_v')^2 dz$ (stratification).

to hold the conservation of $(S_v')^2$. In this work, Equations 18, 19, and 20 are quantified from surface to bottom, and so variation in terms from sloping bathymetry exists and is valid given the definition of stratification we present here. By analyzing a control volume of constant size, we are intercomparing the same depth range on the shelf and so variation is relative to that volume.

In the analysis presented in this paper, there is still some potential for depth-derived variance variation to affect results, which is worth addressing here. Variation to water level from tides can effectively modify the control volume and therefore bias bulk variance quantities at a tidal time scale, while comparing different plumes which spread over nonidentical spatial scales introduces a similar issue. We evaluated the importance of depth bias by quantifying $\iiint (S_v')^2 dx\, dy\, dz$ and $\int (S_v')^2 dz$ for two idealized scenarios using the same horizontal area as our control volume (~225 km$^2$), but modified depths for a high tide case (25 m total depth) and low tide case (22 m total depth). These depths were chosen as they are near the average depth of the control volume we utilize (Fig. 18) and show sea level variability which is typical of the Merrimack outflow. A salinity profile representative of average conditions was applied over each domain and features a linear decrease from 15 psu at the surface to 30 psu at 4 m, with the remainder of the water column set to 32 psu. The difference in $\iiint (S_v')^2 dx\, dy\, dz$ due to depth variation was less than 2 psu$^2$ km$^3$ (~3% difference) while differences in $\int (S_v')^2 dz$ were less than 10 psu$^2$ m (~2% difference), both of which are considered negligible relative to variation from straining, advection, and mixing, which can create differences which are orders of magnitude apart (see section 3.3).

The salinity coordinate approach utilized in Section 3.3 tracks different plume salinity classes regardless of depth, possibly introducing some depth-derived bias to the results presented in Fig. 23. In particular, we would expect salinity classes (plume regions) which advect over significantly different depth ranges between plume SW and NE to be most influenced. In Fig. 20, the 20 – 25 psu salinity class corresponds to the periphery of the plume and exhibits the most spatial change between SW (large region nearshore, in depths < 10 m) and NE (large region offshore, in depths > 20 m). If significant, this

variation in depth would skew straining and mixing intensities up in the 20 – 25 psu class during plume NE relative to SW in Fig. 23. This does not occur, as intensities are similar or smaller, indicating minor bias in results.

## BIOGRAPHY OF THE AUTHOR

Preston Spicer was born in Farmington, Connecticut on February 24, 1995. He was raised in Preston, Connecticut and graduated from Norwich Free Academy in 2013. He attended the University of Maine and graduated in 2017 with a Bachelor of Science in Civil Engineering then in 2019 with a Master of Science in Civil Engineering. Preston started the doctoral program in Civil Engineering, with an emphasis on coastal hydrodynamics, in the fall of 2019. After receiving his Ph.D., Preston will be joining Pacific Northwest National Laboratory as a postdoctoral scientist, to begin his career in coastal engineering research. Preston is a candidate for the Doctor of Philosophy degree in Civil Engineering from the University of Maine in May 2022.